the underlying physics of fault rupture, and we limit the validity of our empirical scaling relations to the size range and structural framework of faults and fractures at Yucca Mountain. We elaborate in Section 6.2.

6.2 THE ISSUE OF TRIGGERING

Another issue that warrants comment at the outset is the triggering of fault slip and the relative importance of static versus dynamic triggering, an issue raised at SSC Workshops 5 and 6 and a subject attracting considerable attention since the 1992 Landers, California, earthquake (see Gomberg *et al.*, 1997, and references therein). The question here is whether our characterization of fault-displacement potential adequately accounts for the possibility of both types of triggering.

Static triggering refers to seismic slip hypothesized to result from static-stress changes which are caused by fault slip elsewhere and which increase the stress on a fault or fault segment so as to move it closer to a threshold of frictional failure, generally specified by the Coulomb failure criterion (see King *et al.*, 1994, and Simpson and Reasenberg, 1994, for overviews). Such static-stress changes can act oppositely to retard failure, but our focus here is on triggering. Dynamic triggering, which also involves frictional instability, refers to the hypothesized initiation of seismic slip by transient stress/strain changes associated with the passage of seismic waves, either from near or distant earthquakes (e.g., Gomberg and Bodin, 1994; Gomberg, 1996; Gomberg *et al.*, 1997).

Gomberg *et al.* (1997) usefully distinguish two types of potential triggering: in the first, termed a clock-advance type, triggering (static or dynamic) simply advances the time of fault slip that would have eventually happened anyway; in the second, termed a new-seismicity type, triggering (static or dynamic) induces fault slip that would not otherwise have occurred under a constant background load. Triggering from near earthquakes (tens of kilometers) may result from either static or dynamic stress/strain changes or both, whereas triggering from remote earthquakes (hundreds to thousands of kilometers) would be attributed to dynamic triggering (Gomberg, 1996; Gomberg and Davis, 1996).

For the Yucca Mountain fault-displacement characterization, we can separately consider (a) the triggering of a primary faulting event on one of the principal faults and (b) the triggering of secondary/distributed fault slip on any fault or fracture at Yucca Mountain. For both (a) and (b), instances of clock-advance triggering (static or dynamic) would have no effect on our probabilistic characterization of fault-displacement potential over the long-term because the relative timing of displacement events would be altered, not their average frequency over the long term, and estimates of the amount of displacement would not change.

What about new-seismicity triggering? First, we emphasize that such a hypothesis is still in a formative stage. Observational evidence presented in its support includes the triggering of small-magnitude earthquakes interpreted to be in excess of background seismicity at Long Valley, California, and at The Geysers, California (see Gomberg *et al.*, 1997, p. 302). Gomberg *et al.* (1997) show qualitatively by using model studies that the new-seismicity hypothesis is plausible under conditions of dynamic triggering, but they caution against using their results to make quantitative interpretations or predictions. Further, the potential for dynamic triggering appears to depend strongly on site characteristics and response (Gomberg, 1996).

For the case of principal faulting, we ask the question, What are the effects on our fault-displacement characterization if triggering (static or dynamic) were to cause surface-rupturing events that otherwise would not have occurred? Logically, this implies surface rupture on a fault not included in our inventory of faults that have a nonzero probability of being seismogenic. Allowing, for the sake of argument, that such new-seismicity triggering is plausible, we reason that its relative long-term probability of occurrence in the future would be similar to that in the past. Because our inventory of principal faults is based on the observed geology, which reflects ample opportunity during the Quaternary epoch for dynamic or static triggering of surface-rupturing events on potential sources of principal faulting not now accounted for, we consider the probability of triggering new principal faulting to be negligible.

If one pushes the concept of new-seismicity triggering to have it add to the number of surface-rupturing events on our inventoried principal faults, we again reason that its long-term relative probability of occurrence in the future, would be similar to that in the past.

As we describe later (see Sections 6.3 and 6.6), our displacement approach to surface displacement on a principal fault effectively accounts for the average relative frequency of any surface displacement, regardless of its cause. In our lower-weighted earthquake approach to principal faulting (Section 6.5), the frequency-magnitude relation of earthquakes on a principal fault is constrained by the average recurrence interval and/or slip rate from paleoseismology, which implicitly accounts for the aggregate long-term history of all displacement events, however they are produced.

Continuing this line of questioning, we examine the case of secondary/distributed fault slip and question what effects new-seismicity triggering (static or dynamic) would have on our characterization. Here too, our displacement approach (Sections 6.3 and 6.7) effectively accounts for all displacements, however they are produced. The last case remaining to be examined is that of our earthquake approach to secondary/distributed faulting on faults and fractures that are not principal faults (Section 6.8). In this case, our method accounts for all earthquakes on identified fault sources and in background source zones out to 100 km that represent opportunities for static or dynamic triggering. Whether or not triggering ensues is assessed probabilistically using empirical approaches. Admittedly, we do not account for plausible new-seismicity triggering by remote earthquakes at distances greater than 100 km. The magnitude of such earthquakes would have to be reasonably large for dynamic stress/strain changes to exceed a triggering threshold (Gomberg and Davis, 1996). Faced with the epistemic uncertainties associated with this particular case, we downweight it in our logic tree.

6.3 ORDER OF PRESENTATION

In the following sections, we first lay the groundwork for our fault-displacement assessment by defining terms and notation, presenting scaling relations, and describing our analysis of variability of slip at a point. We then proceed to describe our separate logic trees for principal and distributed faulting, beginning with an overview followed by sequential description of (1) our earthquake approach to principal faulting, (2) our displacement approach to principal faulting, (3) our point-estimate method (a displacement approach) for distributed faulting, and (4) our principal-distributed-faulting method (an extension of our

earthquake approach) for distributed faulting. Finally, we provide the assessments for the nine test calculation sites.

In applying our logic trees, we distinguish between sites subject to principal faulting (on potentially seismogenic faults) and sites subject to distributed faulting only. Sites in the first category are subject to the hazard of both principal and distributed faulting.

6.4 NOTATION

A potential pitfall we encountered in the fault-displacement analysis is the use of ambiguous terms, so we emphasize the importance of careful notation. In the case of "average displacement," for example, there are clear physical distinctions between the average displacement over the slip surface (i.e., the area of a fault engaged in a rupture event), the average displacement at the ground surface along a rupture, and the average displacement at a point on a fault (at or near the surface) over many displacement events at that point.

In our notation, both for fault displacement and ground-shaking hazard, we try to be as consistent as possible with (1) terms defined by Wells and Coppersmith (1994), whose regression relations we frequently refer to, (2) the notation and terms used most recently by R.R. Youngs and the SSC Facilitation Team (presentations at SSC Workshop 6), and (3) notation used in citations to which we refer the reader. In some cases, however, we give preference to special notation needed to emphasize clear thinking about what is being described and analyzed. For example, we use the term $\bar{U}$ for the average displacement over the slip surface to prevent any possible confusion with other terms for displacement involving the letter D. Following usual convention, a bar over a symbol signifies an average value.

We use superscript notation for some special cases in which the largest value of a parameter has particular importance, in part to avoid confusion with the commonly used suffix "max." (Consider the term "Dmax," which has been used extensively during the SSC Workshops to indicate a maximum displacement, but variously defined.) Some scaling relations involving fault length are only valid for <u>total</u> fault length, which we emphasize by using the term L^{total}. Similarly, the value of maximum surface displacement, MD, that is estimated for the largest displacement event on a fault (generally involving L^{total}) we designate as MD^{max}.

The following is a basic outline of notation used. More complete explanation is given as the terms arise in subsequent discussion.

AD = average (surface) displacement
AR = aspect ratio (L/W)
D or d = general terms for a displacement on a fault
Dcum = total cumulative displacement (herein meaning post-Tiva Canyon Tuff)
D_E = single-event displacement on a fault at or near the surface
$\overline{D}_E$ = average value of D_E at a point on a fault over many displacement events
L = general term for the length or longest horizontal dimension of a fault or rupture (equivalent to RLD in the case of a single rupture)
L^{total} = total length of a fault
M = magnitude (herein meaning moment magnitude)
MD = maximum (surface) displacement
MD^{max} = expected value of MD corresponding to the largest displacement event on a particular fault
P[C] = probability of being capable of slip (i.e., slip susceptibility) given the contemporary stress field at Yucca Mountain
P[S] = probability of being seismogenic (i.e., of generating an earthquake of $M \geq 5.0$)
P[slip|pf] = probability of secondary/distributed faulting, given principal faulting on a nearby fault
QSR = Quaternary slip rate
RA = rupture area
RI = recurrence interval
RLD = subsurface rupture length (rupture length at depth)
RW = rupture width (downdip dimension)
SR = slip rate
SRL = surface rupture length
$\overline{U}$ = average displacement over a slip surface (i.e., the area of a fault engaged in a rupture event)
W = general term for the width or downdip dimension of a fault
λ_{DE} = frequency at which displacement events occur

6.5 SCALING RELATIONS

In this section we provide a basis for adapting scaling relations that can be used for characterizing fault-displacement potential on structures ranging from small fractures upward to the unsegmented relatively small faults ($L < 25$ km) with relatively small cumulative displacement (< 0.5 km) at Yucca Mountain.

We emphasize that we use only scaling relations that are empirically founded, reasonably robust, and which can be adopted without critical assumptions about the underlying physics of fault rupture. We recognize that some of the scatter in data distributions that control the scaling relations we use undoubtedly arise from the kind of complications in earthquake source mechanics discussed by Bodin and Brune (1996)—such as might be expected, for example, from dynamic rupture propagation with spatially varying stress drops, as opposed to quasi-static constant-stress-drop modeling.

The following logic is used to develop our scaling relations: (1) for the Yucca Mountain faults and fractures to be considered, and based on empirical observations alone, a linear approximation can be justified for the scaling of single-event slip $\overline{U}$ with fault rupture length L; (2) empirical observations over a wide range of scales show that total cumulative displacement Dcum on a fault scales linearly with total fault length L^{total}; (3) given (1) and (2), $\overline{U}$ should scale linearly with Dcum when $L = L^{total}$. We show how knowledge of Dcum on a fault or fracture can provide a practical basis for scaling the likely amount of slip on that feature during a future displacement event.

$\overline{U}$ Versus L

Abundant data summarized by Abercrombie (1995, her Figure 11), among others, provide an empirical basis for relating seismic moment to the cube of source dimension—without any assumption about stress drop—over the range from 10 m to at least 10^4m. The measurements of source dimension are based mostly on corner frequencies from shear-wave spectra, such that each represents the radius r of an equivalent circular fault. Based on the moment equation, the distribution of these data imply that $\overline{U}$, on average, scales linearly with r, and similarly $\overline{U}$ can be inferred to scale linearly with rupture length L for roughly equidimensional faults in this range of source dimensions. Thus we adopt a relation of the form, $\overline{U} = \alpha * L$, where α is the constant of proportionality.

Let us be clear. We are not arguing for a model-dependent linear scaling of $\overline{U}$ with L (a so-called L model), which we recognize to be controversial, particularly for large earthquakes (Romanowicz and Rundle, 1993; Bodin and Brune, 1996). Rather, we argue that a linear

relationship is a reasonable approximation for the fault sizes we are considering—based on the abundant earthquake source data summarized by Abercrombie (1995).

We derived an empirical value of α for the Yucca Mountain local faults using data in Table AAR-4 (preferred values for independent faults, Bare Mountain fault excluded). In order to compile consistently paired values of displacement and rupture length for regression, the data were first corrected in the following way. Values of MD, the maximum surface displacement per event along a fault (labeled Dmax in Table AAR-4), were converted to $\overline{U}$ using Wells and Coppersmith's (1994) modal value 0.76 for the ratio $\overline{U}$/MD. Also, we converted the tabulated values of total fault length (labeled active length in Table AAR-4), which were originally assessed as estimates of SRL, to RLD using Wells and Coppersmith's (1994) result that the expected ratio of SRL/RLD is 0.75. Applying the latter correction is appropriate insofar as all the SRL values for the independent faults in Table AAR-4 are within the range of data from which the expected ratio was originally estimated (see Wells and Coppersmith, 1994, p. 985).

Given paired values of $\overline{U}$ and L^{total} for 19 faults, we followed guidance from R.R. Youngs of the Facilitation Team to derive an empirical estimate of 3.69 ($\pm$1.10) x 10^{-5} m/m for α from the mean value of log ($\overline{U}/L^{total}$) (see equation 1, Table AAR-9). This procedure was followed in order to allow the Facilitation Team to estimate aleatory uncertainty in an appropriate form. For comparison, we performed similar calculations using data from S. K. Pezzopane and T. E. Dawson (USGS, written communication, 1996), who plot Quaternary displacement per event versus maximum fault length for six Yucca Mountain faults (their Figure 9-19). To convert their displacement values to $\overline{U}$, we interpreted them as estimates of average surface displacement AD and used Wells and Coppersmith's (1994) modal value 1.32 for the ratio $\overline{U}$/AD. Processing Pezzopane and Dawson's six paired values of displacement and fault length in the form of log ($\overline{U}/L^{total}$), α = their values of "maximum fault length" 3.42 ($\pm$ 1.08) x 10^{-5} m/m, taking L to be estimates of SRL.

For our logic tree, we adopt $\alpha = 3.69 \times 10^{-5}$ m/m derived from our own data—both for internal consistency and because of our larger data set. Because the data are specific to the Yucca Mountain faults, we prefer the result to other values found in the literature. Cowie and

Scholz (1992c) cite values for α ranging from ~1.5 x 10^{-5} for continental plate boundary earthquakes to ~1.0 x 10^{-4} for intraplate earthquakes, including an estimate of ~2.0 x 10^{-5} for earthquakes in the northern Basin and Range.

Dcum Versus L^{total}, General Relation

The basis for the linear scaling of cumulative displacement Dcum with total fault length are developed at length by Cowie and Scholz (1992a,b,c). More recently, rigorous statistical testing by Clark and Cox (1996) of 11 worldwide data sets of log (Dcum) versus log (L^{total}), for fault populations ranging in length from tenths of a meter to hundreds of kilometers, confirm a linear relationship between fault displacement and length within each data set. (See H. L. McKague *et al.*, CNWRA, written communication, 1996, for evidence of the linear scaling of Dcum with fault trace length for faults in the general Yucca Mountain region.)

Following the conventional analysis of Dcum versus L in log-log space, we seek an empirical relation of the form, log (Dcum) = K + log (L^{total}), where K is a constant. In terms of the alternate scaling factors P (Clark and Cox, 1996) and γ (Cowie and Scholz, 1992 b, c), $P = 10^{-K} = 1/\gamma$. We derived an empirical value of K for the Yucca Mountain faults using data in Table AAR-4 (preferred values for independent faults, Bare Mountain fault excluded). The values of Dcum (labeled total displacement in Table AAR-4) consistently represent total cumulative displacement of the Tiva Canyon Tuff. As we did in relating $\bar{U}$ to L^{total}, values of total fault length were first converted to RLD. The resulting regression of 16 available paired values of Dcum and L^{total} yielded a best-fit value of K = - 1.58 (see Table AAR-9 for regression parameters), equivalent to P = 38 or $\gamma = 2.6 \times 10^{-2}$ m/m. We examined, but decided not to regress 6 paired values of Dcum and L^{total} presented by S. K. Pezzopane and T. E. Dawson (USGS, written communication, 1996) in their Figures 9-19 and 9-20 because those data are presented as only preliminary.

Dcum Versus L^{total} for Small Faults and Fractures

Available data and well-constrained trends indicate that Dcum on small faults and fractures appears to be systematically smaller than that estimated by extrapolating the scaling with length from larger faults (Clark and Cox, 1996; Cowie and Scholz, 1992b). We accept this empirical observation.

Based on data in Clark and Cox (1996, their Figure 1) and the range of our data, we judge that our scaling constant for Dcum/L derived in the previous section can be reliably applied only for L greater than about 3 km and Dcum greater constant for than about 75 m. For smaller faults and fractures—down to the scale lengths of features possibly of engineering concern in the repository, we use the data of Clark and Cox (1996) to assess the following distribution for the scaling factors (and corresponding weights), where the minimum value of P is that observed from the data set of the Yucca Mountain faults:

$K = -1.58$ [$P = 38$; $\gamma = 2.63 \times 10^{-2}$] (weight = 0.3)
$K = -2.18$ [$P = 150$; $\gamma = 6.67 \times 10^{-3}$] (weight = 0.4)
$K = -2.70$ [$P = 500$; $\gamma = 2.00 \times 10^{-2}$] (weight = 0.3)

$\bar{U}$ (and MD^{max}) Versus Dcum

Given the relations: (1) $\bar{U} = \alpha * L^{total}$ and (2) $\log (Dcum) = K + \log (L^{total})$, straightforward substitution leads to (3) $\log \bar{U} = \log \alpha - K + \log (Dcum)$ when $L = L^{total}$. This in turn can be expressed in the form $\bar{U} = \beta * Dcum$, where $\beta = \log^{-1} (\log \alpha - K)$. For small faults and fractures, our distribution on K transforms into the following values (and weights) on β (m/m):

1.40×10^{-3} (0.3), 5.59×10^{-3} (0.4), 1.85×10^{-2} (0.3).

The restriction that $L = L^{total}$ implies that the assessed value of Dcum should be the largest value for the entire fault. Thus, the scaling we have derived is fundamentally tied to maximum values associated with a maximum displacement event, which is equivalent to a maximum-magnitude earthquake on a fault. In both circumstances, expected parameters for smaller-size events are scaled from those of the maximum event using other information.

Because we are concerned with fault-displacement characterization at or near the surface, we use the parameter MD^{max}, the value of MD corresponding to the maximum displacement event on a particular fault, instead of $\bar{U}^{max}$ for that same event. We relate the two using Wells and Coppersmith's (1994) modal value of 0.76 for the ratio $\bar{U}$/MD such that, for the relatively small-displacement faults at Yucca Mountain (Dcum <500m), $MD^{max} = 1.32 * \bar{U}^{max}$ or, by substitution, $MD^{max} = 1.32 * \beta * Dcum$.

QSR Versus Dcum

In our point-estimate method for distributed faulting, we require estimates of Quaternary slip rate QSR on a secondary fault or fracture, given an observation of Dcum. Here, we develop a regression relation between QSR and Dcum based on selected paired values in Table AAR-4 for the local Yucca Mountain faults. We use the median values listed for 11 of the 19 independent faults, excluding the Bare Mountain, E. Lathrop Cone, East Busted Butte, Midway Valley, and West Dune Wash (1 and 2) faults. The Bare Mountain fault is excluded because we judge it to be less relevant than the Yucca Mountain faults and it is an extreme outlier if used. Data for the latter five faults are excluded because their slip rates are based on relative comparisons of geomorphology, rather than on direct paleoseismic information.

Using the 11 paired values of QSR and Dcum, we performed a linear regression of QSR (mm/yr) on Dcum (m), constraining the intercept to be zero, and derived a value of 3.26 ($\pm$ 1.72) x 10^{-5} mm/yr/m for the slope coefficient. Statistical parameters for the regression are given in Table AAR-9.

6.6 DISPLACEMENT AT A POINT

A key part of the methodology for fault-displacement characterization is assessing the variability of slip at a point—both (1) as a function of position along strike of the fault, given the size of an event, and (2) variability of slip at the same point from event to event. Of the techniques presented and evaluated to date (summarized in presentations by R.R. Youngs at SSC Workshops 5 and 6), we are satisfied with available solutions for (1), but not (2).

The method developed by the Ake, Slemmons, McCalpin (ASM) team is well suited for estimating variable slip along strike, scaled to the maximum surface displacement MD for a given event (see summary of fault-displacement-hazard methodologies by SSC Facilitation Team, SSC Workshop 6, Figure 5; see also Appendix F this volume). The statistical averaging inherent in the method is realistic, and we see no reason to use an alternate approach that is more deterministic. We considered alternate shape functions to the elliptical displacement profile of the ASM model. Cowie and Scholz (1992a), for example, describe a profile predicted to taper gradually toward the fault tip; they also show normalized

displacement profiles for faults in Japan and Britain that are relatively linear from fault-center to fault-end. Nicol *et al.* (1996), on the other hand, show normalized profiles for restricted faults (i.e., those that intersect the surface or closely approach other faults) whose envelope follows the elliptical shape of the ASM profile. In the end, we determined the ASM model is sufficient for the use we make of it in our logic tree (1) in our earthquake approach to principal faulting (Figure AAR-16) and (2) in assessing distributed faulting at sites where principal faulting also occurs (Figure AAR-23). We adopt the statistical relationships to repeat the ASM model presented in Appendix H, Section H.3.1.

In analyzing the problem of variability of slip at a point from event to event, we observed that, in aggregate, the displacement measurements in the many fault trenches at Yucca Mountain, scaled to MD^{max} on each fault, reflect an exponential-like distribution. This appears to be a combined result of both temporal and spatial variability. We proceed to describe our analysis and use the results as a key basis for assessing the conditional probability for displacement exceedance.

We adapt and extend the approach used by the Doser, Fridrich, Swan (DFS) team (presentation at SSC Workshop 5; see also Appendix H this volume). The DFS team made a composite of displacement data measured in trenches throughout the Yucca Mountain region and summarized by S. K. Pezzopane *et al.* (USGS, written communication, 1996a) in their Table 5-1. Each displacement was normalized to the average from its same trench, and data were then pooled from all trenches. We note that the true average slip over many events at the same point is poorly estimated when the number of observations in a single trench is small. We reasoned that a more robust basis for normalizing the displacement measurements would be to compare them to some independent measure, and we selected MD^{max}, the expected value of MD corresponding to the largest displacement event on that fault.

First, we used the same multiple approaches specified in Figure AAR-16 of our logic tree (but using only median parameter values) to get a weighted-average estimate of MD^{max} for each of the nine faults associated with the 19 trench summaries in Table 5-1 of S. K. Pezzopane *et al.* (USGS, written communication,1996a). Second, we normalized each of 82 available displacement measurements (excluding the Rock Valley fault) to a corresponding value of MD^{max}. Third, we constructed both a probability density function (PDF) and a

cumulative distribution function (CDF) for the combined data, shown here in Figure AAR-11. We discuss these results presently. Fourth, as a test, we carefully examined the trench locations with respect to their along-strike location and used data only for nine of the 19 trenches that were unambiguously located along the central half of a fault to construct a separate PDF-CDF combination. Again, distributions similar to those in Figure AAR-11 resulted. For greater robustness, we chose to use the data from all 19 trenches. The data are listed in Table AAR-10.

Regarding Figure AAR-11, one might ask, 'how can the ratio D/MD^{max} exceed 1.0, as plotted on the abscissa?' Note, as described in the proceeding paragraph, that MD^{max} for each fault is a weighted-average from different approaches of the expected maximum displacement and that central values were used in the calculations. Thus epistemic uncertainty in the estimate and randomness in the process allows the observed values of D to exceed the expected value of MD^{max} estimated for any individual fault. As we have estimated it, MD^{max} simply provides a basis for normalizing observations for comparison from fault to fault.

The PDF shown in Figure AAR-11 was fit with the function $y = 0.09 \exp (- 0.68\ D/MD^{max})$. Regression parameters are listed in Table AAR-9. Following Benjamin and Cornell (1970), we analyze the CDF in terms of the generalized exponential distribution $\lambda e^{-\lambda x}$, whose CDF is $1-e^{-\lambda x}$. For the generalized PDF, values along the x-axis are numerically plotted as λx. The mean value of D/MD^{max}, which is 0.83 for the 82 displacement measurements, directly provides the expected value of $1/\lambda$. Hence $\lambda = 1.20$. The variance on λ is approximated by λ^2/n, and the median for the distribution is given by $0.693/\lambda$.

In the CDF in Figure AAR-11 we superpose the curve for $1-\exp (-1.20\ (D/MD^{max})$, which shows good agreement with the observed CDF. Importantly, the mean (0.83) of the observed values of D/MD^{max} gives a key piece of information—namely, a reliable estimate of $\bar{D}_E$, the average displacement at a point on a fault (at or near the surface) over many displacement events at that point.

The data of Figure AAR-11 were analyzed independently by the Facilitation Team (Appendix H, Section H.2.5), and various statistical distributions were fit to the data. As described in Appendix H, good fits to the data were obtained for an exponential distribution with a mean

of 0.83 and for a gamma distribution with two parameters; a slightly better goodness of fit for the gamma distribution is shown to be only marginally statistical significant.

In examining Figure AAR-11, note that a lower limit of resolution is implicit and inescapable. Some would argue that very small, unobserved surface displacements are greatly more numerous than observed ones, but such a hypothesis must be reconciled with observed earthquake statistics and the observed geology, particularly in terms of the cumulative offset implied by having many small unobserved displacement events. For example, if a one-centimeter displacement event is thought to be material, 100 such unobserved events require one meter of cumulative offset to be accounted for during some time period, and 1,000 such events, 10 m.

In the case of the data used in Figure AAR-11, the smallest bin is centered on 0.1 D/MD^{max}. Following conventional rules for rounding, the two smallest observed ratios of 0.04 and 0.05 (rounded to the nearest even integer) fell below the smallest bin. These ratios correspond to one displacement of 5 cm on the Solitario Canyon fault (MD^{max} =112 cm) and another of 6 cm on the Paintbrush Canyon fault (MD^{max} = 112 cm). The eleven displacement events included in the smallest bin range from 3 to 7 cm.

Based on the data shown on Figure AAR-11, together with the supporting analysis of the Facilitation Team (Appendix H), we adopt the exponential distribution as an appropriate and reasonable empirical predictor for the distribution of displacement at a point — within implied limits of resolution for the ratio of a displacement event to MD^{max}.

To summarize, MD^{max} provides a useful basis for scaling and comparing displacement measurements on the Yucca Mountain faults. The result that aggregated values of D/MD^{max} can be modeled approximately by an exponential distribution has great utility. Not only does the distribution enable a reliable estimate of the average displacement at a point, it also combines both spatial and temporal variability at that point. We interpret the distribution to be a composite effect of event-to-event variability of primary fault ruptures, along-strike variability during ruptures on the same fault, and distributed faulting triggered by static and/or dynamic stress/strain changes. We emphasize that having displacement events at a generalized point on the surface approximate an exponential distribution does not necessarily

imply that earthquakes on the primary faults also follow such a distribution. We adhere to our separate assessment of characteristic versus exponential slip events at depth on the principal faults.

6.7 OVERVIEW OF LOGIC TREES

For convenience, we construct separate logic trees for principal and distributed faulting. After evaluating various approaches proposed and discussed at SSC Workshops 4 and 5 for characterizing fault-displacement potential, we use both an earthquake and a displacement approach for principal faulting. We then assess the potential for distributed faulting using two methods described by R. Youngs (presentation at SSC Workshop 5) as a point-estimate (displacement) method and a principal-distributed faulting (earthquake) method.

For principal faulting, we give a weight of 0.67 to the displacement approach and 0.33 to the earthquake approach. We give greater weight to the former because we are persuaded that, ultimately, the size and frequency of displacements on faults and related features exposed at the surface (or in the repository) must be governed by the budget of what is observed—namely, the record of displacements at or near the surface.

When we assess the potential for distributed faulting, we take different approaches for (1) sites of distributed faulting only and (2) sites where principal faulting also occurs (Figure AAR-12). We do this because at the latter sites the displacement approach for principal faulting simultaneously accounts for distributed faulting at the same point. At such sites, conditional on using the earthquake approach to principal faulting (weight = 0.33), we then use only the principal-distributed faulting method to characterize distributed faulting.

For assessing the potential for distributed faulting at sites of distributed faulting only, we give a weight of 0.33 to our principal-distributed faulting method and 0.67 to our point-estimate method. We downweight the first method for two reasons. First, as discussed earlier in Section 6.2, it does not fully account for plausible new-seismicity triggering by dynamic stress/strain due to remote earthquakes at distances greater than 100 km. Second, we have more confidence in our point-estimate method for characterizing the frequency of slip on a specific secondary fault or fracture.

Throughout our logic tree, whenever we use a regression relation from Wells and Coppersmith (1994), we intend the use of the respective equation for the category of All Data. Our defined sources of principal faulting include those local fault sources in Table AAR-3 which have a probability of being seismogenic, P[S] > 0.

6.8 PRINCIPAL FAULTING—EARTHQUAKE APPROACH

In the earthquake approach (Figure AAR-13), our logic tree for ground-shaking hazard provides a starting point at which one is given a frequency-magnitude distribution for a subject fault. Given an event of magnitude M, we proceed to estimate rupture length L, in part as a predictor of maximum surface displacement (MD) and average surface displacement (AD). For later application, we distinguish between surface rupture length, SRL (for cases of rupture at or near the surface), and subsurface rupture length, RLD. Unless specified otherwise, L is implied to be subsurface rupture length.

Estimating RLD

We give equal weights (0.5, 0.5) to two approaches for estimating RLD (Figure AAR-14). The first is the straightforward use of a regression relation between RLD and M from Wells and Coppersmith (1994). In the second approach we follow Nicol *et al.* (1996), who review data indicating that simple normal faults have an approximately elliptical shape with a subhorizontal major axis. We constructed a cumulative distribution of aspect ratios for 54 earthquake slip surfaces using data from Nicol *et al.* (1996, their Table 2), from which we assess the following distribution for aspect ratio (and relative weighting):

0.8 (0.3), 1.4 (0.4), 2.5 (0.3).

Given M, we use the regression relation, log (RA) = -3.49 + 0.91 M (Wells and Coppersmith, 1994) to estimate rupture area RA in units of km^2. For an elliptical rupture, the major axis = L/2, from which it can be shown that L (km) = $[(4/\pi * \text{aspect ratio} * (RA)]^{1/2}$.

Estimating SRL

Our two approaches to estimating SRL (Figure AAR-14) basically parallel those just described for estimating RLD, and again we assign equal weights (0.5, 05). The first approach uses a regression relation between SRL and M from Wells and Coppersmith (1994). In the second approach, we calculate the length dimension of an elliptical rupture area as for RLD, but the difference is that for the range of lengths being considered, SRL is expected to be less than RLD, and we adopt the ratio 0.75 for SRL/RLD (Wells and Coppersmith, 1994) as a correction factor.

Estimating P[Surface Rupture]

In order to estimate the probability of surface rupture, P[surface rupture], given an event of magnitude M, we invoke a simulation approach developed for the ground-motion modeling in which the location of a rupture is randomized on the subject fault source (Figure AAR-15). The modeling uses our adopted focal depth distribution for $M \geq 5.0$ (based on one from K. Smith, presentation at SSC Workshop 2, "Depth Distribution—SGB 1979-present"). The distribution of distance from a hypocenter to the top of rupture is calculated by allowing the hypocenter location to be uniformly distributed on the lower 75% of the rupture.

In the randomization analysis, the subsurface dimensions of a rupture for an event of magnitude M are modeled by using, with equal weights, the two methods already described for estimating RLD (see Figure AAR-14). In the first, RLD is determined from a regression relation between RLD and M, and downdip rupture width W follows from an assessed distribution on aspect ratio (Figure AAR-15), which has the following distribution of values and weights, justified earlier: 0.8 (0.3), 1.4 (0.4), 2.5 (0.3). In the second method, RLD and W derive from the rupture area RA of an elliptical rupture (where RA is determined from a regression relation between RA and M) whose aspect ratio has the same distribution specified above.

For realizations of surface rupture, the weighted-average value of surface-rupture length SRL (Figure AAR-14) is used to randomize the along-strike location of surface rupture. For the general case in which SRL is less than the total trace length of a fault, the cases of surface rupture in effect become a one-dimensional randomization in which a rupture of trial length SRL is randomly located along the fault trace. This later enables one to assess the location of

any point on the fault with respect to a realized surface rupture in order to apply the ASM model for variability of slip along strike. In any application to a specific fault, the weighted-average value of SRL cannot exceed the total fault length and must be limited to the latter in such cases.

Although this simulation modeling for estimating the probability of surface rupture undoubtedly oversimplifies some complex aspects of faulting, we adopt it for the following reasons. It directly incorporates our subsurface characterization of fault sources at Yucca Mountain and it yields results that are similar to the empirical distributions for the probability of surface rupture derived from samples of historical earthquakes in the Great Basin and surrounding regions of the western U.S. (see Appendix H).

Estimating MD And Variability Along Strike

Given M, SRL, and RLD, we proceed to estimate the expected maximum surface displacement MD on a principal fault (Figure AAR-16).

We focus on estimating the expected value of MD for principal faulting because we adopt the ASM model to assess variability of slip along strike, and that method uses a distribution normalized to MD. Our logic tree outlines three approaches to estimating MD, and we give basically equal weights to each approach. The first two involve regression relations from Wells and Coppersmith (1994) which deliver MD, given SRL or M.

We do not use direct assessments of MD from paleoseismic data tabulated in Table AAR-4 because those values imply rupture of total fault length. Instead, the paleoseismic data for the Yucca Mountain local faults are incorporated into the scaling relation between $\bar{U}$ and RLD, which is our third approach to estimating MD.

6.9 PRINCIPAL FAULTING—DISPLACEMENT APPROACH

Estimating MD^{max}

In our displacement approach to principal faulting (Figure AAR-17), we use three methods to estimate MD^{max}, which provides an underpinning for the recurrence modeling: (1) a fault-

length approach (weight = 0.3), (2) a cumulative-displacement approach (weight = 0.3), and (3) a paleoseismology approach (weight = 0.4).

In the fault-length approach, we use (a) an empirical relation between MD and SRL from Wells and Coppersmith (1994) (weight = 0.4) and (b) our empirical scaling relation between $\overline{U}$ and L^{total}, from which MD^{max} is then scaled from the implicit maximum value of $\overline{U}$ (weight = 0.6). In the first relation, the maximum value of SRL is used to yield MD^{max}.

The cumulative-bedrock-displacement approach, informally referred to as the "Dcum approach" in parts of our logic tree, uses the scaling relations we developed and discussed at length in the section on Scaling Relations. The operative relation is $MD^{max} = 1.32 * \beta *$ Dcum, where the scaling factor β depends on the size of the fault being considered (see Figure AAR-19). We described earlier our reasoning for treating larger and smaller faults differently, where the threshold of larger faults is approximately $L^{total} > 3$ km and Dcum > 75 m. For the larger faults, which with few exceptions include nearly all the principal Yucca Mountain faults, $\beta = 1.40 \times 10^{-3}$ m/m. For the smaller faults, the values (and weights) for β (m/m), justified earlier (see section on Scaling Relations, $\overline{U}$ [and MD^{max}] Versus Dcum), have the following distribution

$$1.40 \times 10^{-3}\ (0.3),\ 5.59 \times 10^{-3}\ (0.4),\ 1.85 \times 10^{-2}\ (0.3).$$

In the Paleoseismology approach, we use the values tabulated in Table AAR-4 under Dmax as direct assessments of MD^{max}.

Recurrence Of Displacement Events And Variability At A Point

To estimate the frequency of fault displacement as a function of size, we rely on the exponential distribution we derived (Figure AAR-11) as a basis for recurrence modeling (Figure AAR-17). We originally considered using an approach similar to that of Youngs and Coppersmith (1985) to derive a frequency-displacement recurrence relation using slip-rate information to distribute seismic moment. With our exponential model in hand, however, we consider it appropriate to use the more direct approach of estimating λ_{DE}, the average frequency of slip events, by dividing slip rate by $\overline{D}_E$, the average displacement at a point over many events. As discussed in our section on "Variability in Displacement at a Point," $\overline{D}_E$ is

estimated by 0.83 MD^{max}. Slip-rate information for the principal faults is provided in Table AAR-4.

6.10 DISTRIBUTED FAULTING—POINT-ESTIMATE METHOD

This method has three basic steps, which we have modified from an approach proposed by the DFS Team at SSC Workshop 5: (1) estimation of slip rate at a point using alternative methods linked to an observed value of Dcum; (2) estimation of the average frequency of slip events at the same point; and (3) estimation of the variability of slip at the point.

In our application of this method (Figure AAR-18), we give zero weight to estimating what we will call Quaternary slip rate QSR by assuming uniform slip on a feature during the last 12.7 Ma (post-Tiva Canyon Tuff), based on abundant evidence for major deformation prior to 11.6 Ma (pre-Rainier Mesa Tuff). We adopt as one approach, however, the possibility of uniform slip during the past 11.6 Ma. In order to assess the fraction of Dcum that accumulated before 11.6 Ma—in a way that is completely independent of paleo-seismological slip-rate information, we did the following. We used data presented by Fridrich *et al.* (1996) for estimates of extension in Miocene bedrock (based on the amount of stratal tilting as a measure of extension) for the three time periods: 12.7 to 11.6 Ma, 11.6 to 10.5 Ma, and 10.5 Ma to present. For the Controlled Area (of most direct interest to this fault-displacement characterization), we estimated the proportion of the cumulative percent of extension post-dating the 12.7 Ma Tiva Canyon Tuff that occurred from 12.7 to 11.6 Ma. Based on conditional logic reasoning, we then assessed the following distribution for the fraction of Dcum that has occurred during the last 11.6 Ma:

60% (0.3), 40% (0.4), 20% (0.3).

The post-11.6 Ma slip rate in this approach is inferred to approximate the average QSR.

Our second approach to estimating QSR was adapted from one described by J. Yount (presentation at SSC Workshop 5) in which offsets of basalts 3.7 Ma old in the Crater Flat basin are used to estimate the fraction of Dcum post-Tiva Canyon Tuff that has occurred in the past 3.7 Ma. Based on estimated offsets of basalts across the So. Windy Wash and So.

Crater Flat faults, and offset tephra across the Stagecoach Road fault, we assessed the following percentages (and weights):

40% (0.3), 16% (0.4), 5% (0.3).

Our third approach is the use of an empirical estimate of QSR as a function of Dcum, based on paleoseismic slip-rate data. The regression relation has already been described and is summarized in Table AAR-9. We assign relative weights to the three approaches that are inversely proportional to the duration of the time interval for which uniformity of slip rate is assumed. Accordingly, the weights are 0.1 for uniformity during the past 11.6 Ma, 0.3 for the past 3.7 Ma, and 0.6 for the time span covered by paleoseismic data (approximately ranging from 0.1 to 1 Ma).

In order to estimate MD^{max} on a secondary fault or fracture, we use information on L^{total}, if available, together with Dcum (Figure AAR-19). If both length and total-displacement information are available, we give equal weight to estimating MD^{max} from: (1) the scaling relation, $MD^{max} = 1.32 * \bar{U}^{max}$, where $\bar{U}^{max}$ (m) = $3.69 \times 10^{-5} L^{total}$ (m); and (2) the Dcum approach we described above in the section, Principal Faulting—Displacement Approach, Estimating MD^{max}. We then use the same procedures described in that section to estimate λ_{DE} and variability of slip at a point (Figure AAR-20)—except that here, our estimates of QSR come not from paleoseismic information in Table AAR-4, but from the feature-specific estimates of QSR just made.

6.11 DISTRIBUTED FAULTING—PRINCIPAL-DISTRIBUTED FAULTING METHOD

In this method, principal faulting may cause the occurrence of slip on secondary/distributed faults and fractures as well as on other principal fault sources. The frequency-magnitude distribution on the primary seismogenic fault is first determined by the earthquake method for principal faulting (Figure AAR-21). Whether a secondary fault or fracture slips is judged to depend on its slip-susceptibility tendency, the size of the principal faulting event, and distance from the principal fault in either the footwall or hanging-wall direction.

We attempted to invert the magnitude and frequency of principal faulting from our displacement approach using MD^{max}, but we encountered what we judged to be a fatal flaw. Given a principal fault, we can straightforwardly determine MD^{max} for the fault, as we did, for example, in our Principal Faulting-Displacement Approach. Given MD^{max}, our exponential distribution yields the relative frequency of displacement events of size D_E/MD^{max}. However, this measure is for the displacement at a single point and cannot be transformed into some measure such as AD or MD from which the magnitude of the event can be estimated. Therefore, we assign full weight to the earthquake approach for determining the magnitude and frequency of principal faulting.

Our logic tree for handling secondary/distributed faulting includes two probability terms (Figure AAR-21). First, P[C] is the probability that a feature is capable of slip to produce secondary/distributed displacement, given the contemporary stress field at Yucca Mountain. Second, P[slip|pf] is the probability that a secondary fault or feature slips to produce secondary/distributed displacement, given principal faulting nearby. Given a principal faulting event, the potential for secondary/distributed displacement on a nearby fault or fracture directly contains the multiplicative terms, P[C] and P[slip|pf]. Rules for assessing P[C] are given in a following section.

In order to apply P[slip|pf], we invoke a probability distribution function described by R.R. Youngs (presentation at SSC Workshop 6; see also Appendix H this volume) based on data from S. Pezzopane for the density of distributed faulting accompanying historic normal-faulting earthquakes in the extensional western U.S. Cordillera—as a function both of event size and distance in the footwall or hanging-wall direction. We believe such a density function provides a suitable measure of the probability that a secondary fracture undergoes slip which is induced by principal faulting.

For application of the modeling of [P slip|pf] to our logic tree, we prefer to exclude data points for surface cracking from the 1986 Chalfant Valley, California, and the 1980 Mammoth Lakes, California, earthquakes. In both cases, the structural setting of Quaternary volcanic rocks that are affected by distributed faulting (S. K. Pezzopane and T. E. Dawson, USGS, written communication, 1996) arguably confound the composite, two-dimensional frequency-distance distribution being sought. Also, we prefer that the regression modeling of

the data impose a magnitude scaling effect on the hanging wall-footwall relations, which we consider more realistic than having magnitude-invariant relations.

Given that secondary/distributed faulting occurs, our procedures for estimating the amount of displacement and the variability of slip depend on whether the site is one of distributed faulting only (Figure AAR-22) or one where principal faulting also occurs (Figure AAR-23). In the former case, our logic tree uses the same approaches described for the point-estimate method.

At a site where principal faulting also occurs, we chose not to let MD^{max} be an estimator of the expected secondary displacement. In principle, this could result in secondary displacements on faults with large MD^{max} that are larger than the displacements on the primary faults. Instead, we use data summarized by S. K. Pezzopane and T. E. Dawson (USGS, written communication,1996, Figures 9-15 and 9-22) relating observations of maximum secondary displacement to maximum primary displacement as a function of mainshock magnitude. The data include both (1) their own compilation from a sample of surface-faulting earthquakes in the extensional Cordillera of the western U.S. and (2) an earlier compilation from Coppersmith and Youngs (1992; see Figure 9-22 in S. K. Pezzopane and T. E. Dawson, USGS, written communication, 1996). We relied on compilation (1) to estimate a cumulative distribution for the ratio of maximum secondary displacement to maximum primary displacement from which we assessed the following distribution of ratios (and weights):

0.20 (0.3), 0.45 (0.4), 0.70 (0.3).

This distribution is consistent with the assumption by Coppersmith and Youngs (1992) of a uniform distribution between 0.1 and 0.8 for the ratio of maximum secondary displacement to maximum primary displacement (see Figures 9-15 and 9-22 of S. K. Pezzopane and T. E. Dawson, USGS, written communication, 1996).

Given a mainshock of magnitude M, we first estimate the maximum primary displacement MD from the regression relation of Wells and Coppersmith (1994) (See Figure AAR-23). We use the ASM model to estimate the variability of MD on the primary fault. To do this,

we assume MD follows the distribution at the midpoint of the fault, which is the most conservative assumption. The maximum secondary displacement is then calculated from its ratio to MD on the primary fault.

6.12 SECONDARY/DISTRIBUTED FAULTING

We spell out 10 rules for characterizing secondary/distributed faulting at the nine test calculation sites. The rules are grouped under the issues of: (1) susceptibility to displacement; (2) the amount, frequency, and variability of displacement; (3) dip and sense of slip; and (4) the width of the zone of displacement. In terms of notation, recall that P[C] is the probability that a feature is capable of slip to produce secondary/distributed displacement, given the contemporary stress field at Yucca Mountain.

Susceptibility to Displacement:

Rule 1. For any fault assigned P[S] = 1.0 (Tables AAR-2, AAR-3), P[C] is also 1.0.

Rule 2. Based on slip-tendency analysis of Yucca Mountain faults (Morris *et al.*, 1996; H. L. McKague *et al.*, CNWRA, written communication, 1996), and using Figures 3-3 and 3-4 of H. L. McKague *et al.* (CNWRA, written communication, 1996) as a guide for relative scaling, we assign P[C] ranging from 1 for faults with high slip tendency to 0.5 for faults with intermediate slip tendency to 0.1 for faults with low slip tendency, such as the NW-SE striking faults. Although we assigned P[S] = 0 to the latter, we allow some possibility that NW-SE striking structures may undergo secondary/distributed displacement; local stresses may be rotated, for example, during principal faulting nearby.

Rule 3. In an underground excavation at Yucca Mountain, we assign P[C] = 1 to any shears with about 10 cm of cumulative offset or to fractures with less or no measurable offset—concluding that, in principle, they can participate in local strain accommodation, regardless of orientation. We adopt this interpretation because we think it very likely that the underground excavation disrupts the coherency of the stress field used for the slip-tendency analysis.

Rule 4. For intact rock, P[C] = 0.

Secondary displacement of intact rock could occur either by propagation of an existing fault or shear fracture into intact rock or by creation of a new fault. Studies at Yucca Mountain show that existing faults were reactivated during Quaternary deformation. The studies provide no examples of the creation of new faults or of the propagation of existing faults into unbroken rock. There is, therefore, no geologic basis for evaluating the probability that such events may occur.

We consider such displacement may be possible given a condition in which the existing fault or rock block is pre-loaded by regional stress to the point of failure and displacement occurs in response to passage of a transient dynamic stress. We consider such an occurrence at Yucca Mountain to be negligible because: (1) the strength of intact rock is commonly 5 to 10 times greater than that of fault rock (Cowie and Scholz, 1992a), (2) small shear fractures tend to propagate along existing fractures or joints (Segall and Pollard, 1983), (3) the rocks at Yucca Mountain (as revealed in the ESF) are cut by many fractures and faults, some of which (for example, the Ghost Dance fault) are marked by low-strength rock thus providing abundant opportunity for stress release adjacent to intact rock, and (4) there is no indication that the Ghost Dance fault, even with its low strength aspect, has been activated in secondary faulting through several cycles of local Quaternary faulting.

Local evidence for a difference in strength between intact and fractured rock can be interpreted from stress measurements made in the ESF (Sandia National Laboratories, written communication, 1997). Table 1 (p. 7) of that report shows a skewed distribution of critical pressures (Pc) measured at different levels in the test hole. Four values are in the range 1.6 to 1.8 and a fifth is 6.4. The high value is suggested to be typical of intact test intervals as opposed to the lower values which are ascribed to pre-fractured conditions (p. 20). Taking these results to be a crude estimate of strength contrasts between intact and fractured rock, we infer that intact rock is 3.8 times stronger than fractured rock. Although less than the factor of 5 to 10 we cite from Cowie and Scholz (1992a), this nonetheless provides local evidence that intact rock is significantly stronger than fractured rock in the ESF.

Amount, Frequency, and Variability of Displacement:

Rule 5. To estimate the expected amount, frequency, and variability of secondary/distributed faulting on any fault or fracture with measurable offset, our logic tree for "Distributed Faulting" should be followed.

Rule 6. For a fracture with no measurable offset, we adopt the logic of our scaling relation for $\overline{U}$ versus Ltotal, requiring an observer to assess a distribution for Ltotal, combined with our exponential distribution for DE/MDmax. Such a distribution for Ltotal (and weights), for example, might be: 5 m (0.3), 10 m (0.4), 20 m (0.3). For the median value of 10 m, MDmax = 1.32 × 3.69× 10-5 m/m × 10 m, yielding 4.87 ×10-4 m. The expected value of DE is 0.83 * MDmax or 4.0×10-4 m. To place a bound on λDE, the relative frequency of displacement events, one could assume (or assess a distribution otherwise) that "no measurable offset" means ≤ 10 cm for Dcum, in which case the upper bound number of displacement events would be 0.1 m divided by 4.0×10^{-4} m/event yielding 2.5×10^{2} events. Thus, λ_{DE} would be 2.5×10^{2} events divided by the age of the rock. For an age of 12.7 Ma, λ_{DE} would be 2.0×10^{-5} events/yr (recurrence interval = 50,000 yr).

Dip and Sense of Slip:

Rule 7 Begging the obvious, estimating the dip to be expected for displacement at a specific point should clearly rest on either (1) direct observation of the candidate feature and fracturing in its immediate vicinity or (2) inference from either detailed mapping of fractures and faults in the repository excavation similar to mapping in the ESF (e.g., R.C. Lung presentation at SSC Workshop 2) or detailed surface mapping (e.g., presentations by W.C. Day, C.J. Potter, and D.S. Sweetkind at SSC Workshops 3 and 4). Dips of 60° to 90° are well known to predominate.

Rule 8. The sense of slip to be expected on a fault or fracture can reasonably be estimated by relating its 3-D orientation to the 3-D orientations of the contemporary principal stresses at Yucca Mountain (e.g., Stock *et al.*, 1985; Morris *et al.*, 1996; Sandia National Laboratory, written communication, 1997). An interactive computer tool developed for application at Yucca Mountain provides a direct way to assess the "relative likelihood and direction of slip on surfaces of all orientations" (Morris *et al.*, 1996; H. L. McKague *et al.*, CNWRA, written communication, 1996). Such methodologies assume that slip will occur in the absence of strain partitioning involving other faults or fractures in the rock volume under consideration (e.g., Wesnousky and Jones, 1994).

partitioning involving other faults or fractures in the rock volume under consideration (e.g., Wesnousky and Jones, 1994).

Rule 9. For faults or fractures exposed in an underground excavation at Yucca Mountain, we consider that those with dimensions exceeding roughly twice the dimensions of the excavation will have an expected sense of slip controlled by the orientation of the contemporary principal stresses (Rule 8). We have little understanding of how stresses will be induced and modified by the excavation, so we have little confidence in assessing the sense of allowable slip on small fractures intersected by the excavation.

Width of the Zone of Displacement:

Rule 10. The width of the zone of displacement (fault zone thickness), interpreted to be the width of the deformation zone within which most of the slip across a fault or fracture has occurred (as distinct from a broader "damage zone" of deformed rock), scales linearly with fault throw (Knott *et al.*, 1996; Power *et al.*, 1988; Hull, 1988). The mean ratio of fault zone thickness to throw (Dcum) for natural faults is approximately 0.01, with individual values ranging between 0.1 and 0.001 (Power *et al.*, 1988).

The ratio of fault zone thickness to throw is observed to vary with lithology, and within the same lithology to vary greatly along an individual fault trace (Knott *et al.*, 1996). This ratio for the Yucca Mountain faults, in the absence of a compilation for the local fault population, can reasonably be assessed from global data by the following distribution of values (and weights): 0.001 (0.185), 0.01 (0.63), 0.1 (0.185). For illustration, a fault zone thickness of 0.6 to 1.0 m for the Ghost Dance fault observed in Alcove 6 of the ESF (J.W. Whitney presentation, SSC Workshop 6), divided by a throw of the order of 20 to 40 m, gives a ratio of the order of 0.01 to 0.05.

6.13 ASSESSMENTS FOR NINE TEST CALCULATION SITES

In this final section, we give specific guidance for calculating fault-displacement hazard at the Nine Test Calculation Sites.

Point 1 (Bow Ridge fault):

- Susceptibility to slip: Source of principal faulting, P[C] = P[S] = 1
- Amount/frequency/variability of displacement: Logic trees for Principal and Distributed Faulting, respectively (see Table AAR-4 under "total disp." for Dcum)

- Dip/Sense of Slip: Rules 7, 8

- Width of zone of displacement: Rule 10

Point 2 (Solitario Canyon fault):

- Susceptibility to slip: Source of principal faulting, P[C] = P[S] = 1

- Amount/frequency/variability of displacement: Logic trees for Principal and Distributed Faulting, respectively (see Table AAR-4 under "total disp." for Dcum)

- Dip/Sense of Slip: Rules 7, 8

- Width of zone of displacement: Rule 10

Point 3 (Drill Hole Wash fault):

- Susceptibility to slip: Susceptible to secondary/distributed faulting only; P[C] = 0.75 (see H. L. McKague *et al.*, CNWRA, written communication, 1996, Figure 3-4)

- Assessed distribution for L^{total}, in km (and weights): 2.0 (0.3), 5.0 (0.4), 9.0 (0.3); assessed distribution for Dcum, in m (and weights): 20 (0.3), 50 (0.4), 100 (0.3)

- Amount/frequency/variability of displacement: Logic tree for Distributed Faulting

- Dip/Sense of Slip: Rule 7 for dip; Rule 9 for sense of slip in an underground excavation, which reverts to Rule 8 because of the dimension of the fault

- Width of zone of displacement: Rule 10

Point 4 (Ghost Dance fault):

- Susceptibility to slip: Source of principal faulting, P[S] = 0.1; however, based on its high slip susceptibility (see H. L. McKague *et al.*, CNWRA, written communication, 1996, Figure 3-4), we assign P[C] = 1 for secondary/distributed faulting,

- Amount/frequency/variability of displacement: Logic trees for Principal and Distributed Faulting, respectively (see Table AAR-4 under "total disp." for Dcum)

- Dip/Sense of Slip: Rule 7 for dip; Rule 9 for sense of slip in presumed underground excavation, which reverts to Rule 8 because of the dimension of the fault

- Width of zone of displacement: Rule 10

Point 5 (Sundance fault W of ESF):

- Susceptibility to slip: Source of secondary/distributed faulting only; P[C] = 0.8 (see H. L. McKague *et al.*, CNWRA, written communication, 1996)

- Assessed distribution for L^{total}, in km (and weights): 0.5 (0.3), 0.75 (0.4), 2.0 (0.3); assessed distribution for Dcum, in m (and weights): 5 (0.3), 10 (0.4), 20 (0.3)

- Amount/frequency/variability of displacement: Logic tree for Distributed Faulting

- Dip/Sense of Slip: Rule 7 for dip; Rule 9 for sense of slip in presumed underground excavation, which reverts to Rule 8 because of the dimension of the fault

- Width of zone of displacement: Rule 10

Point 6 (Minor unnamed fault W of Dune Wash):

- Susceptibility to slip: Source of principal faulting, P[S] = 0.1; however, based on its high slip susceptibility (see H. L. McKague *et al.*, CNWRA, written communication, 1996, Figure 3-4), we assign P[C] = 0.9 for secondary/distributed faulting

- Amount/frequency/variability of displacement: Logic trees for Principal and Distributed Faulting, respectively. (For fault parameters, see Table AAR-4 for what we call the W. Dune Wash 2 fault, along which Point 6 is located.)

- Dip/Sense of Slip: Rules 7, 8

- Width of zone of displacement: Rule 10

Point 7 (feature 100 m E of Solitario Canyon fault):

(a) Assuming a small fault with 2 meters of cumulative offset not directly identifiable from surface mapping

- Susceptibility to slip: Source of secondary/distributed faulting only; P[C] = 0.9 (assuming northerly orientation similar to major fractures in that neighborhood)
- Amount/frequency/variability of displacement: Logic tree for Distributed Faulting
- Dip/Sense of Slip: Rule 7 for slip, Rule 9 for sense of slip in underground excavation, which reverts to Rule 8 because of the inferred length dimension of the fault
- Width of zone of displacement: Rule 10

(b) Assuming a shear with about 10 cm of cumulative offset

- Susceptibility to slip: Susceptible to secondary/distributed displacement only; P[C] = 1 (Rule 3)
- Amount/frequency/variability of displacement: Logic tree for Distributed Faulting
- Dip/Sense of Slip: Rule 7 for slip, Rule 9 for sense of slip (uncertain for small fracture in underground excavation)
- Width of zone of displacement: Rule 10

(c) Assuming a fracture with no measurable offset

- Susceptibility to slip: Susceptible to secondary/distributed displacement only; P[C] = 1 (Rule 3)
- Amount/frequency/variability of displacement: Rule 6
- Dip/Sense of Slip: Rule 7 for slip, Rule 9 for sense of slip (uncertain for small fracture in underground excavation)
- Width of zone of displacement: Rule 10

(d) Assuming intact rock

- Susceptibility to slip: No expected displacement (Rule 4)

- Amount/frequency/variability of displacement: N/A

Point 8 (Feature midway between Solitario Canyon and Ghost Dance faults):
[Except for not knowing the orientation of the feature, all assessments would be identical to those for Point 7 (a-d). The only factor that might change would be P[C] in assumption (a)—if the orientation implied higher or lower susceptibility than P[C] = 0.9 assigned for Point 7(a).]

Point 9 (Site on alluvium in Midway Valley E of the Bow Ridge fault):
All arguments heretofore assume accessibility to direct observations of a fault or fracture in order to assess MD^{max}. Nevertheless, we can proceed as follows:

- Susceptibility to slip: Figure 3-4 of H. L. McKague *et al.* (CNWRA, written communication, 1996) indicates faults/fractures in this vicinity with slip tendencies varying from high to low, so we assume uniform probability of P[C] between 0.1 and 1.0

Amount/frequency/variability of displacement: To assess displacement parameters, we can rule out (from earlier site characterization studies) the presence of a shallowly buried principal fault. We then assess that the most significant shallowly buried intrablock feature at that site has Dcum as follows:

2 m (5%) 10 m (50%) 20 m (95%)

- Given the above distribution for Dcum, follow the logic tree for Distributed Faulting

- Dip/sense of slip: Under the present stress field, the faults most favorably oriented for slip would have strikes of N0°E to N30°E, dips of 60° to 90°, and normal-slip motion with a sinistral component (Morris *et al.*, 1996)

- Width of zone of displacement: Rule 10

7.0
REFERENCES

Abercrombie, R.E., 1995, Earthquake source scaling relationships from -1 to 5 M_L using seismograms recorded at 2.5-km depth: Journal of Geophysical Research, v. 100, n. B12, p. 24,015-24,036.

Anderson, J.G., Wesnousky, S.G., and Stirling, M.W., 1996, Earthquake size as a function of fault slip rate: Bulletin of the Seismological Society of America, v. 86, n. 3, p. 683-690.

Anderson, R.E., Barnhard, T.P., and Snee, L.W., 1994, Roles of plutonism, midcrustal flow, tectonic rafting, and horizontal collapse in shaping the Miocene strain field of the Lake Mead area, Nevada and Arizona: Tectonics, v. 13, p. 1381-1410.

Anderson, R.E, Bucknam, R.C., Crone, A.J., Haller, K.M., Machette, M.N., Personius, S.F., Barnhard, T.P., Cecil, M.J., and Dart, R.L., 1995a, Characterization of Quaternary and suspected Quaternary faults, regional studies, Nevada and California: U.S. Geological Survey Open-File Report 95-599, 56 p.

Anderson, R.E., Crone, A.J., Machette, M.N., Bradley, L.-A., and Diehl, S.F., 1995b, Characterization of Quaternary and suspected Quaternary faults, Amargosa area, Nevada and California: U.S. Geological Survey Open-File Report 95-613, 41 p.

Bell, J.W., de Polo, C.M., Ramelli, A.R., Dorn, R.I., Sarna-Wojcicki, A.M., and Meyer, C.E., 1996, Surface faulting and paleoseismic history of the 1932 Cedar Mountain earthquake area, Central Nevada: Geological Society of American Bulletin (in press).

Benjamin, J.R., and Cornell, C.A., 1970, Probability, statistics, and decision for civil engineers: New York, McGraw-Hill Book Company, 684 p.

Bodin, P., and Brune, J.J., 1996, On the scaling of slip with rupture length for shallow strike-slip earthquakes: Quasi-static models and dynamic rupture propagation: bulletin of Seismological Society of America, v. 86, n. 5, p. 1292-1299.

Clark, R.M., and Cox, S.J.D., 1996, A modern regression approach to determining fault displacement-length scaling relationships: Journal of Structural Geology, v. 18, n. 2/3, p. 147-152.

Cohee, B.P., and Beroza, G.C., 1994, Slip distribution of the 1992 Landers earthquake and its implications for earthquake source mechanics: Bulletin of the Seismological Society of America, v. 84, n. 3, p. 692-712.

Coppersmith, K.J., and Youngs, R.R., 1992, Earthquakes and tectonics, *in* McGuire, R.K., ed., Demonstration of a Risk-Based Approach to High-Level Waste Repository Evaluation: Phase 2, Electric Power Research Institute, EPRI TR-100384, Palo Alto, California

Cowie, P. A., and Scholz, C.H., 1992a, Physical explanation for the displacement-length relationship of faults using a post-yield fracture mechanics model: Journal of Structural Geology, v. 14, n. 10, p. 1133-1148.

Cowie, P. A., and Scholz, C.H., 1992b, Displacement-length scaling relationships for faults: data synthesis and discussion: Journal of Structural Geology, v. 14, n. 10, p. 1149-1156

Cowie, P. A., and Scholz, C.H., 1992c, Growth of faults by accumulation of seismic slip: Journal of Geophysical Research, v. 97, n. B7, p. 11,085-11,095.

Ferrill, D.A., Stamatakos, J.A., Jones, S.M., Rahe, B., McKague, H.L., Martin, R.H., and Morris, A.P., 1996, Quaternary slip history of the Bare Mountain Fault (Nevada) from the morphology and distribution of alluvial fan deposits: Geology, v. 24, n. 6, p. 559-562.

Fridrich, C.J., 1996, Tectonic evolution of the Crater Flat basin, Yucca Mountain region, Nevada, *in* Wright, L. and Troxel, B., eds., Cenozoic basins of the Death Valley region: Geological Society of America Special Paper (in press).

Fridrich, C.J., Whitney, J.W., Hudson, M.R., and Crowe, B.M., 1996, Late Cenozoic extension, vertical-axis rotation, and volcanism in the Crater Flat basin, southwest Nevada, in Wright, L. and Troxel, B. eds., Cenozoic basins of the Death Valley region: Geological Society of America Special Paper (in press).

Frizzell, V.A., Jr., and Shulters, J., 1990, Geologic map of the Nevada Test Site, southern Nevada: U.S. Geological Survey Miscellaneous Investigations Map I-2046, scale 1:100,000.

Frizzell, V.A. and Zoback, M.L., 1987, Stress orientation determined from fault slip data in Hampel Wash area, Nevada, and its relation to contemporary regional stress field: Tectonics, v. 6, p. 89-98.

Gomberg, J., 1996, Stress/strain changes and triggered seismicity following the M_w7.3 Landers, California earthquake: Journal of Geophysical Research, v. 101, n. B1, p. 751-764.

Gomberg, J., Blanpied, M.L., and Beeler, N.M., 1997, Transient triggering of near and distant earthquakes: Bulletin of Seismological Society of America, v. 87, n. 2, p. 294-309.

Gomberg, J., and Bodin, 1994, Triggering of the Ms = 5.4 Little Skull Mountain, Nevada, earthquake with dynamic strains: Bulletin of the Seismological Society of America, v. 84, n. 3, p. 844-853.

Gomberg, J., and Davis, S., 1996, Stress/strain changes and triggered siesmicity at The Geysers, California: Journal of Geophysical Research, v. 101, n. B1, p. 733-749.

Harmsen, S.C., 1994, The Little Skull Mountain, Nevada, earthquake of 29 June 1992: Aftershock focal mechanisms and tectonic stress field implications: Bulletin of the Seismological Society of America, v. 84, n. 5, p. 1484-1505.

Hull, J., 1988, Thickness-displacement relationships for deformation zones: Journal of Structural Geology, v. 10, n. 4, p. 431-435.

Keefer, D.I., and Bodily, S.E., 1983, Three-point approximations for continuous random variables: Management Science, v. 26, p. 595-609.

King, G.C.P., Stein, R.S., and Lin, J., 1994, Static stress changes and the triggering of earthquakes: Bulletin of the Seismological Society of America, v. 84, n. 3, p. 935-953.

Knott, S.D., Beach, Alastair, Brockbank, P.J., Brown, J.L., McCallum, J.E., and Welbon, A.J., 1996, Spatial and mechanical controls on normal fault populations: Journal of Structural Geology, v. 18, n. 2/3, p. 359-372.

Maldonado, F., 1985, Geologic map of the Jackass Flats area, Nye County, Nevada: U.S. Geological Survey, Miscellaneous Investigations Map I-1519, scale 1:48,000.

Mendoza, C., and Hartzell, S.H., 1988, Inversion for slip distribution using teleseismic P-waveforms: North Palm Springs, Borah Peak, and Michoacan earthquakes: Bulletin of the Seismological Society of America, v. 78, n. 3, p. 1092-1111.

Morris, A., Ferrill, D.A., and Henderson, D.B., 1996, Slip-tendency analysis and fault reactivation: Geology, v. 24, n. 3, p. 275-278.

Nicol, A., Watterson, J., Walsh, J.J., and Childs, C., 1996, The shapes, major axis orientations and displacement patterns of fault surfaces: Journal of Structural Geology, v. 18, n. 2/3, p. 235-248.

Parsons, T., and Thompson, G.A., 1991, Coupled processes of normal faulting and dike intrusion in tectonically extended regions: Geological Society of America, Abstracts with Programs, v. 23, n. 2, p. 87.

Piety, L.A., 1996, Compilation of known and suspected Quaternary faults within 100 km of Yucca Mountain: U.S. Geological Survey Open-File Report 94-112, 31 p.

Power, W.T., Tullis, T.E., and Weeks, J.D., 1988, Roughness and wear during brittle faulting: Journal of Geophysical Research, v. 93, n. B12, p. 15,268-15,278.

Rogers, A.M., Harmsen, S.C., and Meremonte, M.E., 1987, Evaluation of the seismicity of the southern Great Basin and its relationship to the tectonic framework of the region: U.S. Geological Survey Open-File Report 87-408, 196 p.

Rogers, A.M., Harmsen, S.C., Corbett, E.J., Priestley, K., and dePolo, D., 1991, The seismicity of Nevada and some adjacent parts of the Great Basin, *in* Slemmons, D.B., Engdahl, E.R., Zoback, M.D., and Blackwell, D.D., eds., Neotectonics of North America: Boulder, Colorado, Geological Society of America, Decade Map Volume 1, p. 153-184.

Romanowicz, B., and Rundle, J.B., 1993, On scaling relations for large earthquakes: Bulletin of the Seismological Society of America, v. 83, n. 4, p. 1294-1297.

Scott, R.B., 1990, Tectonic setting of Yucca Mountain, southwest Nevada, *in* Wernicke, B.P., ed., Basin and Range extensional tectonics near the latitude of Las Vegas, Nevada: Geological Society of America Memoir 176, p. 251-282.

Scott, R.B., and Bonk, J., 1984, Preliminary geologic map of Yucca Mountain, Nye County, Nevada with geologic sections: U.S. Geological Survey Open-File Report 84-494, 9 p., scale 1:12,000.

Segall, P., and Pollard, D.D., 1983, Nucleation and growth of strike slip faults in granite: Journal of Geophysical Research, v. 88, n. B1, p. 555-568.

Simonds, W.F., Whitney, J.W., Fox, K.F., Ramelli, A., Yount, J., Carr, M.D., Menges, C.M., Dickerson, R., and Scott, R.B., 1995, Map of fault activity of the Yucca Mountain area, Nye County, Nevada: U.S. Geological Survey Miscellaneous Investigations Series Map I-2520, scale 1:24,000.

Simpson, R.W., and Reasenberg, P.A., 1994, Earthquake-induced static-stress changes on central California faults, *in* Simpson, R.W., ed., The Loma Prieta, California, Earthquake of October 17, 1989—Tectonic Processes and Models: U.S. Geological Survey Professional Paper 1550-F, p. F55-F89.

Smith, R.P., Jackson, S.M., and Hackett, W.R., 1995, Method for estimating the maximum magnitudes of earthquakes associated with potential dike intrusion and basaltic volcanism in the Yucca Mountain area: Implications for seismic hazards assessment, *in* Proceedings, Topical Meeting on Methods of Seismic Hazards Evaluation, Focus '95: American Nuclear Society, Inc., La Grange Park, Illinois, p. 178-184.

Smith, R.P., Jackson, S.M., and Hackett, W.R., 1996, Paleoseismology and seismic hazards evaluations in extensional volcanic terrains: Journal of Geophysical Research, v. 101, n. B3, p. 6277-6292.

Sonder, L.J., Jones, C.H., Salyards, S.L., and Murphy, K.M., 1994, Vertical-axis rotations in the Las Vegas Valley Shear Zone, southern Nevada: Paleomagnetic constraints on kinematics and dynamics of block rotations: Tectonics, v. 13, p. 769-788.

Stewart, J.H., and Diamond, D.S., 1990, Changing patterns of extensional tectonics; Overprinting of the basin of the middle and upper Miocene Esmeralda Formation in western Nevada by younger structural basins, *in* Wernicke, B.P., ed., Basin and Range extensional tectonics near the latitude of Las Vegas, Nevada: Geological Society of America Memoir 176, p. 447-475.

Stock, J.M., Healy, J.H., Hickman, S.H., and Zoback, M.D., 1985, Hydraulic fracturing stress measurements at Yucca Mountain, Nevada, and relationship to regional stress field: Journal of Geophysical Research, v. 90, n. B10, p. 8691-8706.

Veneziano, D., and Van Dyck, J., 1985, Statistical discrimination of "aftershocks" and their contribution to seismic hazard, seismic hazard, *in* Methodology for Nuclear Facilities in the Eastern United States: EPRI Research Project N. P101-29, EPRI/SOG 85-1, v. 2, Appendix A-4.

Wald, D.J., and Heaton, T.H., 1994, Spatial and temporal distribution of slip for the 1992 Landers, California, earthquake: Bulletin of the Seismological Society of America, v. 84, n. 3, p. 668-691.

Wells, D.L., and Coppersmith, K.J., 1994, New empirical relationships among magnitude, rupture length, rupture width, rupture area, and surface displacement: Bulletin of the Seismological Society of America, v. 84, n. 4, p. 974-1002.

Wesnousky, S.G., and Jones, C.H., 1994, Oblique slip, slip partitioning, spatial and temporal changes in the regional stress field, and the relative strength of active faults in the Basin and Range, western United States: Geology, v. 22, n. 11, p. 1031-1034.

Yeats, R.S., Sieh, K., and Allen, C.R., 1997, The geology of earthquakes: Oxford University Press, New York, 568 p.

Youngs, R.R., and Coppersmith, K.J., 1985, Implications of fault slip rates and earthquake recurrence models to probabilistic seismic hazard estimates: Bulletin of the Seismological Society of America, v. 75, n. 4, p. 939-964.

Youngs, R.R., Swan, III, F.H., Power, M.S., Schwartz, D.P, and Green, R.K., 1987, Probabilistic analysis of earthquake ground shaking hazard along the Wasatch Front, Utah, *in* Gori, P.L., and Hays, W.W., eds., Assessment of regional earthquake hazards and risk along the Wasatch Front, Utah: U.S. Geological Survey Open File Report 87-585, p. M-1 to M-110.

TABLE AAR-1
SEISMIC SOURCE PARAMETERS FOR REGIONAL FAULT SOURCES
(p. 1 of 2)

Fault Name	Total Fault Length [1] (km)	Max. Rupture Length [1] (km)	Min. Distance to Rep. (km)	Doc. Quaternary Displacement	Style	Dip [1] (deg.)	Slip Rate [1] (mm/yr)	Recur. Int.[1] (ka)	P[S]
Mine Mountain (MM)	20 23 37	20 23 37	11	y?	LO	50 70 90	0.002 0.015 0.03		0.6
Wahmoni (WAH)	11 14 17	11 14 17	22	y	N/L	50 65 90	0.002 0.025 0.05		1
Ash Meadows (AM)	8 42 72	8 42 72	24	y	N	50 65 80	0.001 0.01 0.1		1
Oasis Valley (OSV)	8 19 29	8 19 29	24	y?	N	50 65 80	0.001 0.005 0.01		0.4
Rock Valley (RV)	25 33 69	25 33 46	25	y	LO	65 90 90	0.02 0.06 0.1	33 50 180	1
Cane Spring (CS)	18 22 36	18 22 36	29	y?	LO?	65 90 90	0.002 0.025 0.05		0.6
West Specter R. (WSR)	7 8 22	7 8 22	33	y	N	45 60 80	0.001 0.004 0.01		1
Amargosa R./ Pahrump (AR/PRP)	75 82 134	75 82 110	34	y	R?	80 90 90	0.005 0.07 0.2		1
Amargosa R. (AR)	13 14 25	13 14 25	34	y	NR	80 90 90	0.005 0.04 0.2		1
Yucca Lake (YCL)	12 14 24	12 14 24	36	y?	N	45 60 80	0.001 0.005 0.01		0.5
Eleana Range (ER)	11 13 18	11 13 18	37	y	N	45 60 80	0.001 0.005 0.01		1

TABLE AAR-1
SEISMIC SOURCE PARAMETERS FOR REGIONAL FAULT SOURCES
(p. 2 of 2)

Fault Name	Total Fault Length [1] (km)	Max. Rupture Length [1] (km)	Min. Distance to Rep. (km)	Doc. Quaternary Displacement	Style	Dip [1] (deg.)	Slip Rate [1] (mm/yr)	Recur. Int.[1] (ka)	P[S]
Yucca Fault (YC)	20 25 31	20 25 31	40	y	N/RO	50 65 90	0.001 0.025 0.05		1
Keane Wonder (KW)	19 23 32	19 23 32	43	y?	N	50 65 85	0.001 0.005 0.01		0.6
Furnace Creek (FC)	100 118 146	100 118 146	50	y	R	80 90 90	2.3 8.0 10.0	0.5 0.7 1.0	1
Death Valley/ Furnace Creek (DV/FC)	154 178 193	125 150 165	50	y	N/R	50 82 90	2.3 8.0 10.0	0.5 0.7 1.0	1
West Spring Mts. (WSM)	37 52 66	23 37 48	53	y	N	50 65 80	0.02 0.05 0.07	28 30 124	1
Death Valley (DV)	42 57 74	42 57 74	55	y	N	50 65 90	3.0 4.0 5.0	0.5 0.75 1.3	1
Belted Range (BLR)	21 29 50	21 29 45	55	y	N	50 65 80	0.02 0.05 0.1		1
Kawich Range (KR)	20 27 76	20 27 45	57	y	N	50 65 80	0.005 0.03 0.07		1
Pahrump (PRP)	37 45 107	37 45 85	68	y	R	80 90 90	0.005 0.07 0.2		1
West Pintwater (WPR)	30 48 57	30 48 57	76	y	N	45 60 80	0.002 0.04 0.07		1

[1] Three numbers represent minimum, preferred, and maximum values

TABLE AAR-2
SOURCE INVENTORIES

Model [?]	Local Seismic Source	P[s][›]
A-1, A-2, A-3	CFD faults [*]	*
	Highway 95 fault (H95)	0.5
	Regional ss (subjacent) (T4-SS)	1.0
	Background source zones	1.0
B-1, B-2, B-3	CFD faults *	*
	Highway 95 fault (H95)	0.8
	No. bounding ss fault (T4-PA2)	0.5
	Background source zones	1.0
C-1, C-2	CFD faults *	*
	Highway 95 fault (H95)	0.8
	No. bounding ss fault (T4-PA2)	0.5
	Cross-basin fault (T4-CB)	1.0
	Background source zones	1.0
D-1, D-2, D-3	CFD faults *	*
	Background sources	1.0

[?] Keyed to Figure AAR-1
[›] Probability of being seismogenic
[*] See Table AAR-3

TABLE AAR-3
INVENTORY OF CRATER FLAT DOMAIN (CFD) FAULTS

FAULT	P[s]'
Bare Mountain	1.0
Bow Ridge	1.0
S. Crater Flat	1.0
N. Crater Flat	1.0
W. Dune Wash #1	0.1
W. Dune Wash #2	0.1
Ghost Dance	0.1
Fatigue Wash	1.0
Iron Ridge	1.0
E. Lathrop Cone	1.0
Midway Valley	0.1
Paintbrush Canyon	1.0
Solitario Canyon	1.0
Stagecoach Road	1.0
S. Windy Wash	1.0
N. Windy Wash	1.0
C. Windy Wash	0.6
C. Crater Flat	0.6
Black Cone	0.8
E. Busted Butte	0.4

' Probability of being seismogenic. P[S] for each fault is constant for all the logic tree branches outlined in Table AAR-2 and Figure AAR-1

TABLE AAR-4
ESTIMATES OF FAULT PARAMETERS FOR LOCAL FAULT SOURCES
(p. 1 OF 3)

fault name	act length [1] (km)	doc. Quat act?	styl	fault dip [1] (deg)	total disp. [1] (m)	disp./event Dmax [1] (cm)	disp./event Davg [1] (cm)	slip rate [1] (mm/yr)	rec. int. [1] (ka)
Independent down-to-west faults									
	17			50	2500	120	80	0.005	200
Bare Mountain	21	Y	n	60	3000	150	120	0.01	100
(BM)	31			70	4000	180	160	0.25	30
	4			50	100	20	20	0.002	200
Bow Ridge	8	Y	In	60	200	40	40	0.003	120
(BWR)	10			70	300	60	60	0.007	70
	6			50	40	30	30	0.002	150
S. Crater Flat	8	Y	In?	70	300	50	50	0.008	80
(SCF)	14			80	600	70	70	0.02	40
	5			50	100	30	30	0.001	
N. Crater Flat	8	Y	In?	60	200	50	50	0.003	
(NCF)	10			70	300	70	70	0.005	
	3			70	50	10	10	0.0001	
W. Dune Wash 1	7	N?	In?	80	100	20	20	0.0005	
(WD1)	10			90	200	30	30	0.001	
	2			60	30	5	5	0.0001	
Ghost Dance	2.5	Y?	In	70	40	10	10	0.0005	
(GD)	7			80	50	15	15	0.001	
	6.5			50	70	30	30	0.003	
Fatigue Wash	9.5	Y	In	60	200	50	50	0.009	
(FW)	14			70	400	70	70	0.02	
	4.5			50	200	10	10	0.001	
Iron Ridge	6.5	Y	In?	60	250	50	50	0.002	
(IR)	9			70	400	80	80	0.005	
	1.5			50	50	30	30	0.005	
E. Lathrop Cone	4	Y	In?	65	100	50	50	0.01	
(ELC)	9			80	200	80	80	0.03	
	3			60	30	10	10	0.0001	
Midway Valley	4	N	In?	70	50	20	20	0.0005	
(MWV)	8			80	70	30	30	0.001	
	8			50	300	100	40	0.01	200
Paintbrush Cyn	12	Y	In	60	500	150	90	0.015	60
(PBC)	25			70	700	250	130	0.03	30
	13.5			50	400	70	50	0.005	100
Solitario Cyn	16	Y	In	60	700	100	80	0.01	60
(SC)	25			70	1000	130	110	0.02	35
	3.5			50	300	50	50	0.01	40
Stagecoach Road	4.5	Y	In?	60	500	70	70	0.04	20
(SR)	8			70	700	100	100	0.07	5
	8			50	300	50	50	0.01	60
S. Windy Wash	9	Y	In	60	500	70	70	0.03	40
(SWW)	12			70	700	90	90	0.04	20

TABLE AAR-4
ESTIMATES OF FAULT PARAMETERS FOR LOCAL FAULTS SOURCES
(P. 2 OF 3)

fault name	act length [1] (km)	doc. Quat act?	styl	fault dip [1] (deg)	total disp. [1] (m)	disp./event Dmax [1] (cm)	disp./event Davg [1] (cm)	slip rate [1] (mm/yr)	rec. int. [1] (ka)
Independent down-to-west faults (cont'd.)									
N. Windy Wash	7			50	300	30	30	0.001	
(NWW)	8	Y	ln?	60	400	50	50	0.003	
	10			70	600	70	70	0.005	
Independent down-to-east faults									
Black Cone	3.5			50		10	10	0.001	
(BC)	8	Y	rn?	65		30	30	0.003	
	12			80		50	50	0.005	
	1.5			50	200	10	10	0.0005	
E. Busted Butte	4	Y	n?	60	400	30	30	0.001	
(EB)	11			70	600	50	50	0.003	
	3			50		10	10	0.001	
C. Crater Flat	6.5	Y	n?	65		30	30	0.003	
(CCF)	8			80		50	50	0.005	
	1.5			70	100	10	10	0.0001	
W. Dune Wash 2	3	N?	n?	80	150	20	20	0.0005	
(WD2)	5			90	200	30	30	0.001	
	4			50		10	10	0.001	
C. Windy Wash	5	Y	n?	65		30	30	0.003	
(CWW)	6			80		50	50	0.005	
Linked systems									
	14			50	300	100	40	0.01	120
PBC/SR	18	Y	ln	60	500	150	90	0.04	40
	32			70	700	250	130	0.07	15
	21			50	300	50	50	0.01	60
SWW/FW/CWW/NWW	23	Y	ln	60	500	70	70	0.03	40
	28			70	700	90	90	0.04	20
Coalesced systems									
	22			50	300	100	40	0.01	120
E-side	24	Y	ln	60	500	150	90	0.04	40
	36			70	700	250	130	0.07	15
	13.5			50	400	70	30	0.005	100
W-side #1	16	Y	ln	60	700	100	60	0.01	60
	25			70	1000	130	90	0.02	35
	21			50	300	70	70	0.01	60
W-side #2	23	Y	ln	60	500	110	110	0.04	40
	29			70	700	150	150	0.06	20

TABLE AAR-4
ESTIMATES OF FAULT PARAMETERS FOR LOCAL FAULTS SOURCES
(P. 3 OF 3)

Multiple-structure coalesced systems (length & recurrence)

fault name	act leng [1] (km)	rec. int. [1] (ka)
Single	35	100
W-side	39	60
(W-side1+W-side2)	54	35
Single	57	120
YM system	63	60
(E-side+W-Side1 +W-side2)	907	35
Single	74	200
system	84	100
(YM+BM)	121	35

fault name	active length [1] (km)	doc Q actv?	style	fault dip [1] (deg.)	disp./event Dmax [1] (cm)	disp./event Davg [1] (cm)	slip rate [1] (m/ka)
Buried/bounding strike-slip (ss) faults							
	50			70	200	200	0.05
Regional ss fault	75	N	rl	90	400	400	0.1
(T4-ss)	100			90	600	600	0.2
No. bounding ss fault	10			70	30	30	0.005
(T4-PA2)	20	N	rl	90	80	80	0.01
	30			90	130	130	0.05
	20			60	50	50	0.02
Hwy.95 fault	40	N?	rl	80	150	150	0.05
(H95)	60			90	250	250	0.1
	10			70	30	30	0.005
Cross-basin fault	20	N	rl	90	80	80	0.01
(T4-CB)	30			90	130	130	0.05

[1] Three numbers represent minimum, preferred, and maximum values.

TABLE AAR-5
WEIGHTS FOR BEHAVIOR OF LOCAL FAULTS DEPENDING ON TECTONIC MODELS

Behavior	A1	A2	A3	B1	B2	B3	C1	C2	D1	D2	D3
Independent	0.1	0.2	0.2	0.1	0.2	0.2	0.1	0.6	0.1	0.2	0.2
Coalesced	0.9	0.8	0.8	0.9	0.8	0.8	0.9	0.4	0.9	0.8	0.8

TABLE AAR-6
WEIGHTS FOR LINKED OPTIONS GIVEN INDEPENDENT BEHAVIOR,

	A1	A2	A3	B1	B2	B3	C1	C2	D1	D2	D3
PBC/SR:											
Independent	0.4	0.2	0.2	0.4	0.2	0.2	0.4	0.5	0.4	0.2	0.2
Linked	0.6	0.8	0.8	0.6	0.8	0.8	0.6	0.5	0.6	0.8	0.8
WW/FW:											
Independent	0.5	0.4	0.4	0.5	0.4	0.4	0.5	0.7	0.5	0.4	0.4
Linked	0.5	0.6	0.6	0.5	0.6	0.6	0.5	0.3	0.5	0.6	0.6

- PBC/SR includes Paintbrush and Stagecoach Road faults.
- WW/FW includes So. Windy Wash, Fatigue Wash, Central Windy Wash, and No. Windy Wash faults. CWW is antithetic to the subparallel FW. Estimates for this linked system are primarily derived from SWW, the most active of the four faults.

TABLE AAR-7

WEIGHTS FOR COALESCED MODELS GIVEN COALESCED BEHAVIOR

Coalesced model	A1	A2	A3	B1	B2	B3	C1	C2	D1	D2	D3
1 system	0.2	0.0	0.0	0.0	0.0	0.0	0.1	0.0	0.0	0.0	0.0
2 systems 0.2	0.0	0.0	0.0	0.0	0.0	0.2	0.0	0.0	0.0	0.0	
3 systems 0.3	0.4	0.4	0.3	0.2	0.2	0.3	0.1	0.3	0.2	0.2	
4 systems 0.3	0.6	0.6	0.7	0.8	0.8	0.4	0.9	0.7	0.8	0.8	

TABLE AAR-8
WEIGHTS FOR M_{max} APPROACHES—LOCAL FAULT SOURCES

Expected Rupture Length <25 km:

Approach	Weight
a. Rupture length	0.3
b. Rupture area	0.2
c. Rupture length/slip rate	0.2
d. Moment equation	0.3

Expected Rupture Length ≥25 km:

Approach	Weight
a. Rupture length	0.3
b. Rupture area	0.0
c. Rupture length/slip rate	0.2
d. Moment equation	0.5

Exception #1: For scenarios A-1, B-1, C-1, and D-1 (local detachment at 3-10 km depth), use these weights for all CFD faults other than the Bare Mountain fault:

Approach	Weight
a. Rupture length	0.1
b. Rupture area	0.2
c. Rupture length/slip rate	0.1
d. Moment equation	0.6

Exception #2: For "multiple-structure coalesced systems" (which have no slip rates provided in Table AAR-4), use these weights:

Approach	Weight
a. Rupture length	0.5
b. Rupture area	0.2
c. Rupture length/slip rate	0.0
d. Moment equation	0.3

TABLE AAR-9
REGRESSION RELATIONS

Equation	Number of Data Points	Coefficients and Standard Errors a (sa)	b (sb)	Standard Deviation	Correlation Coefficient	Range of Variables Independent	Dependent
1. $\log \overline{U} = \log b + \log L^{total}$ [m/m]	19		log b = -4.433 (0.041)	0.18	n.d.	3.3 to 21.3 km	0.08 to 1.14 m
2. log (Dcum) = a + b (log L^{total}) [m/m]	16	-1.58 (1.37)	1.00*	0.32	0.61	3.3 to 21.3 km	40 to 700 m
3. QSR = a + b Dcum [mm/yr/m]	11	0*	3.26 (1.72) e-05	0.01	0.58	40 to 700 m	0.0005 to 0.04 m/yr
4. PDF = a * exp (b * D/MD^{max})	19	0.09 (0.02)	-0.68 (0.16)	1.88	-0.70	0.1 to 2.9	0.01 to 0.14
5. CDF = 1 - exp (-λ * D/MD^{max})	82	λ = 1.20 (0.13)		0.69	n.d.	0.1 to 2.9	0.14 to 1.00

* Constrained

Table AAR-10
Displacement Data Used for Figure AAR-11

FAULT	TRENCH	MD^{max} (cm)	D obs (cm)/ D/MD^{max}	D obs (cm)/ D/MD^{max}	D obs (cm)/ D/MD^{max}	D obs (cm)/ D/MD^{max}	D obs (cm)/ D/MD^{max}	D obs (cm)/ D/MD^{max}	D obs (cm)/ D/MD^{max}	D obs (cm)/ D/MD^{max}
BR	14D	40.92	44 1.08	13 0.32	14 0.34					
NCF	CFF-T2a	46.79	3 0.06	5 0.11	40 0.85	50 1.07	50 1.07			
SCF	CFF-T1a	52.77	18 0.34	10 0.19	20 0.38					
FW	CF 1	49.59	25 0.50	105 2.12	54 1.09					
IR	SCF-T2	46.98	5 0.11	70 1.49	100 2.13	70 1.49				
PB	A1	114.07	6 0.05	39 0.34	7 0.06	100 0.88				
PB	BB4	114.07	44 0.39	28 0.25	47 0.41	167 1.46	142 1.24	105 0.92	94 0.82	
PB	MWV-T4	114.07	20 0.18	62 0.54	98 0.86	40 0.35				
SC	SCF-T1	111.64	10 0.09	70 0.63						
SC	SCF-T3	111.64	10 0.09	80 0.72	35 0.31					
SC	SCF-T4	111.64	5 0.04	30 0.27	20 0.18					
SC	SCF-T8	111.64	10 0.09	120 1.07	30 0.27	50 0.45				
SCR	SCR-T1	66.21	40 0.60	42 0.63	47 0.71	51 0.77				
SCR	SCR-T3	66.21	43 0.65	59 0.89	57 0.86	67 1.01	35 0.53			
WW	CF-2 northwall	30.34	4 0.13	20 0.66	23 0.76	20 0.66	73 2.41	45 1.48	50 1.65	80 2.64
WW	CF-2 southwall	30.34	4 0.13	12 0.40	50 1.65	42 1.38	28 0.92	16 0.53	60 1.98	65 2.14
WW	CF-2.5	30.34	6 0.20	20 0.66	42 1.38	15 0.49				
WW	CF-3 northwall	30.34	4 0.13	33 1.09	87 2.87	35 1.15	65 2.14			
WW	CF-3 southwall	30.34	3 0.10	35 1.15	88 2.90					

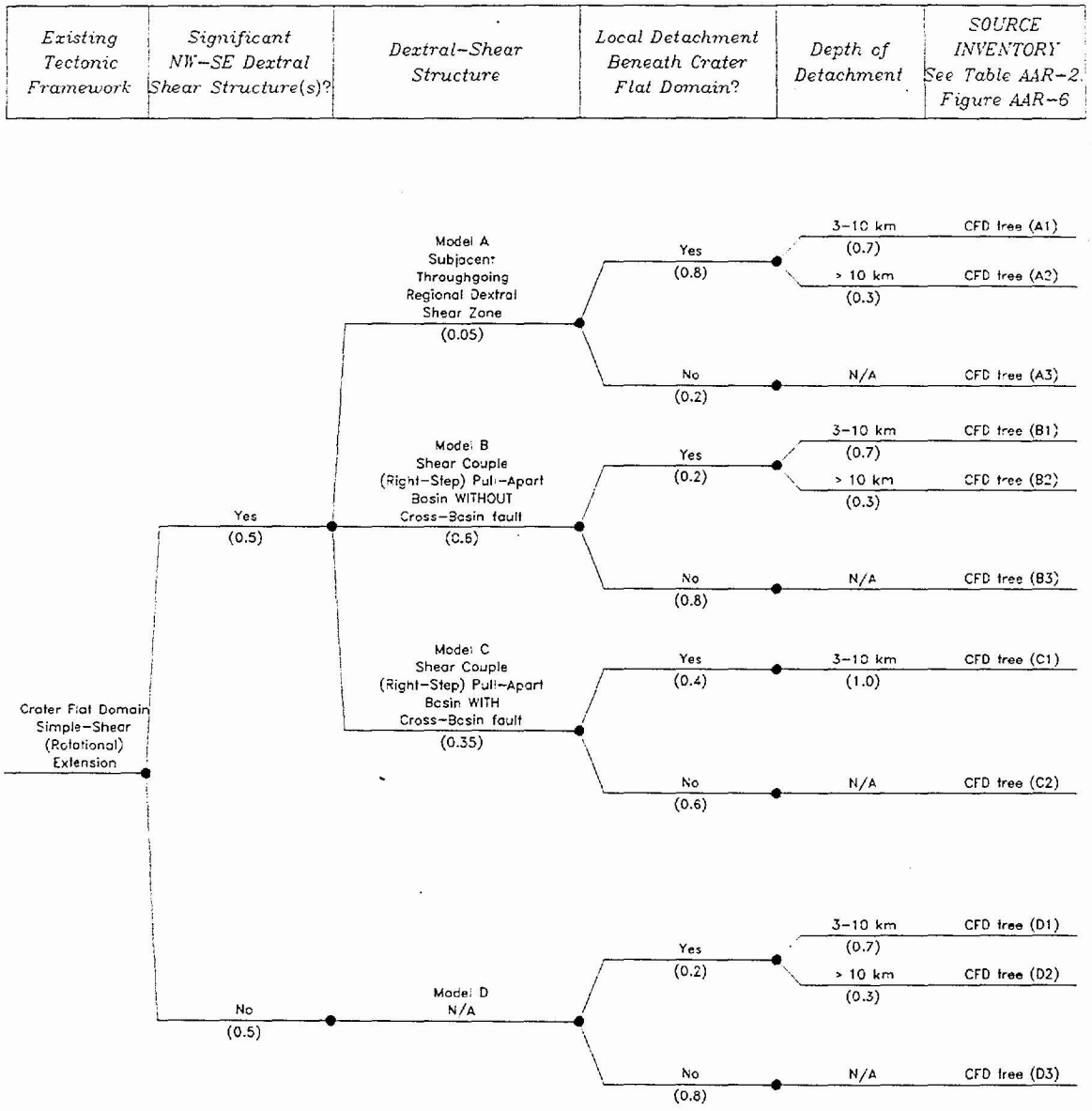

Figure AAR-1 Logic tree for tectonic models and local faults

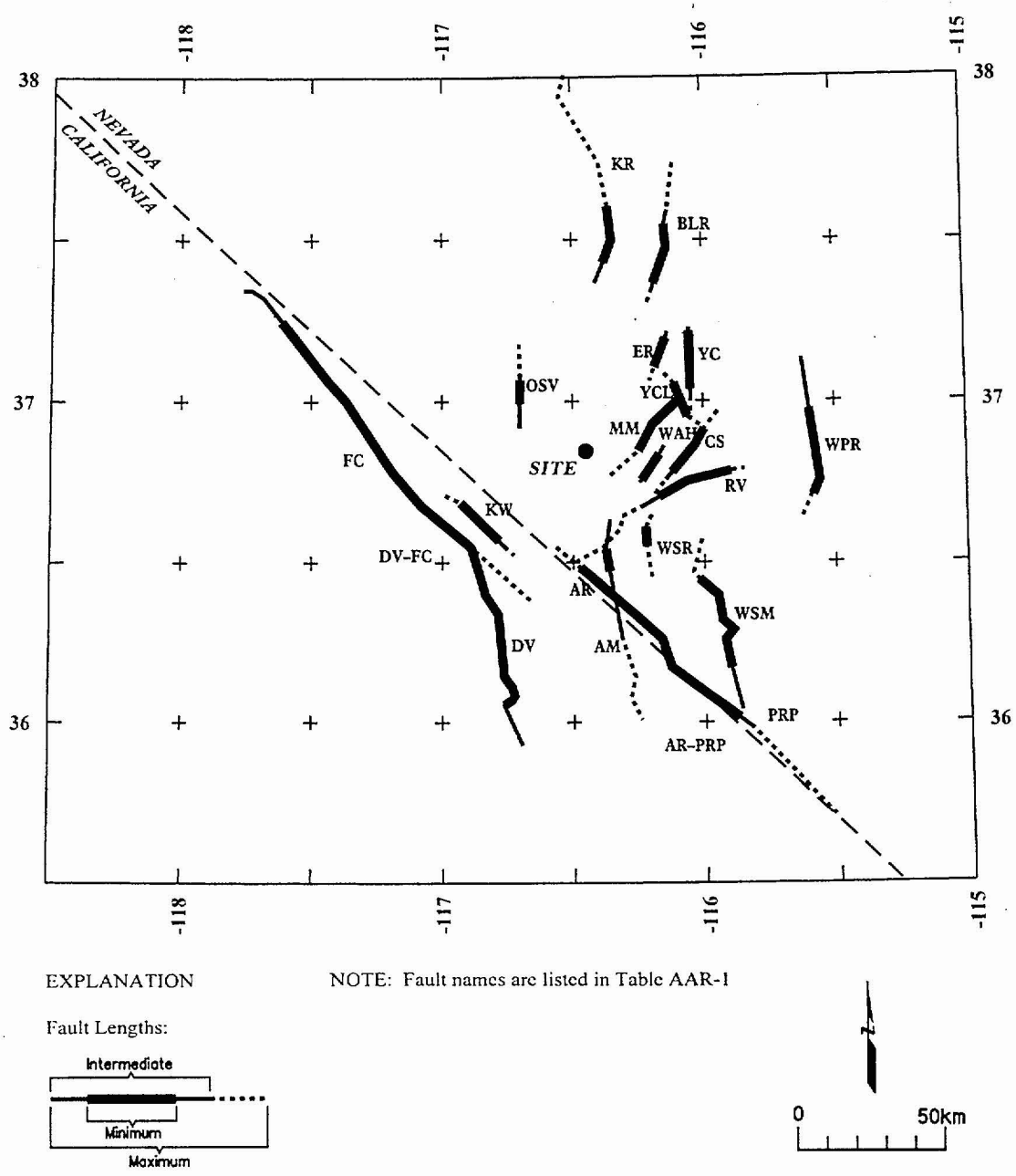

Figure AAR-2 Map showing regional faults included in the seismic source model

h:\prj\yucca_mt\dgn\1097\plate_t4_reg_fault.dgn 27-OCT-1997 15:01

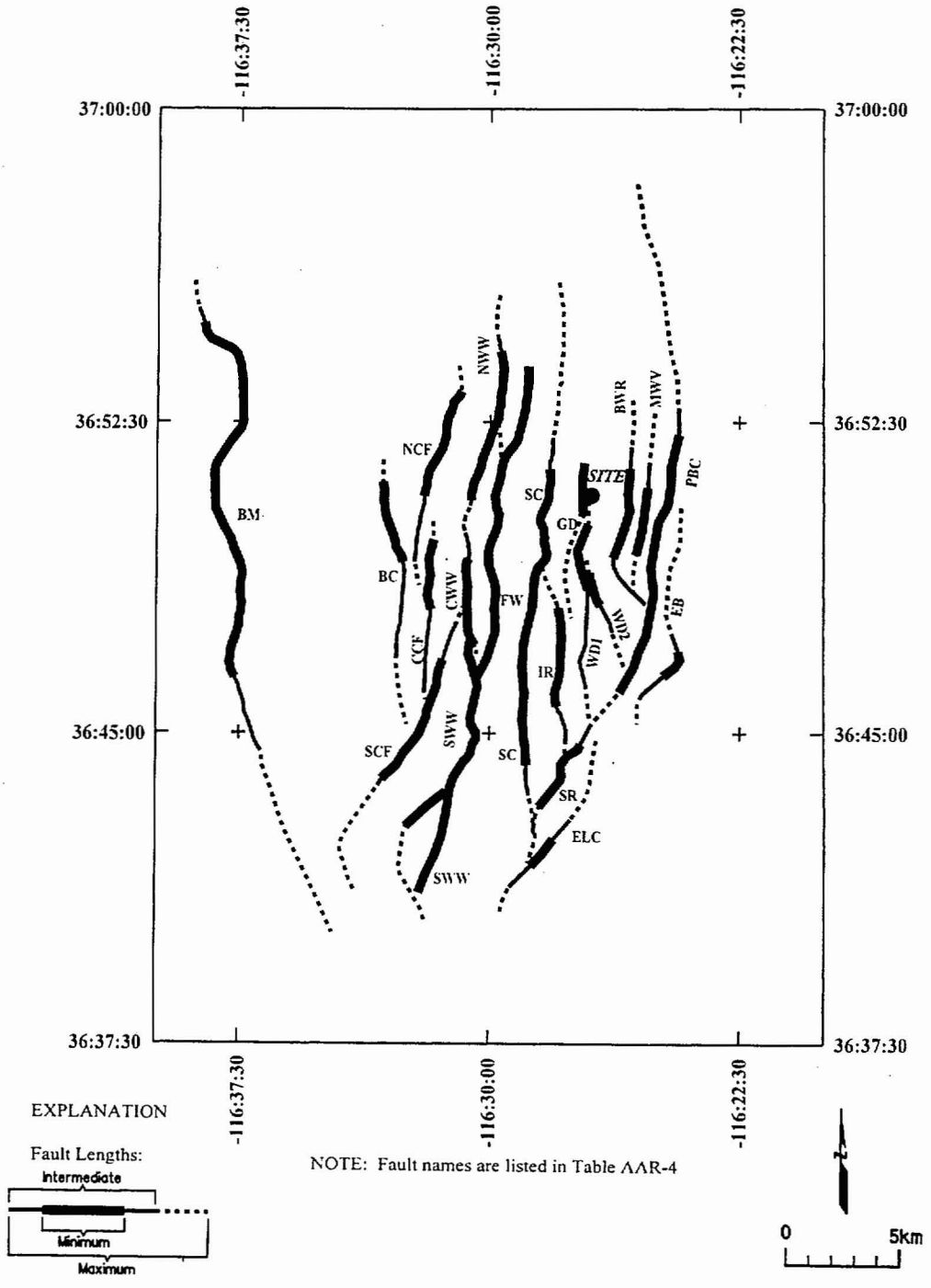

Figure AAR-3 Map showing local fault sources included in the independent model

h:\prj\yucca_mt\dgn\1097\plate_t4_lcl_fault1.dgn 27-OCT-1997 14:59

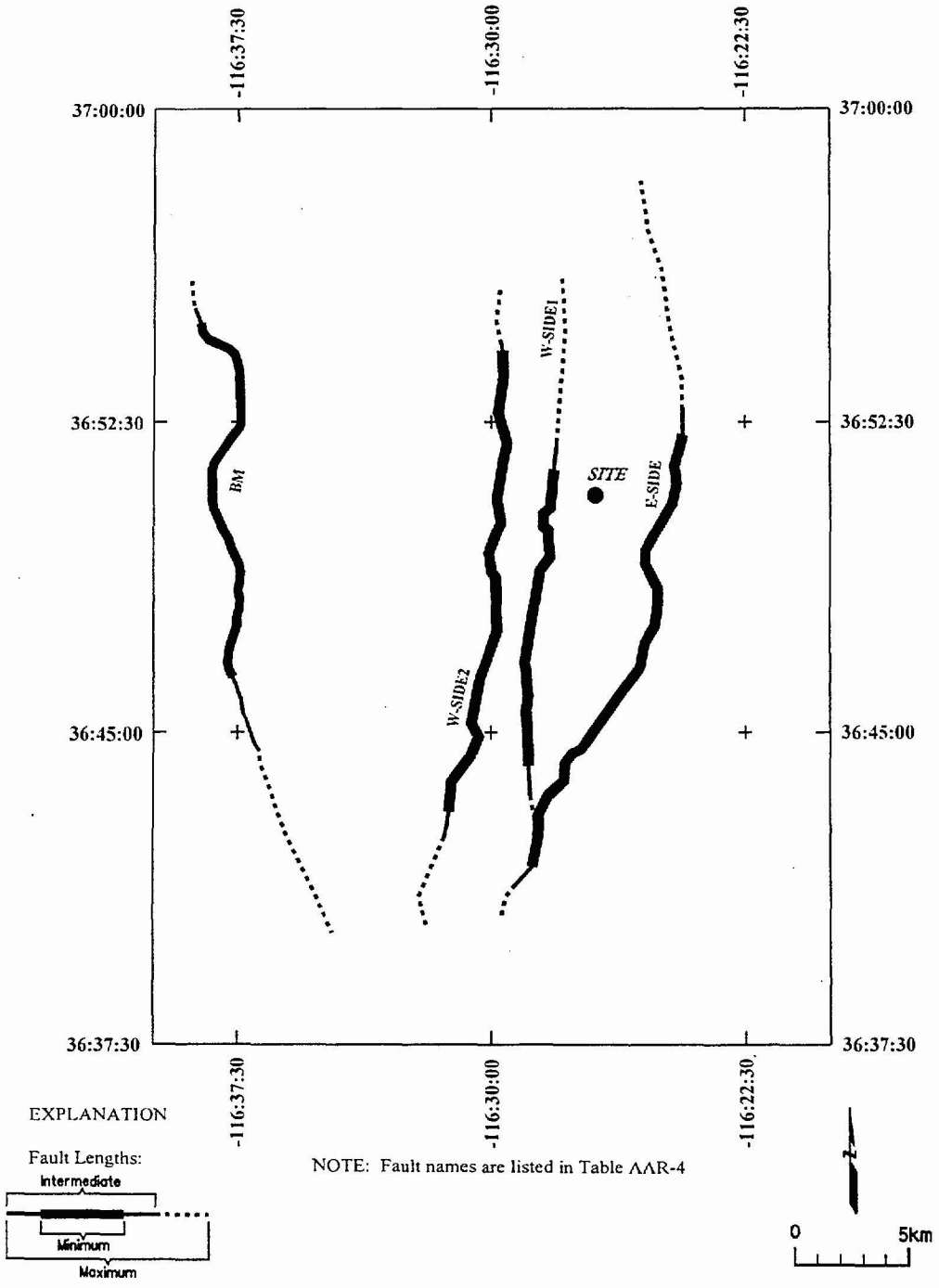

Figure AAR-4 Map showing local faults included in the coalesced model

h:\prj\yucca_mt\dgn\1097\plate_14_lcl_fault2.dgn 27-OCT-1997 15:00

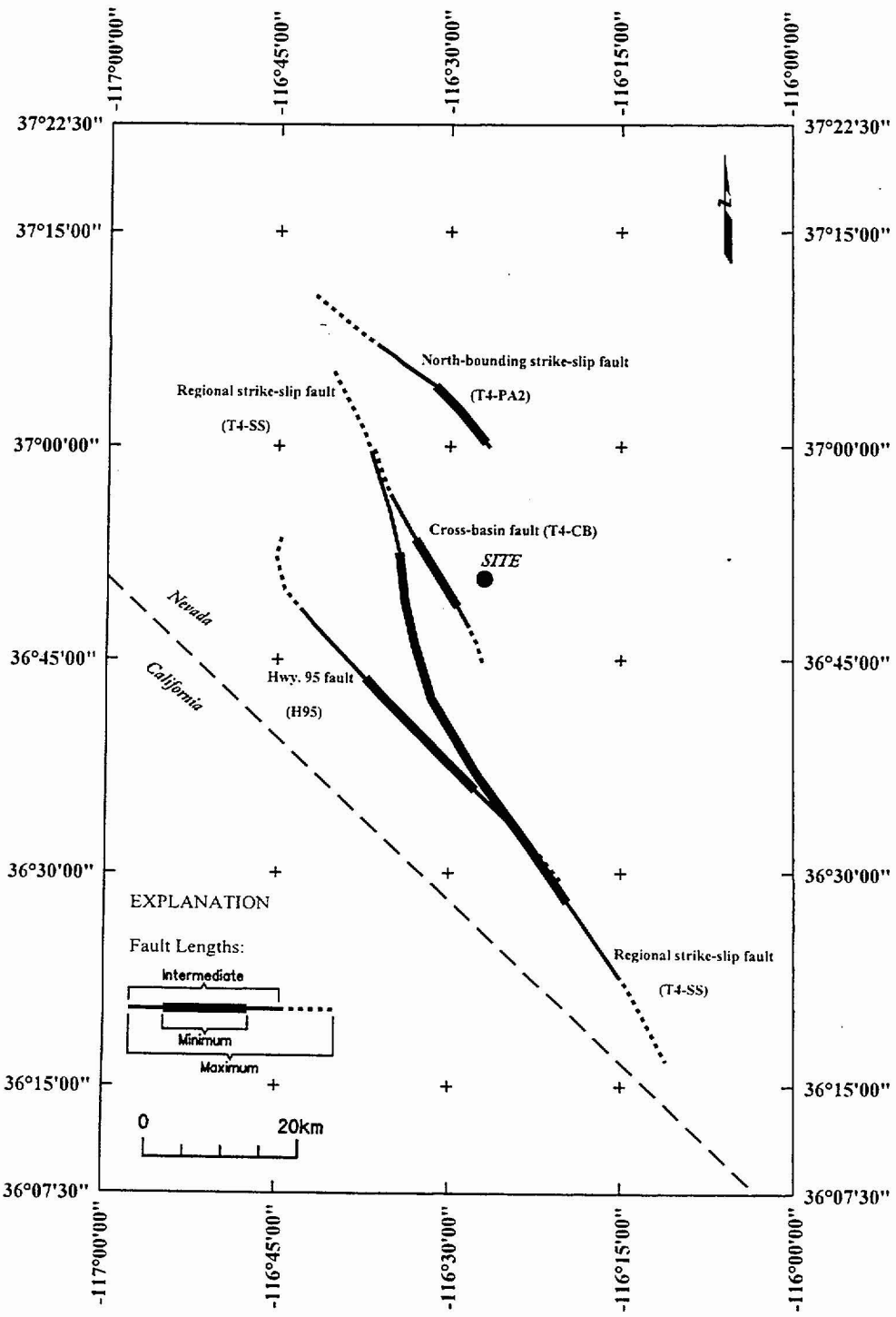

Figure AAR-5 Map showing hypothetical fault sources included in the seismic source model

h:\prj\yucca_mt\dgn\1097\plate_t4_buried_fault.dgn 27-OCT-1997 14:57

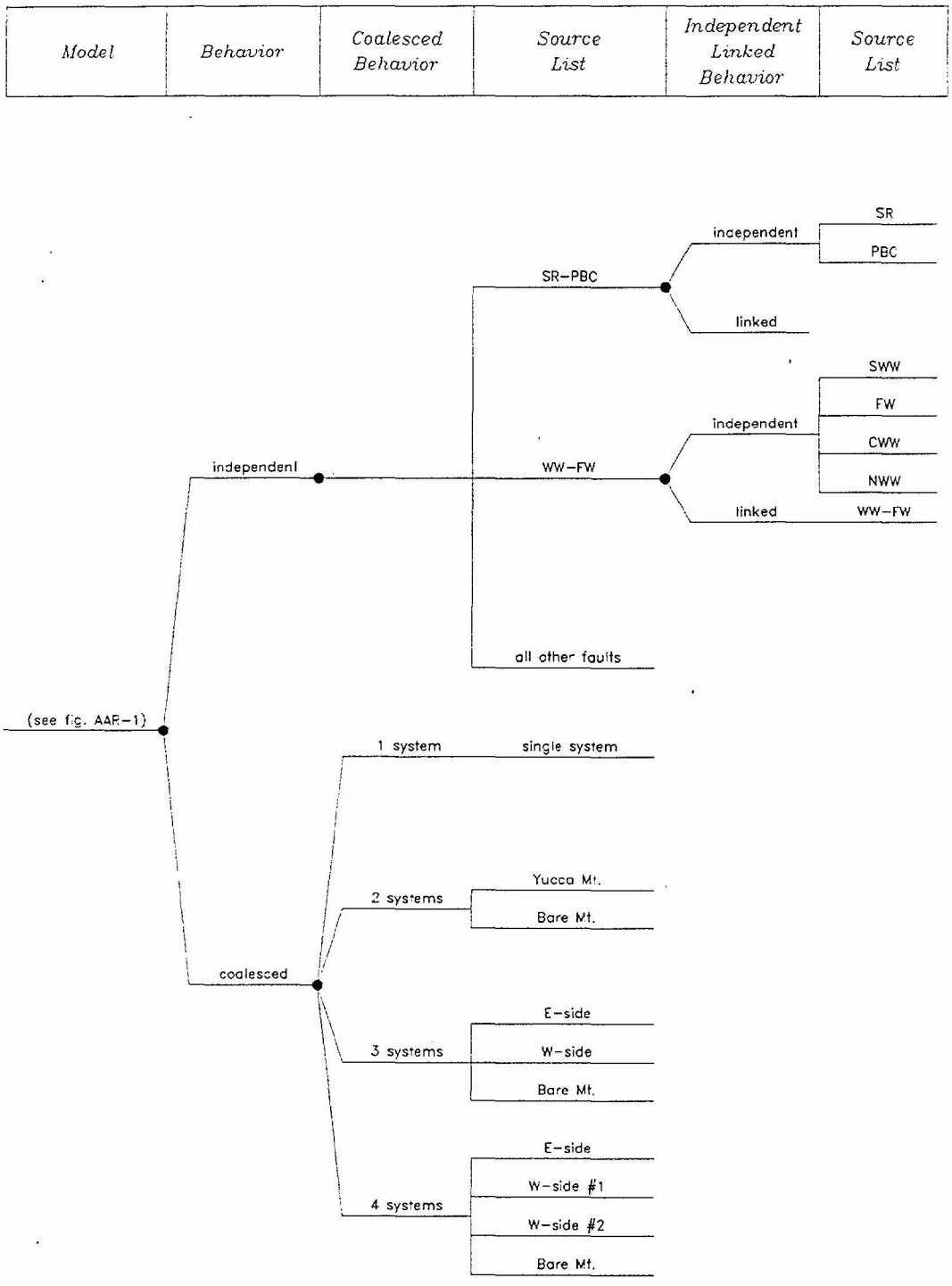

Figure AAR-6 Logic tree: behavior branches for Crater Flat domain

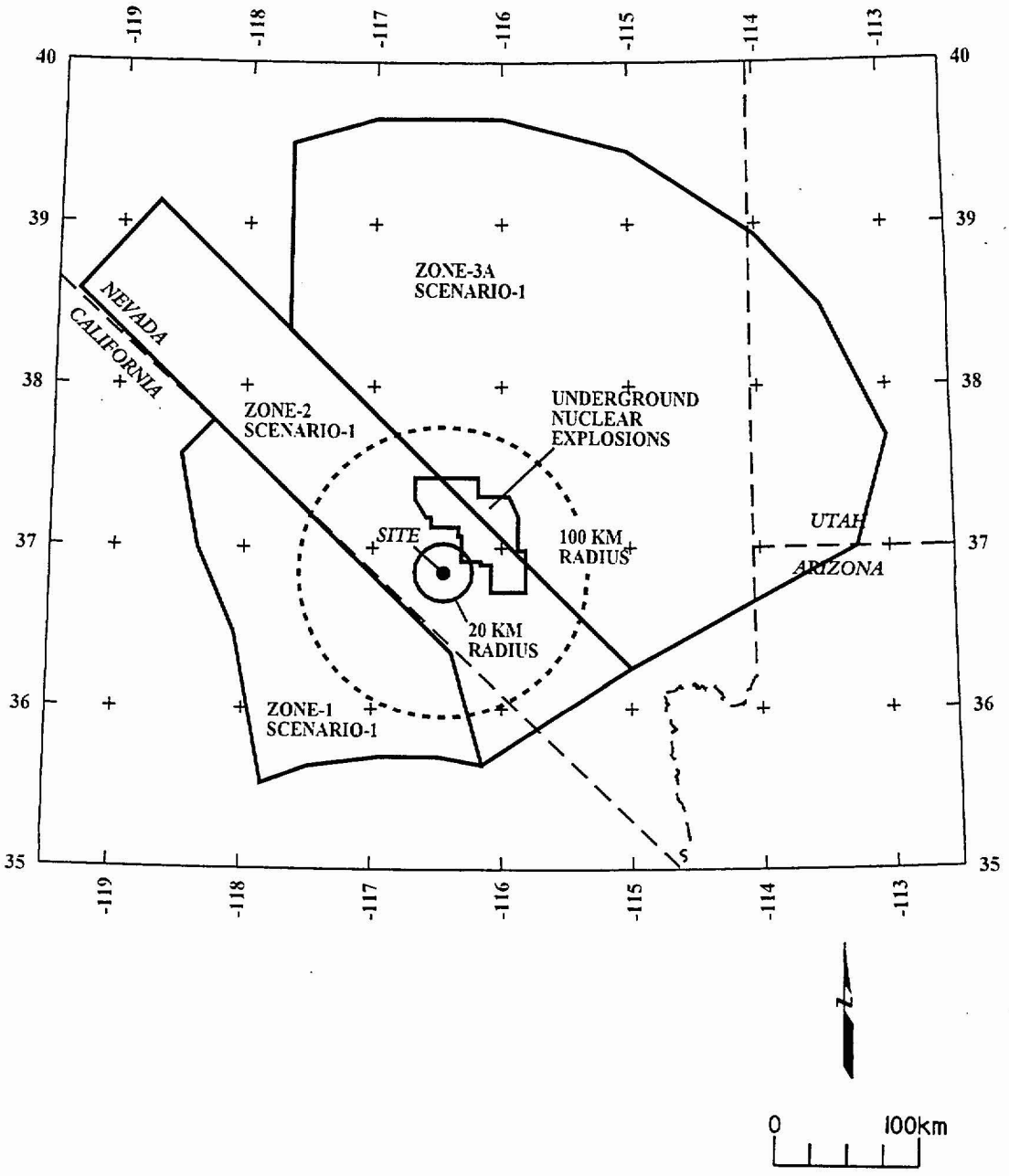

Figure AAR-7 Map showing the boundaries of seismic source zones, Scenario 1.

h:\prj\yucca_mt\dgn\1097\plate_t4_reg_zone1.dgn 27-OCT-1997 15:45

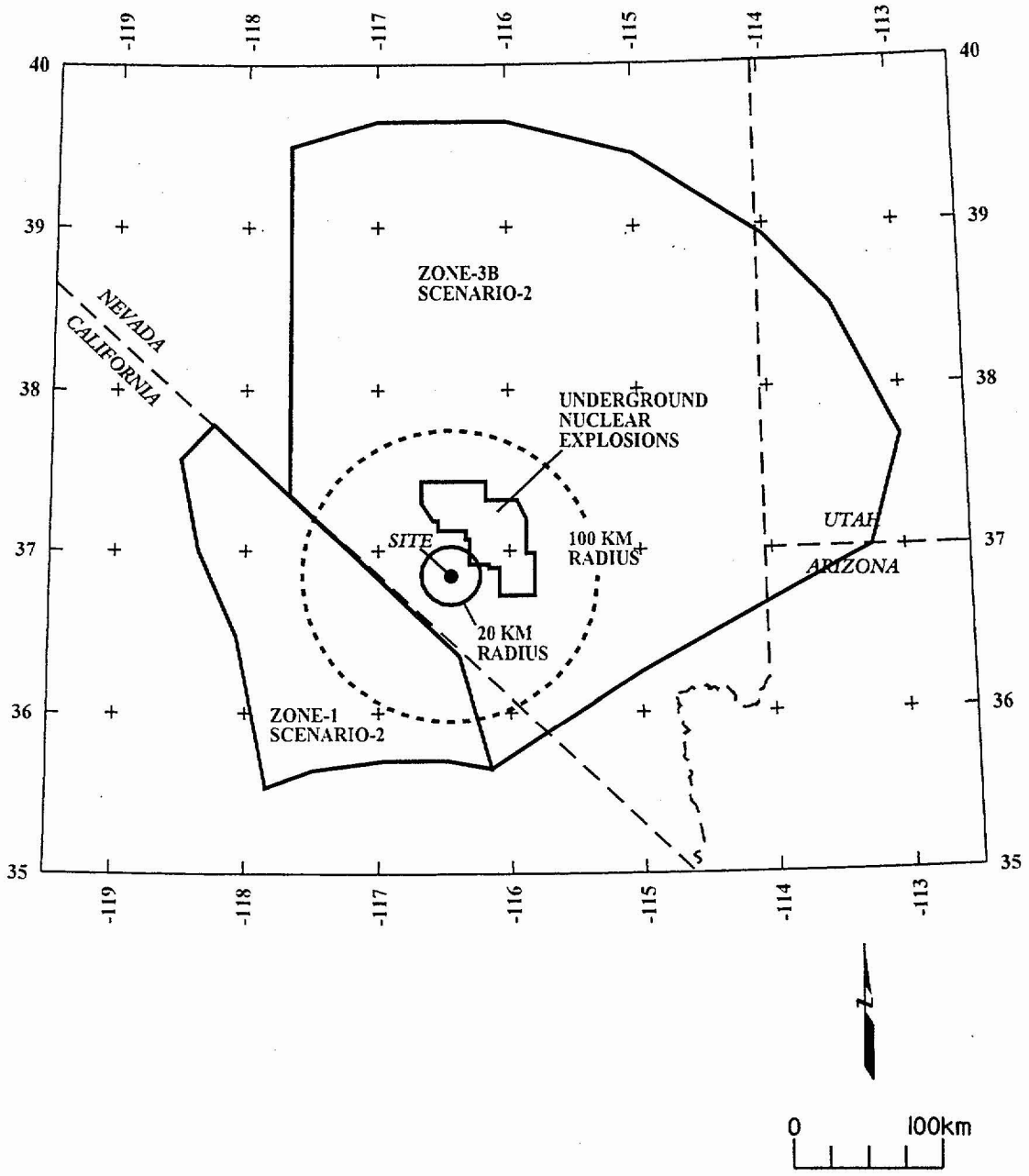

Figure AAR-8 Map showing the boundaries of seismic source zones, Scenario 2.

h:\prj\yucca_mt\dgn\1097\plate_14_reg_zone2.dgn 27-OCT-1997 15:46

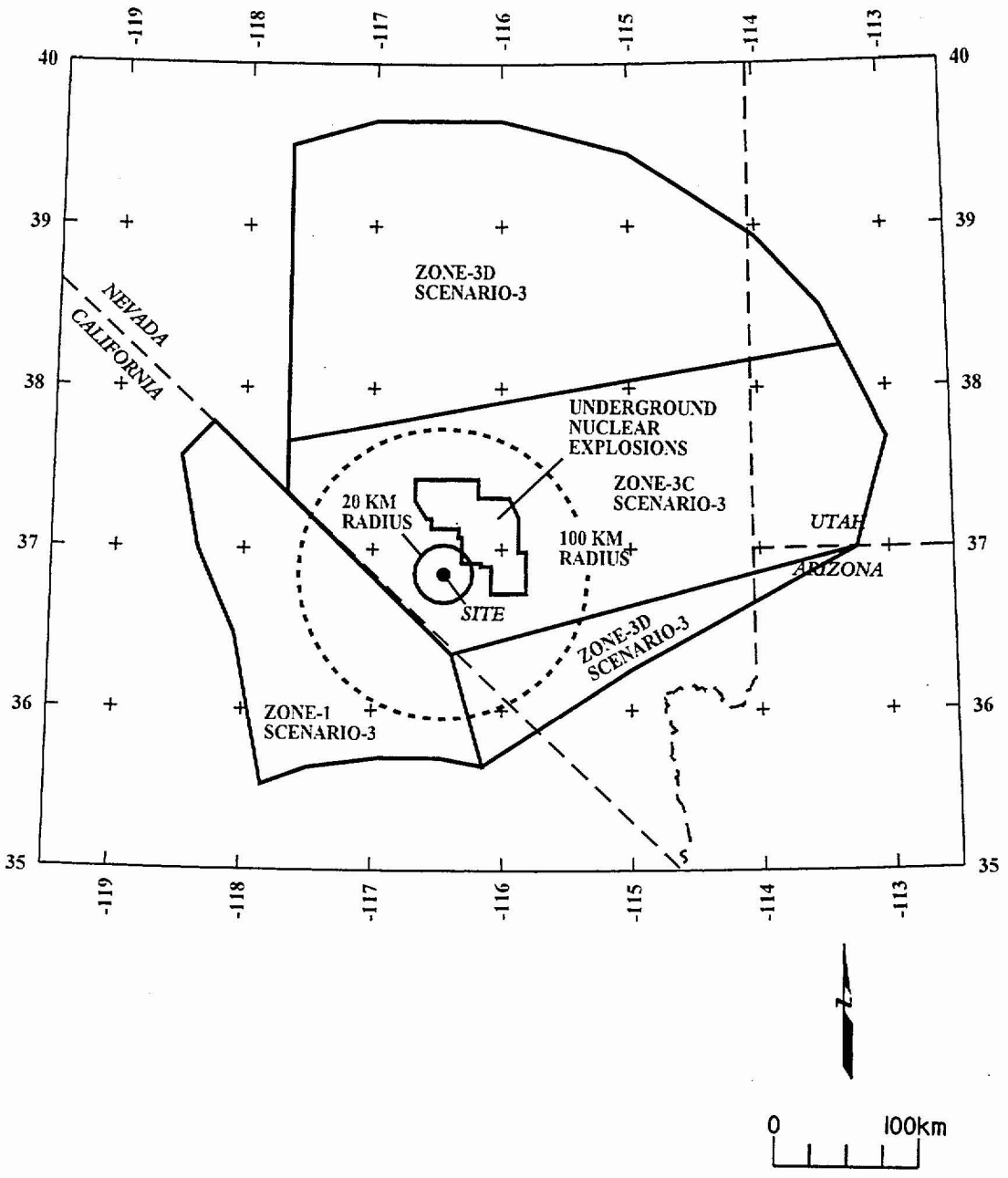

Figure AAR-9 Map showing the boundaries of seismic source zones, Scenario 3.

h:\prj\yucca_mt\dgn\1097\plate_t4_reg_zone3.dgn 27-OCT-1997 15:48

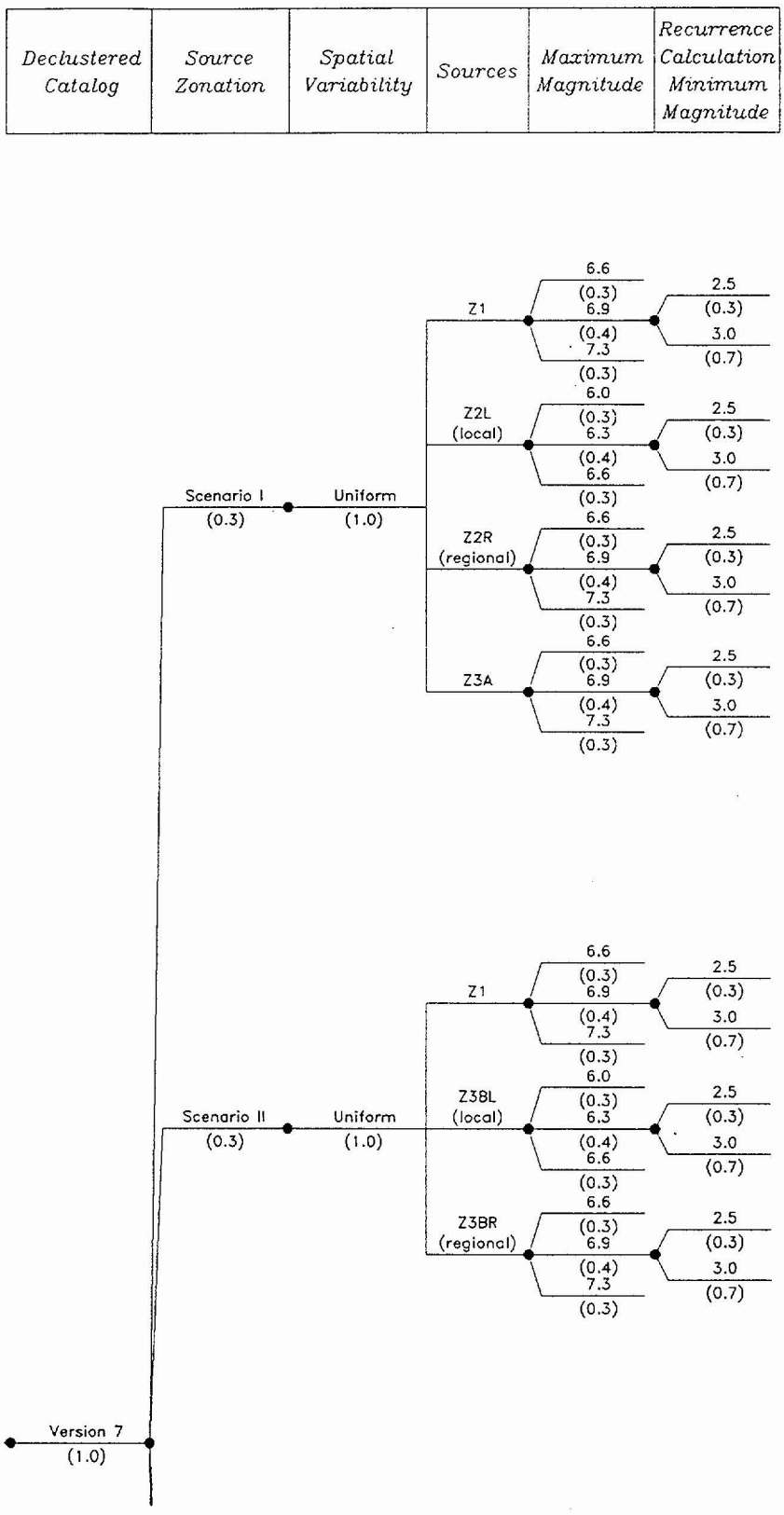

Figure AAR-10a Logic tree for source zones (top)

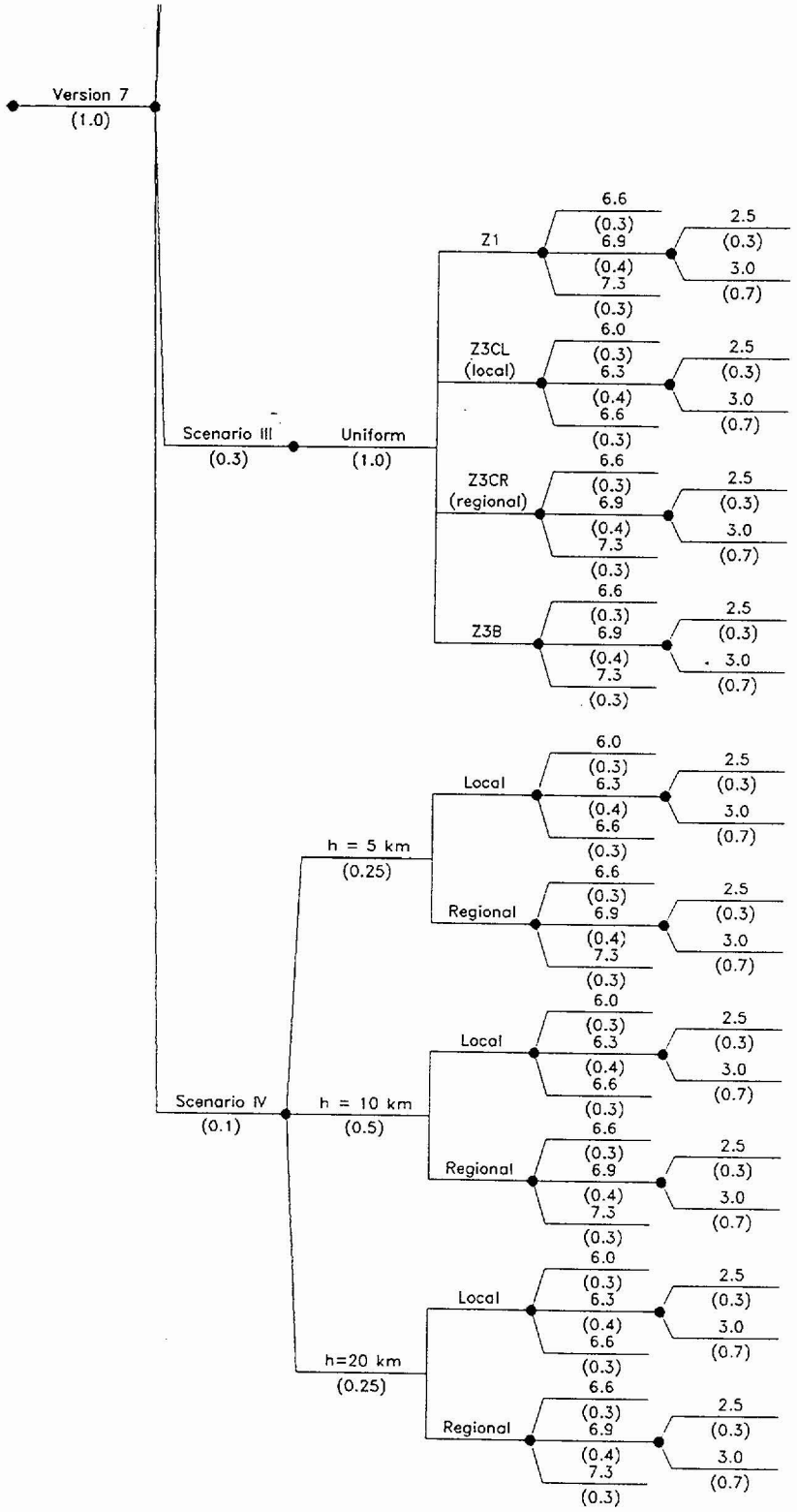

Figure AAR-10b Logic tree for source zones (bottom)

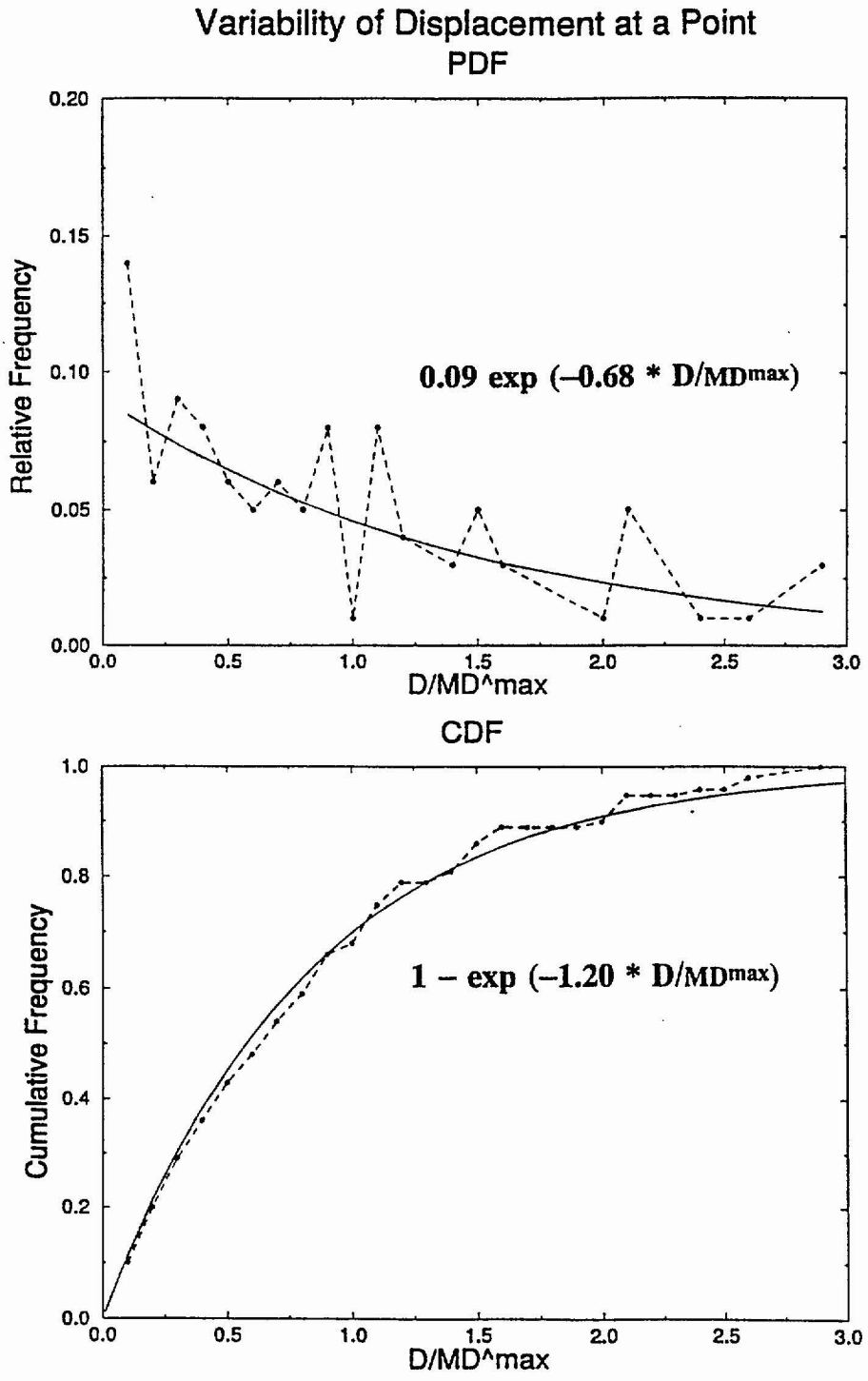

Figure AAR-11 Probability density function (PDF) and cumulative distribution function (CDF) for 80 measurements of single-event displacement, normalized to MD^{max} for the corresponding fault, from 19 trenches in the Yucca Mountain area

INITIAL BRANCHES OF SEPARATE LOGIC TREES
FOR PRINCIPAL AND DISTRIBUTED FAULTING

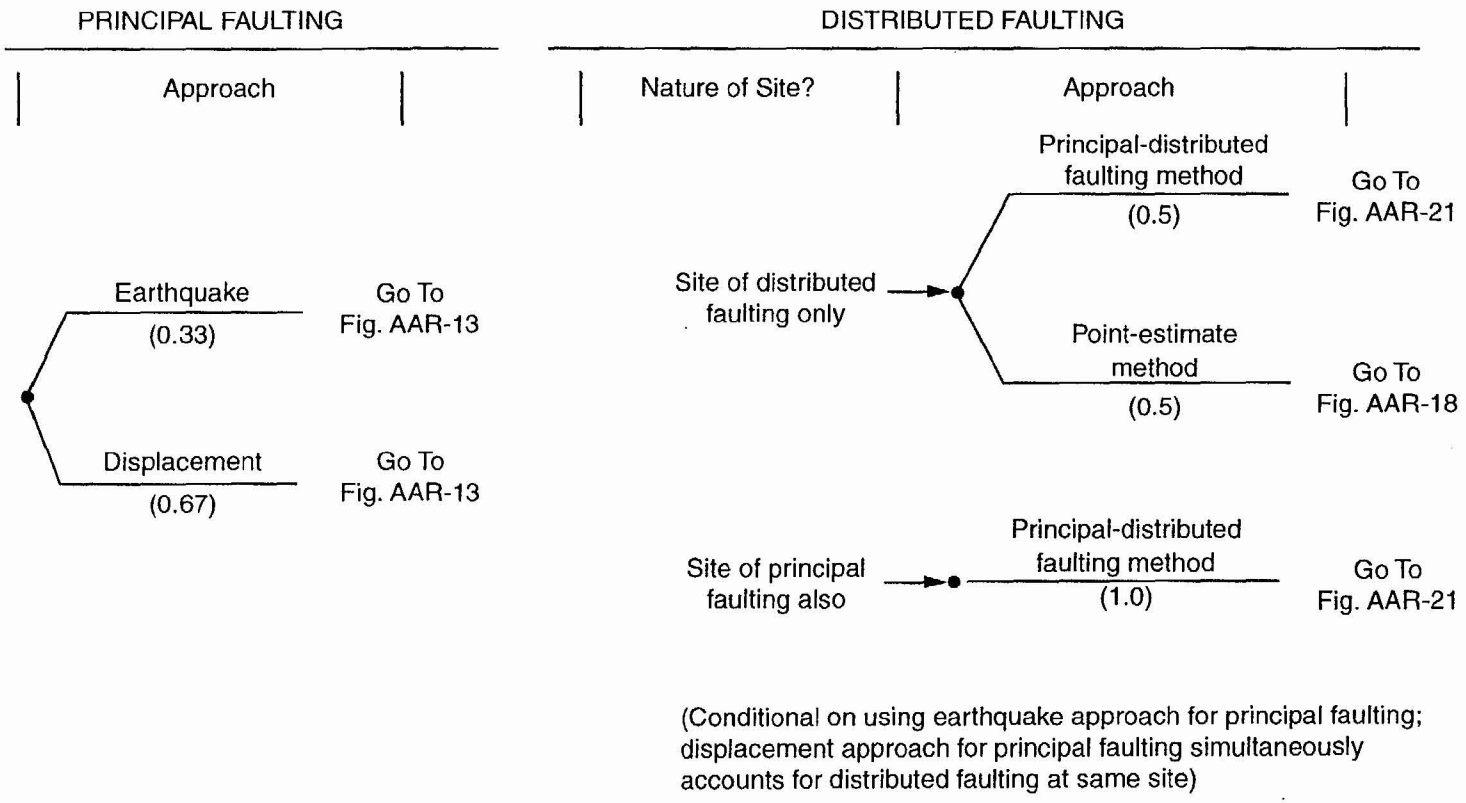

Figure AAR-12 Initial branches of separate logic trees for principal and distributed faulting

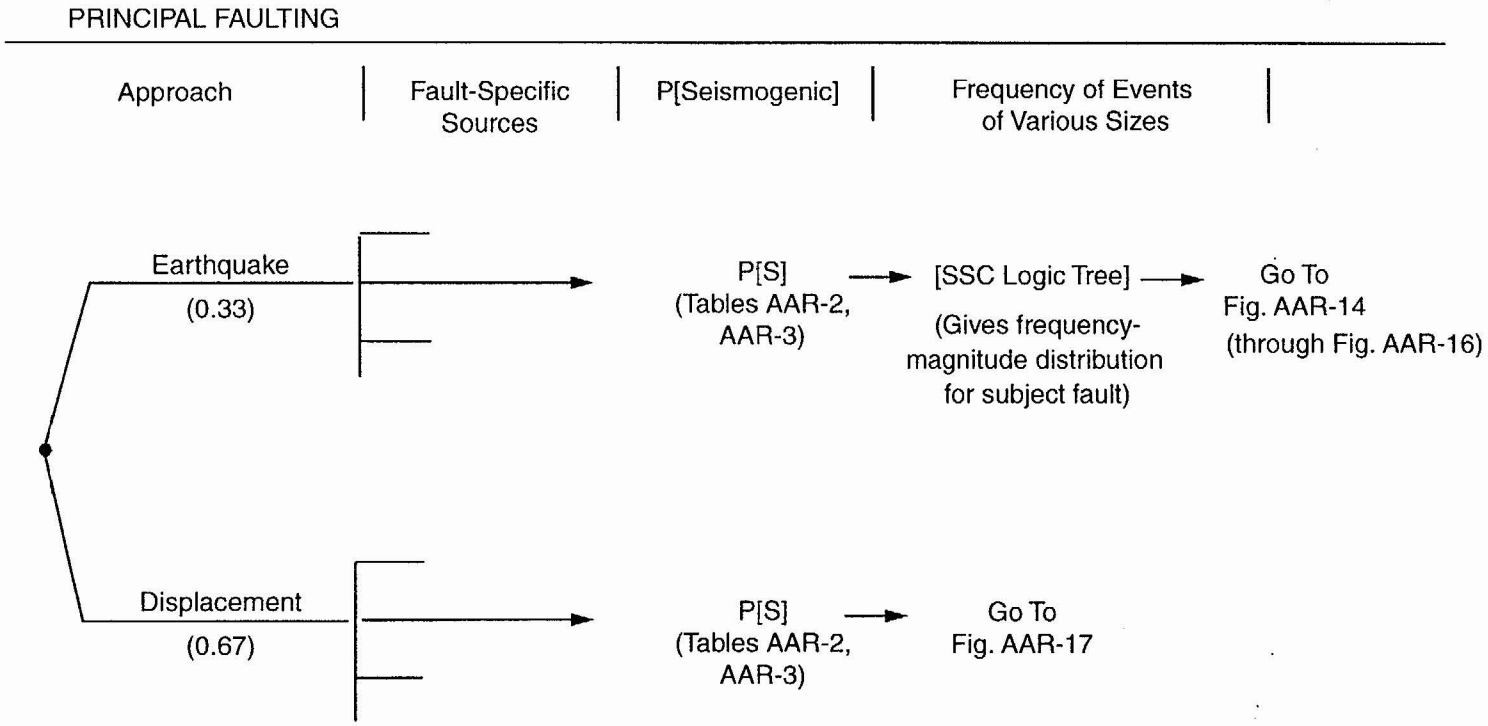

Figure AAR-13 Logic tree for principal faulting

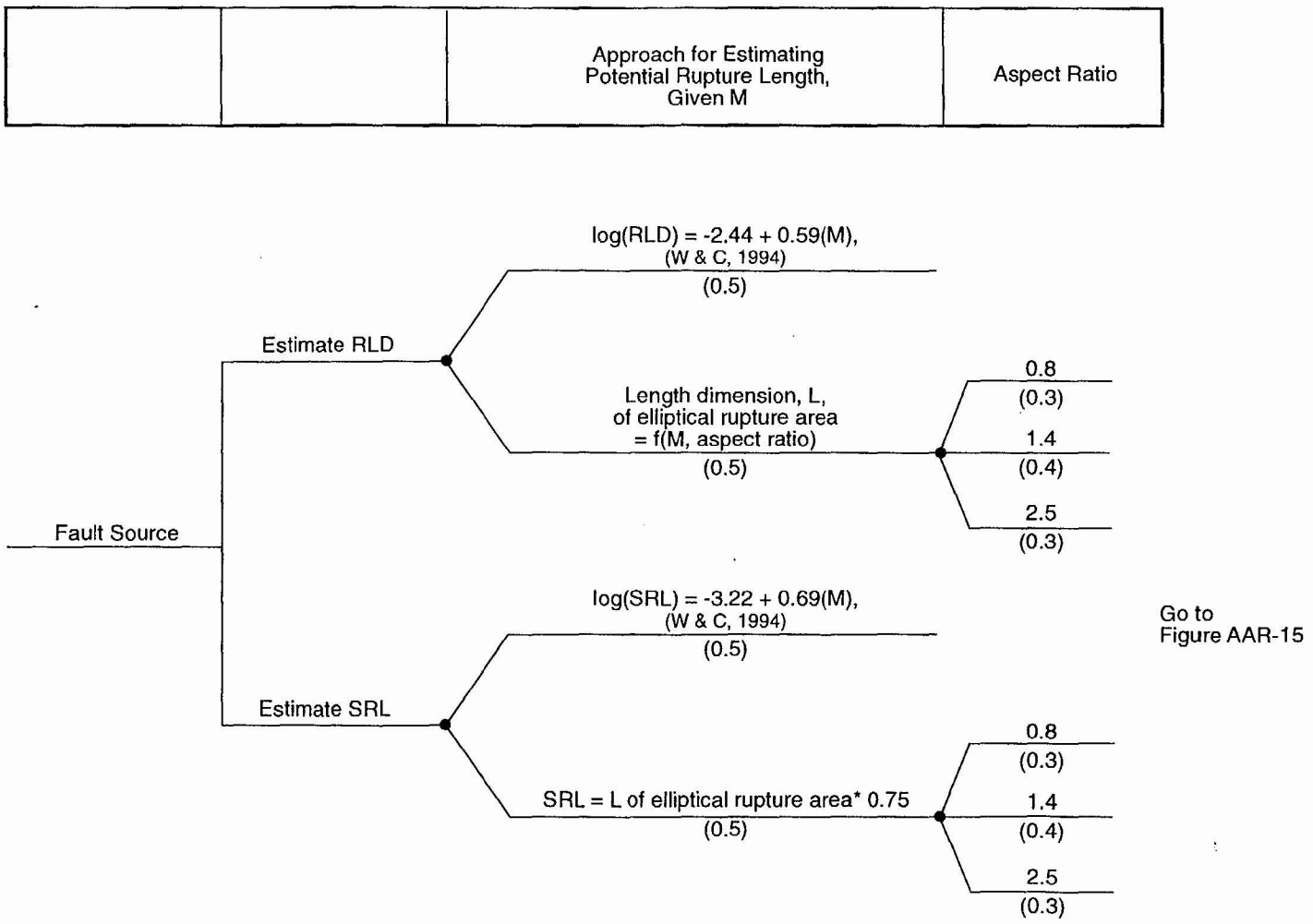

Figure AAR-14 Logic tree for principal faulting – earthquake approach (cont'd): estimating potential rupture length, given M

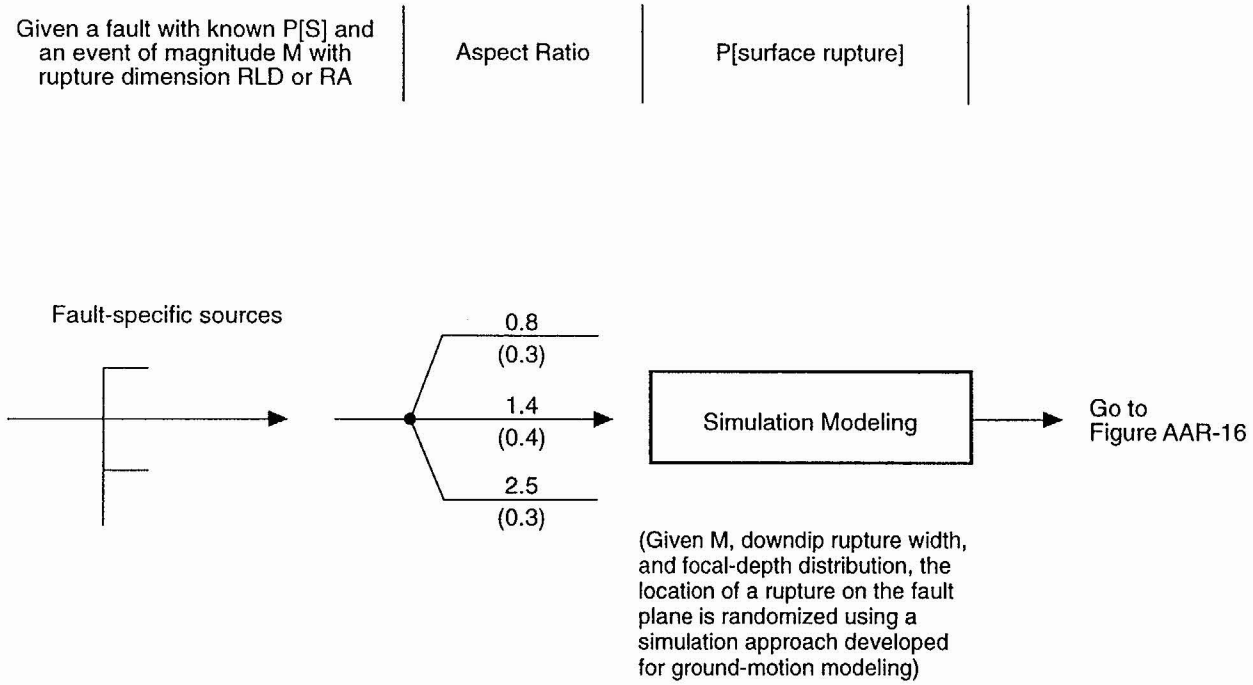

Figure AAR-15 Logic tree for principal faulting – earthquake approach (cont'd)

Given a rupture event on a fault source with known M, P[S], $\overline{RLD}$, $\overline{SRL}$, and P[surface rupture]	*Approach for Estimating Principal Fault Displacement, MD*	*Variability of Slip Along Strike*

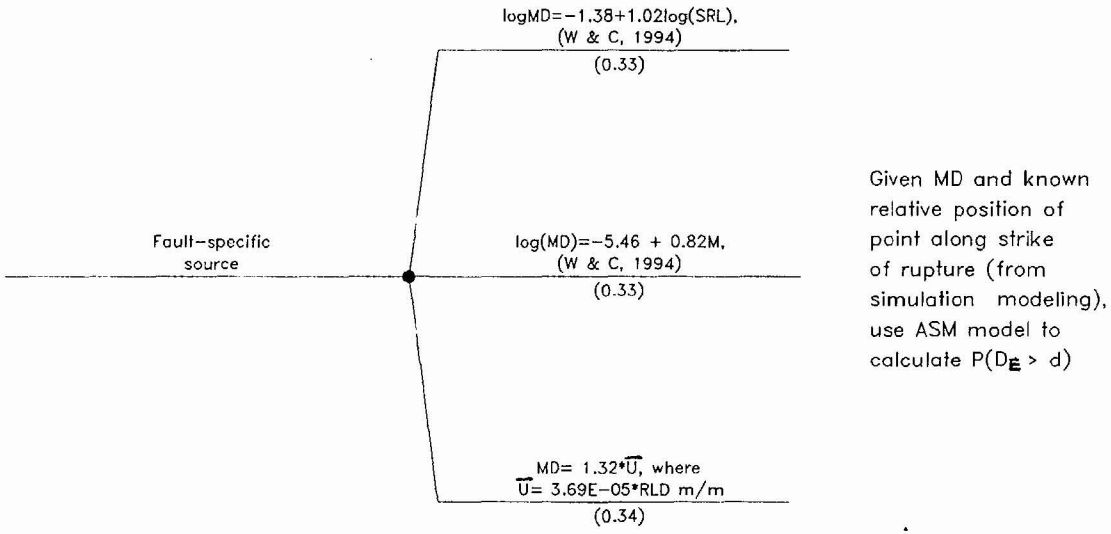

Figure AAR-16 Logic tree for earthquake approach to principal faulting (cont'd): estimating principal fault displacement, *MD*

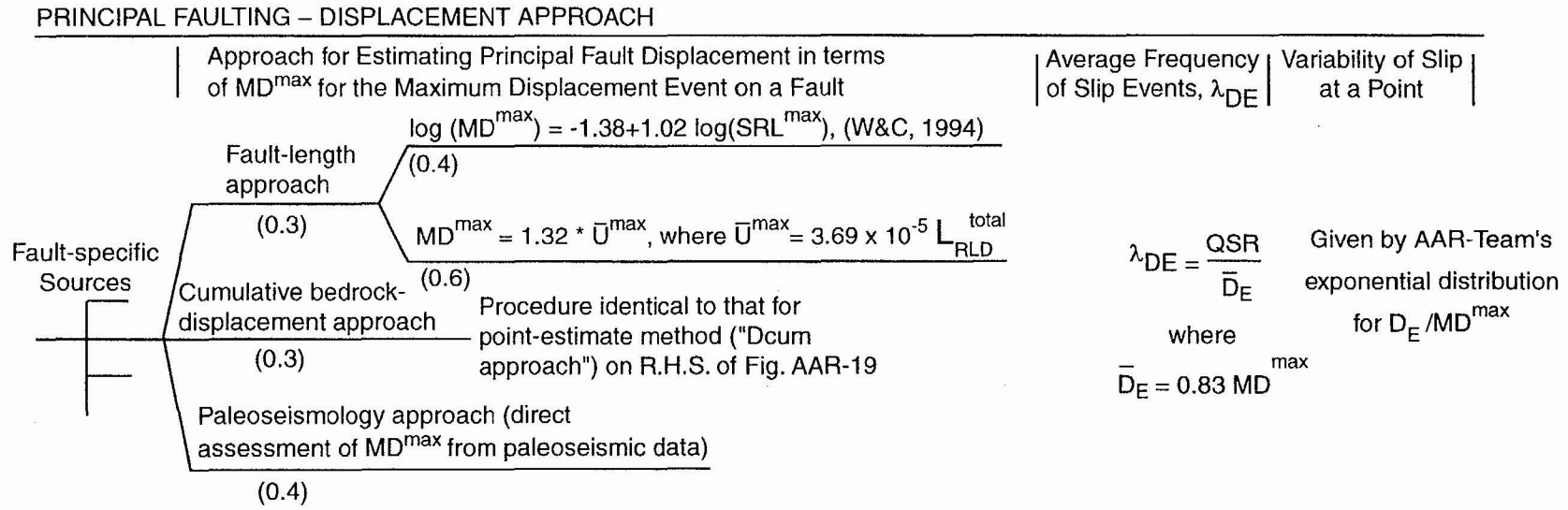

Figure AAR-17 Logic tree for principal faulting — displacement approach

DISTRIBUTED FAULTING — POINT-ESTIMATE METHOD

Secondary Fault or Fracture	P[C] (susceptibility to slip)	Total Post-Tiva Canyon Displacement, Dcum	Approach for Estimating Average Quaternary Slip Rate QSR	Portion of Dcum contributing to QSR

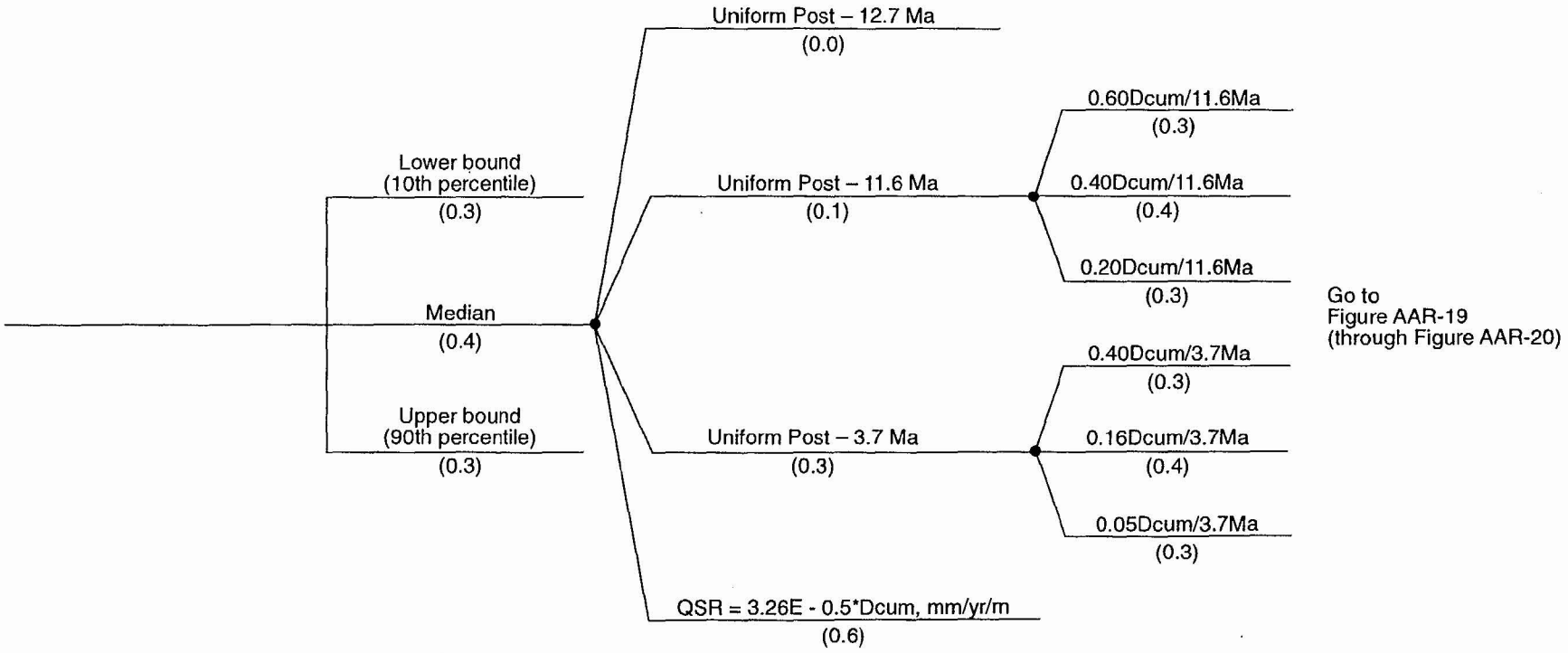

Figure AAR-18 Logic tree for distributed faulting – point estimate method

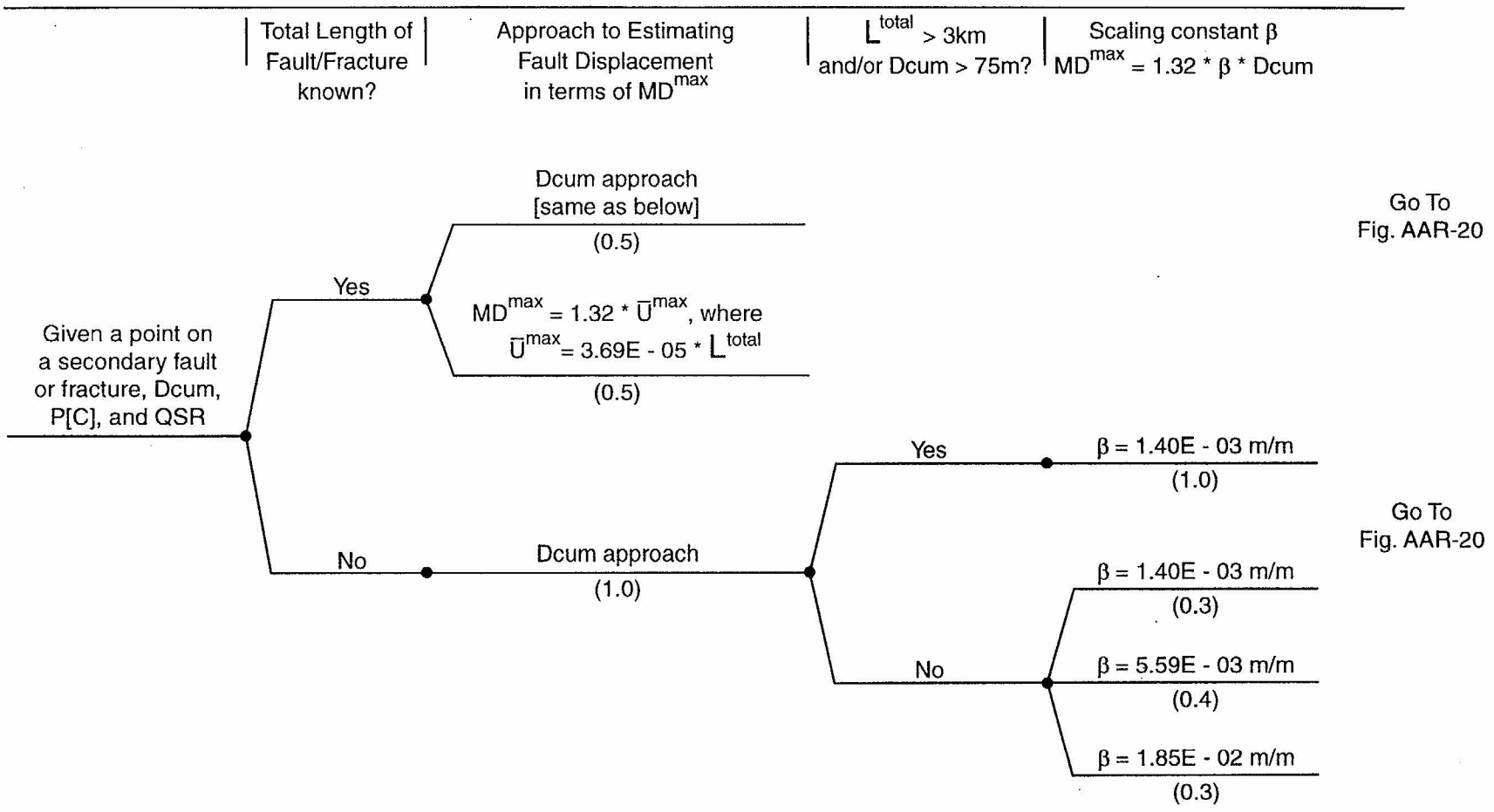

Figure AAR-19 Logic tree for distributed faulting — point-estimate method, cont'd

Average Frequency of Slip Events, λ_{DE}	Variability of Slip at a Point
Given a point on a secondary fault or fracture, Dcum, P[C], QSR, and MD^{max} → $\lambda_{DE} = \frac{QSR}{\bar{D}_E}$ where $\bar{D}_E = 0.83\ MD^{max}$	Given by AAR-Team's exponential distribution for D_E / MD^{max}

Figure AAR-20 Logic tree for distributed faulting — point-estimate method, cont'd

DISTRIBUTED FAULTING – PRINCIPAL-DISTRIBUTED FAULTING METHOD

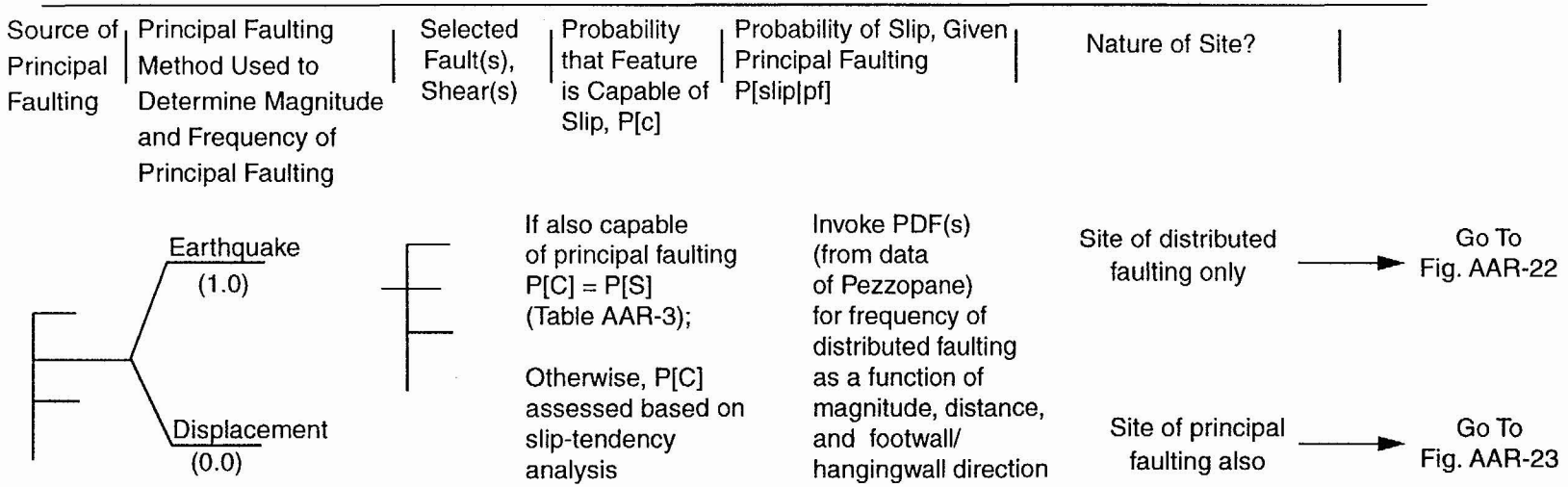

Figure AAR-21 Logic tree for distributed faulting — principal-distributed faulting method

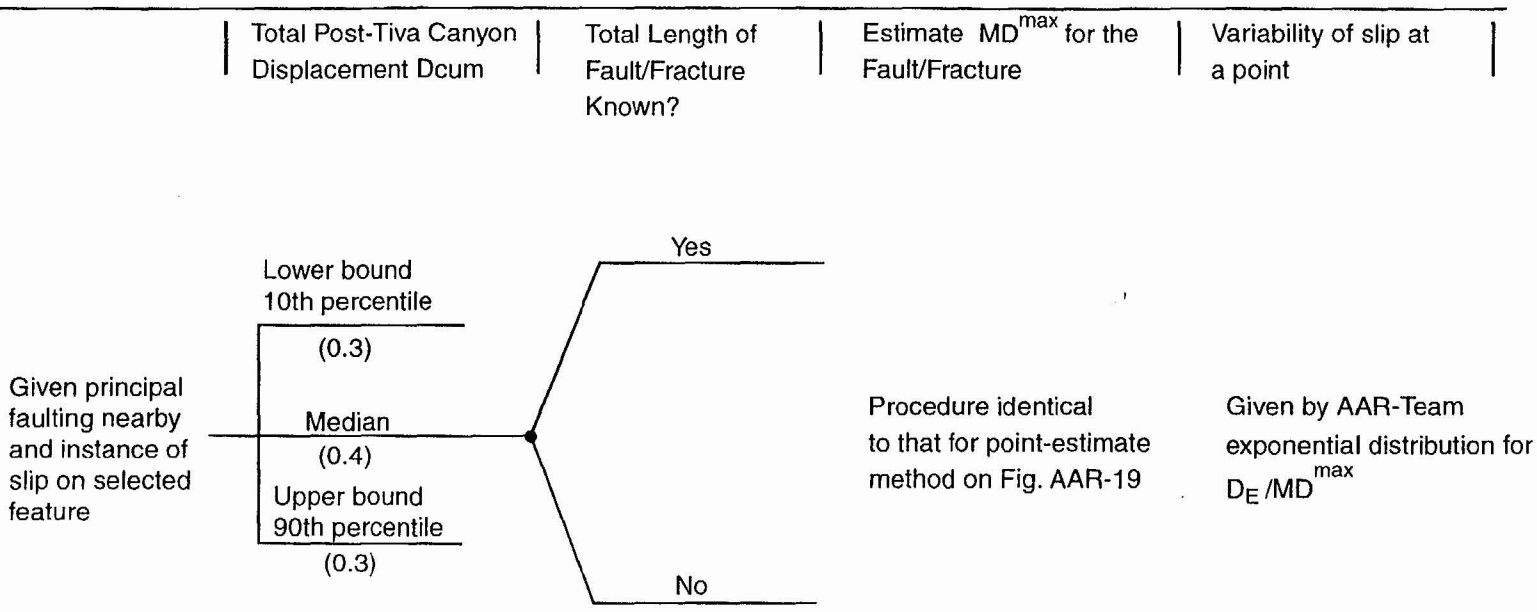

Figure AAR-22 Logic tree for distributed faulting — principal-distributed faulting method, cont'd (for site of distributed faulting only)

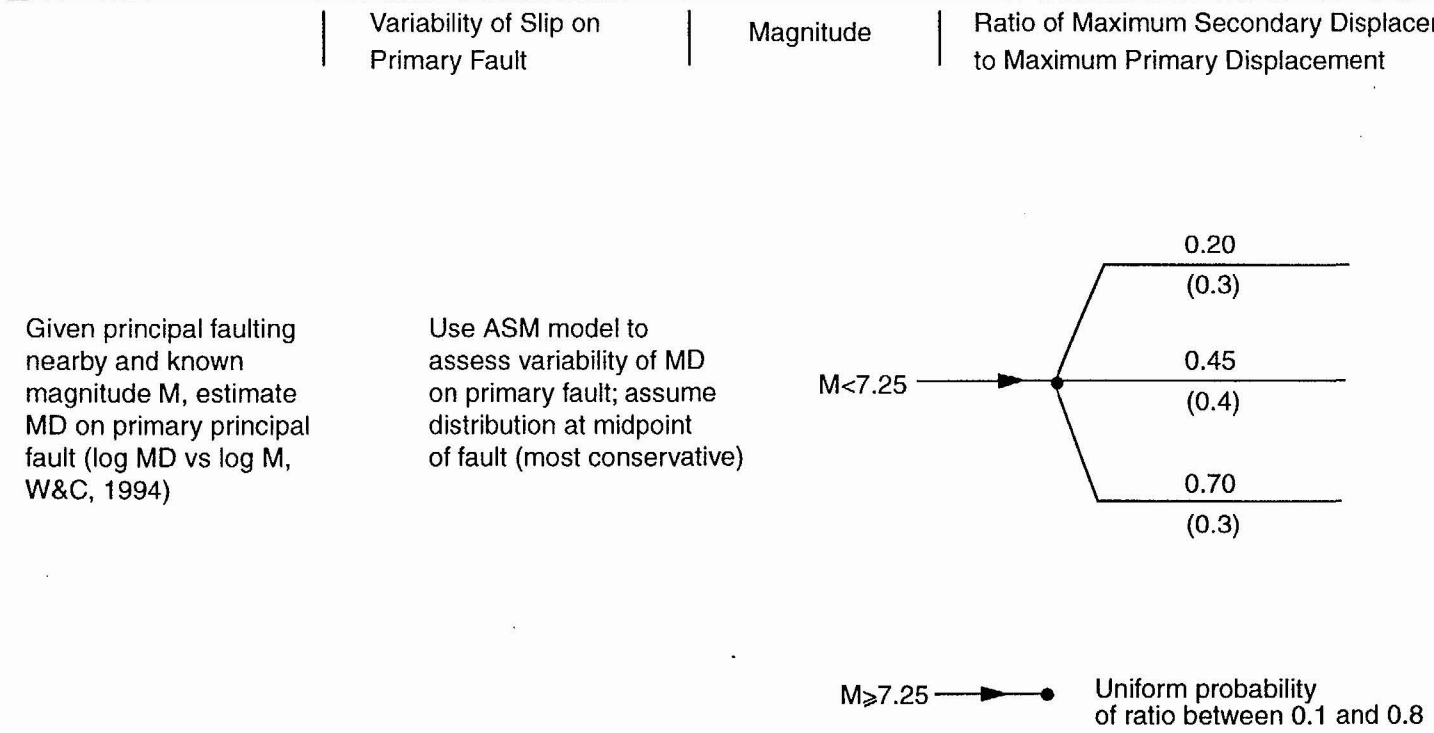

Figure AAR-23 Logic tree for distributed faulting — principal-distributed faulting method cont'd (for site of principal faulting also)

ELICITATION SUMMARY

DIANE DOSER, C.J. FRIDRICH, AND FRANK H. SWAN

TABLE OF CONTENTS

TABLE OF CONTENTS

TABLE OF CONTENTS

TABLES

TABLE OF CONTENTS

FIGURES

TABLE OF CONTENTS

ELICITATION SUMMARY
DIANE DOSER, C. J. FRIDRICH, AND FRANK H. SWAN

1.0
INTRODUCTION

Available seismic, geologic, and geophysical data are used to characterize potential earthquake hazards at Yucca Mountain. The approaches and source parameters presented here will be used by the Yucca Mountain project to develop probability functions that relate: (1) values of strong ground shaking (peak acceleration or spectral acceleration) to annual probability of exceedance; and (2) the likelihood of fault displacement at selected sites in the vicinity of the proposed underground repository.

The geologic and tectonic setting of the Yucca Mountain region and the seismicity data used in this analysis are described in Sections 2 and 3, respectively. The characterization of seismic sources for the ground motion analysis is presented in Section 4. The methods for assessing the potential for fault displacement and the characterization of tectonic features at selected localities within the controlled area at Yucca Mountain are presented in Section 5.

2.0
GEOLOGIC AND TECTONIC SETTING

Yucca Mountain is located in southwest Nevada in the eastern part of the Walker Lane belt, a 100- to 300-km-wide by 700-km-long zone of irregular topography and discontinuous strike-slip structures between the Sierra Nevada and the northern Basin and Range province (Stewart, 1988) (Figure DFS-1). Together, the northern Basin and Range and the Walker Lane belt make up the Great Basin, a region of dominantly extensional tectonism that began with back-arc spreading, at about 45 Ma, associated with subduction of the Farallon plate under the North American plate (Scholz *et al.*., 1971). During northward migration of the Mendocino triple junction, subduction along the southwest coast of North America ceased as the North American plate became juxtaposed against the Pacific plate along a strike-slip boundary, the San Andreas fault (Atwater, 1989; Oldow *et al.*., 1989). West of Yucca Mountain, this transition occurred at about 10 Ma. Since this transition, extension in the

Great Basin has been driven by the northwestward movement of the Pacific plate relative to the North American plate.

Within this framework, Yucca Mountain is a multiple-fault-block ridge in the eastern part of the Crater Flat basin, an extensional basin that formed primarily between 12.7 and 10 Ma, before the tectonic transition discussed above. The Crater Flat basin is a subbasin of the Amargosa trough, a long graben-like feature bounded on the west by the Bare Mountain range-front fault and on the east by the largely buried gravity fault (Figure DFS-2). The domain west of the Bare Mountain fault is characterized by extreme extension and by detachment faulting that terminates eastward in the vicinity of the Bare Mountain fault. The areas east of Bare Mountain fault, including the Amargosa trough, are characterized by minor to moderate extension. The domains east of the Amargosa trough are dominated by northeast-striking, left-lateral strike-slip faults and northwest-striking, right-lateral strike-slip faults. (Only the major ones are shown on Figure DFS-2.)

The Crater Flat basin lies on the south flank of the Timber Mountain caldera complex, the central eruptive source area of the southwest Nevada volcanic field. This volcanic field straddles the structural transition between the Walker Lane belt and the northern Basin and Range Province. The caldera complex has influenced the development of structures within the northernmost part of the Crater Flat basin by local modification of the stress regime associated with doming of the area around the calderas (Fridrich, 1997).

Yucca Mountain is composed of a 1.5- to 3.0-km-thick sequence of variably welded Miocene ash-flow tuffs and lesser ashfall tuffs and lavas of the southwest Nevada volcanic field overlying a complexly deformed Paleozoic and late Precambrian sequence of marine carbonates, quartzites, and argillites. The Tertiary section thickens westward within the Crater Flat basin to a maximum thickness of about 4 km, and is truncated on the western margin of the basin by the Bare Mountain fault. The Tertiary strata in the basin are tilted dominantly eastward to southeastward along a closely spaced system of mostly west- to northwest-dipping faults. Most of the intrabasin faults are thus antithetical to the range-front fault at the western margin of the basin in that they face into the range-front fault and formed coevally with it (Fridrich,1997).

Deformation in the Crater Flat basin is dominantly extensional but includes a significant component of northwest-directed right-lateral strike-slip strain. On the surface at least, the strike-slip deformation is diffuse rather than discrete—the basin evidently opened in an oblique manner, with the least extension (about 7-15 percent) and the least vertical-axis rotation (less than 5 degrees) in the northeast corner of the basin, on northern Yucca Mountain. From there, the magnitude of deformation increases to the west and south, to maximum values of 50 to 100 percent extension and at least 45 degrees clockwise rotation in the southwest corner of the basin (Fridrich *et al.*., in press). The vertical-axis rotation in the basin is accommodated by left slip on the closely spaced north- to northeast-striking normal faults that comprise the internal structure of the basin. The structural geometry of the Crater Flat basin thus resembles that of some strike-slip pull-apart basins; however, detailed mapping has failed to uncover any evidence of master strike-slip faults anywhere in, or at the margins of, this basin. As in most of the eastern Walker Lane belt, the strike-slip deformation is diffuse rather than discrete.

In the Yucca Mountain region, the 10 Ma transition in the driving force of tectonism, discussed above, coincided with a shift in the style of volcanism to much lower eruptive volumes, and a shift from dominantly silicic volcanism before 10 Ma to dominantly basaltic volcanism afterward. A significant shift in tectonic style also may have occurred during this transition; however, because of the large decrease in silicic volcanism around 10 Ma, there is poor stratigraphic constraint on the tectonic evolution of this region between 10 Ma and present.

The evidence indicates that, after 10 Ma, the locus of both volcanism and tectonism continued to migrate westward out of the Yucca Mountain vicinity toward Death Valley, as it had been doing since 12.7 Ma. In the wake of this westward migration of the focus of tectonism, tectonism rates in the Yucca Mountain region declined strongly after 10 Ma. Quaternary tectonism in the Yucca Mountain region has consisted of selective reactivation of certain faults that formed during the middle Miocene or earlier, including some of the major faults in Crater Flat basin, as well as faults in the Rock Valley fault system to the east (Figure DFS-2).

During the Quaternary, tectonism and volcanism in the Great Basin has been localized primarily along the eastern limit of the extensional province—at the Wasatch Front, and along the western limit of the province—in Death and Owen's valleys. In addition, a third and significantly lesser area of tectonism has been a north-trending zone in the center of the province. Yucca Mountain is located outside all three of these zones of major Quaternary seismic activity, and the rates of recent tectonism at Yucca Mountain are much lower than in any other part of the Great Basin where studies of Quaternary tectonism have been conducted.

In the Crater Flat basin, eight major faults show evidence of offset during the past 500,000 years, with rates of slip ranging from less than 0.001 to about 0.03 mm/yr. All of these faults formed around 12.7 Ma, and the current level of activity along these faults is very low relative to slip rates on the same structures between 12.7 and 10 Ma (Fridrich *et al.*., in press). The three largest Quaternary faults on Yucca Mountain show late Quaternary slip rates that increase southward, indicating that the oblique style of extension in the Crater Flat basin, established during the middle to late Miocene, has continued to the present.

Basalts have erupted in Crater Flat basin in four episodes, at about 10 Ma, 3.7 Ma, 1 Ma, and 70 ka, that together define a trend of progressively declining volume of magma (B.M. Crowe *et al.*, LANL, written communication, 1995). The latest eruption formed the Lathrop Wells center, a small cinder cone with associated lavas on the southern end of Yucca Mountain. The fact that ash from this eruptive center fills cracks formed during late Quaternary faulting events on Yucca Mountain has been interpreted by some workers as evidence that there may be a relationship between faulting and volcanic activity in the Crater Flat basin (J.W. Whitney *et al.*, USGS, written communication 1996a).

3.0
HISTORICAL SEISMICITY DATA

Historical seismicity catalogs available to the panel members describe seismicity within a 100- and a 300-km radius of the site, as collated by Woodward-Clyde personnel. Our calculations of recurrence parameters made exclusive use of the 300-km radius catalog, as we believe this catalog enables us to obtain better spatial averages than the smaller catalog.

Catalog magnitudes have been converted to a common moment-magnitude scale (Appendix D). We used the catalog completeness intervals defined by Woodward-Clyde Federal Services (I. Wong *et al.*, WCFS, written communication, 1997; I. Wong, SSC Workshop 3). Known nuclear explosions have been deleted from the catalog. Also, earthquakes that appear to be associated with regional fault sources have been subtracted from the catalog when estimating recurrence for the seismic source zones. These earthquakes were identified by drawing areas around each regional fault source (Section 4.2) and laying seismicity plots over the fault area map. The areas around the faults were drawn to include the area above the inclined fault plane (estimated dip projected to the base of the seismogenic zone) plus a nominal distance to allow for inaccuracies in epicentral locations.

The catalog was declustered using the algorithms of both Veneziano and van Dyck (1985) and Youngs *et al.*. (1987). The two declustered catalogs were given equal weight for calculating recurrence parameters.

A minimum magnitude of 2.5 was used to compute the recurrence parameters after considering maximum likelihood rates and b-values calculated as a function of minimum magnitude (Section 3.1 contains a description of the methods used to calculate seismicity parameters). Spatially varying a-values were included in the analysis through use of a Gaussian kernel. Details of the smoothing are discussed in Section 4.1.1

Focal mechanism data compiled by S.K. Pezzopane *et al.*. (USGS, written communication, 1996b, Table 7-3) were used for analysis of variations in focal depth and focal mechanism within the study area. Results of this analysis are discussed in Section 4.1.2.

4.0
CHARACTERIZATION OF SEISMIC SOURCES FOR GROUND MOTION ANALYSIS

Our model includes four categories of seismic sources: (1) *seismic source zones* to account for seismicity that cannot be attributed to fault-specific sources included in the model; (2) *regional fault sources,* which include mapped late Quaternary faults within about 100 km of Yucca Mountain, but not including the faults in the site vicinity; (3) *local fault sources* in the

vicinity of Yucca Mountain; and (4) *hypothetical faults* near the site. Different approaches are used to characterize each of these categories. Seismic sources that might make a significant contribution to the seismic hazard at Yucca Mountain (either because they have a relatively high rate of activity and/or because they are close to the site) are characterized in greater detail than are sources far from the site.

4.1 SEISMIC SOURCE ZONES

Seismic source zones are used to characterize volumes of the Earth's crust that are inferred to exhibit similar characteristics with respect to the magnitude and frequency of occurrence of earthquakes that cannot be attributed to fault-specific seismic sources (i.e., background seismicity). The seismicity within a given zone may be uniformly or non-uniformly distributed.

Uncertainties in the source zone geometry are incorporated in this analysis by considering different source zone models and a range of values for the depth of the seismogenic crust. Uncertainties in the magnitude frequency distribution within each zone are incorporated in the analysis by considering a range of values for the upper-bound earthquake and by considering different smoothing algorithms that provide for different levels of spatial smoothing of the earthquake epicenters in the seismicity catalog.

4.1.1 Definition

The region around Yucca Mountain commonly is divided into three major tectonic zones: the northern Basin and Range, the southwestern part of the Walker Lane belt, and the northeastern part of the Walker Lane belt. The northern Basin and Range extends from the western limit of the Colorado Plateau westward to the eastern side of the Walker Lane belt, as defined below, and from the southern boundary of the Snake River Plain southward to the gravity gradient, just north of the Hoover Dam, that separates the northern and southern parts of the Basin and Range (Saltus and Thompson, 1996). The southwestern part of the Walker Lane belt extends from the Sierra Nevada, at its western boundary, eastward to the Furnace Creek and Pahrump fault systems, and extends from the northern boundary of the Mohave Desert, namely the Garlock fault at its southern limit, about 700 km to the north-northwest. The northeastern part of the Walker Lane belt extends from the Furnace Creek and Pahrump

fault systems eastward to a line across which the topography changes from being very irregular to showing the regular N20°E pattern of basins and ranges that characterizes the northern Basin and Range.

All three provinces have been characterized by extensional tectonics from the Eocene to the present. In the northern Basin and Range, extensional structures dominate the tectonic pattern. Relatively little strike-slip deformation has occurred in this province relative to the two parts of the Walker Lane belt. The southwestern part of the Walker Lane belt is characterized by a strong northwest structural grain created by several major northwest-striking, right-slip and oblique slip faults. The northeastern part of the Walker Lane belt, in which Yucca Mountain is located, is a structural province characterized by numerous short, discontinuous strike-slip structures and by distributed strike-slip strain, including both northwest-striking right-slip structures and northeast-striking left-slip structures. This diverse structural pattern creates a very irregular topography in the northeastern Walker Lane belt.

The three provinces are structurally distinct and yet much more similar to one another than they are to any of the bordering provinces, including the Colorado Plateau to the east, the Mohave Desert to the south, and the Sierra Nevada to the west. The seismic characteristics of the Yucca Mountain region can be characterized based on the historical record of seismicity in the northern Basin and Range and the two parts of the Walker Lane belt. However, because of the structural differences between these three provinces, an even better characterization may be derived by studying the seismicity of these three provinces individually to see if they have distinct seismic characteristics. Accordingly, two seismic source zone models are considered in the logic tree (Figure DFS-3): *Model A,* which consists of one regional zone plus a site-vicinity zone (Figure DSF-4); and *Model B*, which has three regional zones plus a site-vicinity zone (Figure DFS-5). The one-zone model, three-zone model, and the site-vicinity seismic source zone are described below.

Model A - One Zone Plus Site-Vicinity Zone. In this model recurrence parameters are estimated for a single regional zone outside the local site zone (see Figure DFS-4) based on the 300-km radius historical catalog and the estimated upper-bound magnitude. This model, which is assigned a weight of 0.2, assumes that over a long period (million years), regional differences in tectonics are minimized because the region as a whole is undergoing roughly

the same rate of extension. Smoothing of the historical catalog was conducted using Gaussian kernels having different half-widths. The half-widths included in the analysis and their associated probability weights (in parentheses) are: 10 km (0.25), which is comparable to the location uncertainty for the better-located events in the region; 25 km (0.6) , which is comparable to the value used by Frankel *et al.*. (1996); and infinity (0.15), which corresponds to no smoothing.

Model B - Three Zones Plus Site Vicinity. In this model the recurrence parameters were estimated by dividing the region into three distinct zones (Figure DFS-5) in addition to a local site-vicinity zone. The zones reflect differences in fault style and orientation as well as differences in focal mechanisms and focal depths (Bellier and Zoback, 1995). The three zones are: (1) a Basin and Range zone; (2) an eastern Walker Lane zone; and (3) a western Walker Lane zone. The Basin and Range zone is characterized by extension along predominantly normal faults that trend north-south to NNE-SSW. The eastern Walker Lane zone is characterized by a mixture of normal (still dominant) and strike-slip faulting along NNW-SSE to NE-SW trending faults. In the western Walker Lane zone, strike-slip faulting predominates along NW-SE trending faults, and focal depths appear to be about 2 to 4 km shallower than surrounding regions, perhaps due to the increased regional heat flow. The three-zone model is assigned a higher weight (0.8) than the one-zone model, because in the short term (thousands of years), differences in the stress regimes in the three regions appear to have led to different styles of faulting.

Smoothing of the historical catalog was conducted in the same manner as for model A after removing earthquakes associated with specific fault sources. Half-widths for smoothing also were selected at 10 km, 25 km, and infinity, but weights were selected as 0.22, 0.53, and 0.25, respectively. Slightly more weight was given to infinity (as compared to Model A) because, if there are smaller regional zones, the spatial distribution of seismicity is more likely to be uniform within them.

Site-Vicinity Zone. The boundaries of the site-vicinity zone were drawn to include only the well-investigated part of the Yucca Mountain area that was the focus of the detailed USGS/DOE site-characterization studies. The earthquake recurrence parameters for the site-vicinity zone are estimated the same way as for Models A and B, except that a lower range of

values is considered for the upper-bound earthquake magnitude because the active faults capable of producing larger magnitude earthquakes have been identified and are included in the model as fault-specific (local) sources.

This rationale does not necessarily apply to the seismogenic part of the crust below a detachment layer, if one exists. Given a detachment zone, the potential for larger magnitude, deep events is considered by including in the hazard model a postulated hidden strike-slip fault (Section 4.4.2).

The background earthquake for the site-vicinity zone includes a potential earthquake produced by volcanic processes. Quaternary volcanic activity in the site zone has included five basaltic eruptions that formed small cinder cones and associated lava flows; four of these occurred at about 1 Ma, and the other at about 70 ka. The calculated probability of recurrence of this type of volcanic activity in the site area has been estimated at about 10E-7 per year (B.M. Crowe *et al.*, LANL, written communication, 1995). Whereas volcanic activity sometimes generates earthquakes having magnitudes > 6.0, the likely maximum magnitude earthquake associated with the formation of small cinder cones, such as formed in Crater Flat, is considerably smaller than magnitude 6.0. Given the low probability of a volcanic earthquake in Crater Flat as well as the small maximum magnitude, the upper bound earthquake for the site area source zone adequately covers this type of event.

4.1.2 Maximum Depth of Seismicity

Depth to the base of the seismogenic zone for all our models was based on studies of focal depth distributions of catalog (A quality) events and depths associated with focal mechanisms tabulated by S.K. Pezzopane *et al.* (USGS, written communication, 1996b), which also should represent high-quality hypocenters. Only 4 percent of A quality catalog events had depths ≥ 12 km; 2 percent of the events with focal mechanisms had depths ≥ 12 km. Few events had depths of greater than 16 km. The values for the depth of the seismogenic crust that were included in the analysis and their associated weights are: 12 km (0.6), 14 km (0.3), and 16 km (0.1).

4.1.3 Maximum Earthquakes

Model A (one regional source zone excluding the site-vicinity zone) regards the maximum earthquake magnitude as the largest earthquake that could occur in the region. This event could occur randomly and/or on a geologic structure that is not explicitly included in the seismic source model. For example, several Quaternary faults shown on Piety's map (1995, plates 1 and 2) but for which there is no reported evidence of late Quaternary displacement are not included in the seismic source model. These faults presumably have low slip rates; nonetheless, they could be the source of large events. Estimates of the maximum earthquake range from Mw 7.7, which corresponds to the largest earthquake considered for any of the regional fault sources (Section 4.2), down to magnitude Mw 7.0, which is believed to be a conservative estimate for the largest event that could occur without surface fault rupture. The values included in the seismic hazard analysis and their associated probability weights (in parentheses) are: Mw 7.0 (0.2), Mw 7.3 (0.6), and Mw 7.7 (0.2).

In Model B (three regional source zones excluding the site-vicinity zone), the maximum earthquake magnitude varies with the zone. The values considered for the western Walker Lane zone are the same as for Model A [i.e., Mw 7.0 (0.2), Mw 7.3 (0.6), and Mw 7.7 (0.2)]. A slightly smaller range of values is considered for the eastern Walker Lane zone and the Basin and Range zone because these zones seem to lack the major continuous structures (e.g., the Death Valley/Furnace Creek fault system) that characterize the western Walker Lane zone. The values for these zones included in the seismic hazard analysis and their associated probability weights (in parentheses) are: Mw 7.0 (0.2), Mw 7.25 (0.6), and Mw 7.5 (0.2).

Estimates of the maximum earthquake magnitude for the site-vicinity zone range from Mw 5.6 (about the size of the Little Skull Mountain earthquake) to about Mw 6, which corresponds to a rupture area of about 100 km^2 (Wells and Coppersmith, 1994). Clearly larger events have occurred in the Basin and Range that were not associated with surface fault rupture; however, given the close spacing of the local fault sources, we believe that larger events are best represented in the hazard model as occurring on the mapped faults. Selecting a cutoff magnitude of about Mw 6 also mitigates the problem of "double accounting" that can result by combining predictions of the number of large events based on observed seismicity with predictions of the number of small- to moderate-size events from paleoseismic evidence of past surface faulting events. The values included in the seismic

hazard analysis and their associated probability weights are: Mw 5.6 (0.2), Mw 5.8 (0.6), and Mw 6.0 (0.2).

4.2 REGIONAL FAULT SOURCES

Regional fault sources include the mapped late Quaternary faults that extend to within about 100 km of the site but lie outside the site vicinity (Figure DFS-6). These faults were identified based on information presented in the USGS analysis to identify relevant earthquake sources (S. K. Pezzopane, USGS, written communication, 1996), Piety's (1995) report on Quaternary faults within 100 km of Yucca Mountain, and discussions during the Seismic Source Characterization Workshops with personnel who have examined some of these faults in the field. Faults included as regional seismic sources are judged to be capable of generating magnitude 5 or larger earthquakes and, based on published reports, are inferred to have had multiple late Quaternary displacements. The regional fault sources and the seismic source parameters (and associated uncertainties) used to characterize the seismic potential of these structures are summarized in Table DFS-1.

Several faults that are known or suspected to have had Quaternary displacement, but are not reported to exhibit evidence of late Quaternary displacement, are not included as fault-specific seismic sources. The rate of slip on these faults is too low to have a significant effect on the ground motion hazard at the site, which is demonstrated by the results of previous analyses (Stepp *et al.*, 1995; I. Wong *et al.*, WCFS, written communication, 1997), which show that most of the regional fault sources have no significant effect on the overall hazard at the site. Earthquakes that occur on Quaternary faults that are not included as regional fault sources are modeled as part of the seismic source zone activity (Section 4.1).

4.2.1 Guidelines for Modeling

The logic tree used to characterize the regional fault sources is shown on Figure DFS-7. A more simplified approach is used to characterize the regional faults than is used to model the local faults (Section 4.3), particularly if the faults are more than about 50 km from the site. Generalizing the fault geometry does not have a significant effect on the source-to-site distance. It could have an effect on the calculated maximum magnitudes, but this is factored into the analysis by increasing the range of uncertainty on the estimated maximum magnitude

values. Except where noted in subsequent sections, the following guidelines were used in modeling regional fault sources.

Total Fault Length and Plan View Geometry. Discontinuous faults are generalized as a single continuous trace consisting of one or more straight line segments, so that the average source-to-site distance and total length of the modeled fault are consistent with the mapped fault. The total fault length is taken as the combined length of the straight line segments. A single, somewhat conservative, estimate of the total length is considered for most faults more than about 50 km from the site. For faults longer than about 25 km that extend to within about 50 km of the site, a range of values is assigned to account for uncertainties in total fault length.

Activity. The reported evidence for Quaternary displacement on all the regional fault sources described in this section is assumed to be associated with past seismogenic fault displacements (probability of activity = 1.0). Non-tectonic origins for some of the scarps may be possible, but are deemed to be sufficiently unlikely that their inclusion in this assessment would not significantly affect the hazard results.

Fault Dip and Downdip Width. Predominantly strike-slip faults are modeled as having a dip of 90 degrees. Predominantly dip-slip faults are modeled as having an average dip of 60 degrees. The faults are modeled as extending down to the base of the seismogenic crust, which is estimated to be between 12 and 16 km deep based on earthquake focal depths (see Section 4.1.2). The range of values for the maximum depth of faulting included in the analysis and their associated probability weights (in parentheses) are: 12 km (0.6), 14 km (0.3), and 16 km (0.1).

Maximum Earthquake Magnitude (M_{MAX}). Maximum magnitudes were calculated using an empirical relation that relates fault rupture length to magnitude (Wells and Coppersmith, 1994, relation for all fault types). Values were calculated by assuming 100 percent rupture of the longest geometrically defined fault segment and/or 100 percent rupture of the total fault length. The resulting values were considered to select a range of values for M_{MAX}. In most cases, the uncertainty associated with the preferred value for M_{max} is chosen to be about 3 of

a magnitude unit (i.e., plus or minus 0.2 to 0.3 Mw); however, as described below, somewhat wider and narrower ranges were considered in some cases.

Slip Rate. To the extent possible, estimated slip rates were based on published slip rates. Where reported rates were not available, slip rates were estimated (with wider uncertainty) based on analogy with other mapped faults and/or by inferring the likely ages and amount of displacement based on reported descriptions of the faults.

Earthquake Recurrence Models. The slip rate reflects the rate at which strain energy (seismic moment) is accumulating along a fault. The geologically derived seismic moment rate is used to translate slip rate into earthquake recurrence rate by partitioning the moment rate into earthquakes of various magnitudes according to a recurrence relationship (Cornell and Winterstein, 1986). Three general types of relationships have been proposed: (1) truncated exponential relations that mimic the behavior of recorded earthquakes in a region (e.g., Gutenberg and Richter, 1954); (2) a characteristic earthquake recurrence model (Youngs and Coppersmith, 1985) in which there is a greater tendency for earthquakes close to the maximum to occur than is predicted by seismicity-based exponential relations; and (3) relations that attribute all of the moment release on faults to earthquakes close to the maximum (Wesnousky, 1986). All three recurrence relations are considered in this hazard analysis (Figure DSF-7). The greatest weight (0.6) is assigned to the characteristic earthquake model. The results of detailed paleoseismic studies along active faults have shown repeatedly that the characteristic model is more representative of the seismicity of an individual fault than are exponential models that represent the seismicity of regions, which contain faults of various sizes. Maximum moment models assume that independent events on faults (i.e., excluding aftershocks and/or foreshocks) are always close to the maximum earthquake. This model is given less weight (0.3) than the characteristic model, but more weight than the exponential model, which is given the least weight (0.1).

The exponential and characteristic recurrence models require estimates of the b-value associated with specific faults. We used a b-value of 1.0 ± 0.1, which is based on the median value obtained for the seismic source zones plus or minus the 90-percent confidence interval. This uncertainty is about three times the uncertainty used to characterize the seismic source

zones. Greater uncertainty is warranted because there is more uncertainty in the magnitude frequency distribution associated with individual faults.

4.2.2 Parameters

Eighteen regional fault sources are included in the seismic hazard analysis (not including the hypothetical faults described in Section 4.4). The fault parameters used to characterize these sources are summarized in Table DFS-1 and described below.

Hunter Mountain/Panamint Fault Zone. The Hunter Mountain/Panamint fault zone is characterized by strike slip. Individual rupture segments are estimated to range from a minimum of about 16 km to a maximum of about 74 km. Considering the possibility of rupture along multiple segments, our preferred estimate for the maximum rupture length in the range of 45 to 98 km, suggesting a M_{MAX} in the range of Mw 7.0 to 7.4. Rupture of 146 km (the total fault length included in the model) suggests an upper bound of Mw 7.6. The values included in the analysis and their associated probability weights (in parentheses) are Mw 7.0 (0.2), Mw 7.4 (0.6), and Mw 7.6 (0.2).

The Quaternary slip rate on the Panamint Valley section of the fault is better constrained than is the rate along the Hunter Mountain section. Piety (1995, p. 383) reports that the Holocene/late Pleistocene slip rate on the Panamint Valley section is between about 1.1 and 3.2 mm per year, with a preferred estimate of about 2.5 mm per year. This range of values is used to characterize the entire fault. The values included in the analysis and their associated probability weights are 1.1 mm per year (0.2), 2.5 mm per year (0.6), and 3.2 mm per year (0.2).

Furnace Creek/Fish Lake Valley Fault Zone. This system of faults, which is characterized by strike slip, has a total combined length of at least 125 km (Piety, 1995, plates 1 and 2). Individual rupture segments are estimated to range from about 26 km to a maximum of about 87 km, with a preferred estimate for the maximum rupture length in the range of 38 to 87 km, suggesting a M_{MAX} in the range of Mw 6.9 to 7.3. Rupture of 149 km (the total fault length as shown on Figure DSF-6) suggests an upper bound of about Mw 7.6. The values included in the analysis and their associated probability weights are Mw 7.0 (0.2), Mw 7.3 (0.6), and Mw 7.6 (0.2).

There is obvious evidence of late Quaternary displacement along this fault trend, but the ages of the displaced units are not well constrained. Bryant (as cited in Piety, 1995) reports 46 m of late Pleistocene offset (right slip) along the fault. If late Pleistocene is interpreted to mean older than Holocene (10 ka) and younger than or about equal to latest Pleistocene (approximately 35 ka), the likely slip rate is in the range of $\geq$ 1.3 mm to < 4.6 mm per year. The values included in the analysis and their associated probability weights are 1.3 mm per year (0.2), 2.3 mm per year (0.6), and 4.6 mm per year (0.2).

Death Valley Fault Zone. The Death Valley fault zone has a mapped length of 71 km and is reported to be predominantly dip-slip (Piety, 1995). Rupture of the longest geometrically defined segment (51 km) yields an expected magnitude of Mw 7.1; rupture of the entire mapped fault suggests a magnitude of about Mw 7.2. The uncertainty associated with M_{MAX}, however, is assumed to be greater than this narrow range of values. The values included in the analysis and their associated probability weights are Mw 7.0 (0.2), Mw 7.2 (0.6), and Mw 7.5 (0.2).

Piety (1995) cites slip rates on the Death Valley fault zone ranging from as little as 0.08 mm per year to as high as 11.5 mm per year, with a best estimate of about 2.5 mm per year for the late Holocene slip rate. R.E. Klinger and L.A. Piety (USBR, written communication, 1996) report a vertical separation rate of 3 to 5 mm/yr. The values included in the analysis and their associated probability weights are 0.08 mm per year (0.2), 2.5 mm per year (0.6), and 11.5 mm per year (0.2), which gives a weighted average value of 3.96 mm/yr.

Pahrump/Stewart Valley Fault. This fault is composed of a discontinuous alignment of Quaternary fault scarps having a total length of about 41 km (Piety, 1995, plate 2). The total length of known Quaternary fault scarps is 18.5 km. The sense of Quaternary slip is inferred to be right-slip (Anderson *et al.*., 1995a). The fault can be divided into two roughly equivalent segments of about 20 km based on an apparent left step in the fault trend, suggesting a magnitude of Mw 6.6. Rupture of the entire fault suggests a magnitude of about Mw 7.0. These rupture models were considered equally likely; the values included in the analysis and their associated probability weights are Mw 6.6 (0.5) and Mw 7.0 (0.5).

The Quaternary slip rate on the Pahrump/Steward Valley fault is poorly constrained. Piety (1995) reports that the slip rate is "low," which is interpreted to mean that it is less than 1 mm per year, because faults having slip rates equivalent to or faster than this typically are well expressed geomorphically. Anderson *et al.*. (1995a, p. 12) report that the long-term vertical slip rate is "less than a few hundredths of a millimeter per year and is most likely on the order of thousandths of a millimeter per year" (less than 0.009 to 0.02 mm per year). Even allowing for a significant lateral component to the net slip, the Quaternary slip rate probably is on the order of 0.005 to 0.05 mm per year. Given the large uncertainties in the ages of the reported displacements, any slip rate within this wide range is considered to be equally likely. The values included in the analysis and their associated probability weights are 0.005 mm per year (0.5) and 0.05 mm per year (0.5).

West Spring Mountain Fault. A nearly continuous fault trace is mapped along the west flank of the Spring Mountains for about 29 km. The southern limit of the fault is uncertain; discontinuous traces (Piety, 1995, plate 2) suggest the fault might extend to its projected intersection with the Pahrump/Stewart Valley fault, for a total fault length of 51 km. Both of these options for the total length are included in the hazard analysis with equal weight. The fault may have a small oblique slip component, but is predominantly a dip-slip fault (Piety, 1995, p. 334). Values for M_{max} depend on the total fault length (Figure DFS-6). In both cases, we assumed that rupture length was equal to total fault length. The resulting values (using Wells and Coppersmith's 1994 relation for all fault types) were taken as the preferred values for M_{max} the associated uncertainty is estimated to be plus or minus about 3 of a magnitude unit (Table DFS-1).

J. L. Hoffard (University of Nevada, Reno, written communication, 1991, as cited in Piety, 1995, p. 354) reports a preferred value for the late Quaternary slip rate on the West Spring Mountains fault of 0.06 mm per year near Wheeler Wash. His maximum and minimum rates at this locality, given the uncertainty in the age of the displaced surface, are 0.2 and 0.02 mm per year, respectively. The values included in the analysis and their associated probability weights are 0.02 mm per year (0.2), 0.06 mm per year (0.6), and 0.2 mm per year (0.2).

West Pintwater Range Fault. Piety (1995, plates 1 and 2) shows a series of mapped fault traces extending nearly continuously along the west flank of the Pintwater Range for about

55 km. The faults are interpreted to be down-to-the-west normal faults. Rupture of the longest geometrically defined segment (about 41 km) suggests a magnitude of Mw 6.9; rupture of the entire fault suggests a magnitude of Mw 7.1. Accordingly, M_{max} is estimated to be Mw 7 ± 3. The values included in the analysis and their associated probability weights are Mw 6.7 (0.2), Mw 7.0 (0.6), and Mw 7.3 (0.2).

No reported slip rates were found for the West Pintwater Range fault. Piety (1995, p. 349) describes the fault as having weak geomorphic expression in late Quaternary deposits. Based on analogy to the Paintbrush Canyon fault, which is also characterized by weak geomorphic expression in late Quaternary deposits, the slip rate on the West Pintwater fault is estimated to be in the range of 0.02 to 0.2 mm per year. Having no basis for selecting a preferred value, we assumed that the actual rate is equally likely anywhere within this range. The values included in the analysis and their associated probability weights are 0.02 mm per year (0.5) and 0.2 mm per year (0.5).

Yucca Fault. The Yucca fault is predominantly dip slip (normal down-to-the-east) and has a mapped length of 25 km (Piety, 1995, plate 1). Given its short overall length, we assumed that the entire fault could rupture during the maximum earthquake, suggesting a M_{max} of 6.7 (± 3). The values included in the analysis and their associated probability weights are Mw 6.5 (0.2), Mw 6.7 (0.6), and Mw 7.0 (0.2).

No reported slip rates were found for the Yucca fault. The basis for assigning a slip rate to this fault is the same as for the West Pintwater fault. The values included in the analysis and their associated probability weights are 0.02 mm per year (0.5) and 0.2 mm per year (0.5).

Emigrant Valley North Fault. The Emigrant Valley North fault consists of a diffuse zone of north-northeast-trending fault traces having an overall length of about 27 km (Piety, 1995, plate 1). The style of faulting is uncertain. In this analysis, it is modeled as a 60 degree west-dipping normal fault having a linear surface trace centered along the zone of mapped faults. Given its short overall length, we assumed that the entire fault could rupture during the maximum earthquake, suggesting a M_{max} of 6.7 (± 3).The values included in the analysis and their associated probability weights are Mw 6.5 (0.2), Mw 6.7 (0.6), and Mw 7.0 (0.2).

No reported slip rates were found for the Emigrant Valley North fault. The basis for assigning a slip rate to this fault is the same as for the West Pintwater fault. The values included in the analysis and their associated probability weights are 0.02 mm per year (0.5) and 0.2 mm per year (0.5).

Oaks Spring Butte Fault. The Oak Springs Butte fault consists of a generally north-south zone of fault traces having an overall length of about 22 km (Piety, 1995, plate 1). Both down-to-the-east and down-to-the-west displacements occur within the zone, but the predominant displacement appears to be down-to-the east. In this analysis, it is modeled as a 60 degree east-dipping normal fault having a linear surface trace centered along the zone of mapped faults. Given its short overall length, we assumed that the entire fault could rupture during the maximum earthquake, suggesting a M_{max} of 6.7 (± ¼). The values included in the analysis and their associated probability weights are Mw 6.5 (0.2), Mw 6.7 (0.6), and Mw 7.0 (0.2).

No reported slip rates were found for the Oak Springs Butte fault. Based on published reports (Dohrenwend *et al.*, 1991, as cited in Piety, 1995, p. 256), there are "visible scarps" across surfaces that are estimated to be between 10 and 130 ka. Assuming that "visible scarps" means they are less than 1 to 2 m high, we estimated a slip rate less than about 0.01 to 0.2 mm per year. Having no basis for selecting a preferred value, we assumed that the actual rate is equally likely within this range. The values included in the analysis and their associated probability weights are 0.01 mm per year (0.5) and 0.2 mm per year (0.5).

Belted Range Fault. The Belted Range fault is a normal down-to-the-east fault that lies along the west foot of the Belted Range (eastern side of Kawich Valley). The total length of the fault is about 49 km (Piety, 1995, plate 1). Anderson *et al.* (1995b) report that scarps in Quaternary alluvium extend for only about 22 km of this length Assuming rupture lengths of between 22 and 49 km suggests a M_{MAX} in the range of Mw 6.6 to 7.0 (or about 6¾ ±¼). The values included in the analysis and their associated probability weights are Mw 6.5 (0.2), Mw 6.8 (0.6), and Mw 7.1 (0.2).

Anderson *et al.* (1995b, p. 13) report 11.3 m of displacement in surfaces that they estimate to be between 0.13 and 0.78 Ma, suggesting a slip rate between 0.01 and 0.09 mm per year.

Having no basis for selecting a preferred value, we assumed that the actual rate is equally likely within this range. The values included in the analysis and their associated probability weights are 0.01 mm per year (0.5) and 0.1 mm per year (0.5).

Kawich Range Fault. The Kawich Range fault consists of numerous subparallel normal faults and lineaments on the west side of the Kawich Range (Piety, 1995, plate 1; and Anderson *et al.*., 1995b). Most of the mapped faults occur in bedrock or at the bedrock-alluvial contact; the total length of Quaternary faulting is uncertain. The fault is divided into three line segments (Figure DFS-6), and four options are considered for the total length of the Quaternary active part of the Kawich Range fault. Most of the weight (0.68) is assigned to line segment A-B, because this is the only part of the fault having demonstrated displacements of alluvial surfaces (Anderson *et al.*., 1995b). The balance of the weight was assigned to the remaining options (Table DFS-1) based on the relative geomorphic expression of the adjacent sections of the fault. Values for M_{max} depend on total fault length (Figure DFS-6). For all four options, we assumed that the rupture length is equal to the total fault length. The resulting values (using Wells and Coppersmith's 1994 relation for all fault types) were taken as the preferred values for M_{max} and the associated uncertainty is estimated to be plus or minus about 3 of a magnitude unit (Table DFS-1).

Based on the subdued geomorphic expression of the fault and an inferred rate of scarp degradation, Anderson *et al.*. (1995b, p. 18) infer that the Quaternary slip rate on the Kawich Range fault is less than 0.01 mm per year. The values included in the analysis and their associated probability weights are 0.01 mm per year (0.5) and 0.001 mm per year (0.5).

Rock Valley Fault. The Rock Valley fault, which is inferred to be primarily a left-slip fault (Anderson *et al.*., 1995a), trends north-northeastward across alluvial fan deposits on the southeast flank of Little Skull Mountain. The continuity of this faulting with fault traces along its southwestern projection is uncertain. Three options were considered to account for uncertainty in the total length of the Rock Valley fault (Figure DFS-6 and Table DFS-1). Most of the weight (0.6) is assigned to the well-defined section of the fault (segment A-B) adjacent to Little Skull Mountain. The balance of the weight is assigned to the remaining options. The least weight (0.1) is assigned to option A-D because it seems less likely that the fault would continue west of its projected intersection with the north-south trending

Amargosa/Gravity (Ash Meadows) fault system. Values for M_{max} depend on the total fault length (Figure DFS-7). For all three options, we assumed that the rupture length is equal to the total fault length. The resulting values (using Wells and Coppersmith's 1994 relation for all fault types) were taken as the preferred values for M_{max} and the associated uncertainty is estimated to be plus or minus about ¼ of a magnitude unit (Table DFS-1).

Piety (1995, Table 6) reports vertical slip rates on the order of 0.003 to 0.01 mm per year based on observed surface displacements ranging from less than 1 m to 1.1 m. No estimate of the amount of lateral slip is presented. D. W. O'Leary *et al.* (USGS, written communication, 1996) estimate the maximum vertical displacement across the Rock Valley fault to be 0.054 mm per year (the sum across three stands of the fault). Assuming a major strike-slip component (e.g., a rake of 20 degrees) suggests that the net slip could be about three times the vertical slip, or about 0.16 mm per year. O'Leary (1996, pers. comm.) suggests the minimum slip rate (net slip) might be an order of magnitude less than the maximum. The values included in the analysis and their associated probability weights are 0.02 mm per year (0.5) and 0.16 mm per year (0.5).

Wahmonie Fault. The Wahmonie fault, which strikes northeast, has a mapped length of 14 km (Piety, 1995). The style of faulting is uncertain. The fault scarps are predominantly down-to-the-northwest according to Piety (1995, p. 346, and plate 1). In this analysis, it is modeled as a 60-degree northwest-dipping normal fault. Given its short overall length, we assumed that the entire fault could rupture during the maximum earthquake, suggesting a M_{max} of 6.4 ($\pm$¼). However, an upper-bound earthquake (M_{MAX}) of less than about 6.5 is considered unlikely for surface faulting events. The values included in the analysis and their associated probability weights are Mw 6.5 (0.8) and Mw 6.8 (0.2).

Reported scarp heights of < 1 m to 3 m on surfaces that are interpreted to be between 270 and 740 ka (Swadley and Huckins, 1990, as cited in Piety, 1995, p. 346) suggest slip rates on the order of 0.01 to 0.001 mm per year. The values included in the analysis and their associated probability weights are 0.01 mm per year (0.5) and 0.001 mm per year (0.5).

Yucca Lake Fault. The surface trace of the Yucca Lake fault measures 14 km (Piety, 1995, plate 1). The fault, which strikes northwest, appears to have predominately down-to-the-

northeast dip slip. Given its short overall length, we assumed that the entire fault could rupture during the maximum earthquake, suggesting a M_{max} of 6.4 ($\pm$3). However, an upper bound earthquake of less than about 6.5 is considered unlikely for surface faulting events. The values included in the analysis and their associated probability weights are Mw 6.5 (0.8) Mw and Mw 6.8 (0.2).

No reported slip rates were found for the Yucca Lake fault. Based on reported recognizable scarps on late Quaternary surfaces, the fault is assumed to have a slip rate on the order of 0.02 to 0.2 mm per year (see discussion for West Pintwater Range fault above). The values included in the analysis and their associated probability weights are 0.02 mm per year (0.5) and 0.2 mm per year (0.5).

Eleana Range Fault. The Eleana Range fault is a north-northeast-striking down-to-the-east normal fault having a total length of about 11 km (Piety, 1995, plate 1). Given its short overall length, we assumed that the entire fault could rupture during the maximum earthquake, suggesting an M_{max} of 6.3 ($\pm$3). However, an upper-bound earthquake of less than about 6.5 is considered unlikely for surface faulting events. The values included in the analysis and their associated probability weights are Mw 6.5 (0.8) and Mw 6.8 (0.2).

No reported slip rates were found for the Eleana Range fault. The basis for assigning slip rate values was the same as for the West Pintwater Range and Yucca Lake faults. The values included in the analysis and their associated probability weights are 0.02 mm per year (0.5) and 0.2 mm per year (0.5).

Peace Camp Fault. A series of discontinuous fault scarps have been mapped in alluvial deposits south and southwest of Mercury that are informally referred to as the Peace Camp fault (J. Yount, SSC Workshop 4). Based on its trend subparallel to the Rock Valley fault, the Peace Camp fault probably has a significant left-lateral component to the net slip. The total length of Quaternary faulting is uncertain. Estimates range from about 19 km, which includes the fairly well-expressed eastern section of the fault (segment A-B on Figure DFS-6), up to about 31 km (segment A-C) (J. Yount, SSC Workshop 4). More weight (0.7) is assigned to the better-expressed section of the fault (Table DFS-1). M_{MAX} depends on the total fault length. For both options, we assumed that the rupture length is equal to the total

fault length. The resulting values (using Wells and Coppersmith's 1994 relation for all fault types) were taken as the preferred values for M_{max} and the associated uncertainty is estimated to be plus or minus about 3 of a magnitude unit (Table DFS-1).

Half-meter-high scarps have been observed on late Pleistocene alluvial surfaces that are estimated to be between 20 ka and 130 ka (J. Yount, SSC Workshop 4), indicating vertical slip rates in the range of 0.004 to 0.025 mm per year. Allowing for a major strike-slip component, net slip might be several times vertical slip, which would be consistent with estimated slip rates on the Rock Valley fault. The values included in the analysis and their associated probability weights are the same as those assigned to the Rock Valley fault, 0.02 mm per year (0.5) and 0.16 mm per year (0.5).

Amargosa/Gravity (Ash Meadows) Fault. This fault consists of a discontinuous zone of Quaternary fault scarps and lineaments that trends north-south along the east side of Amargosa Valley. The total length of the zone is uncertain. Four options are considered, depending on how far the zone might extend to the north and/or the south. The most weight (0.56) is assigned to the 27-km-long central part of the fault (segment A-B on Figure DFS-6). It is considered equally likely that the fault extends to the north or to the south (i.e., segments B-C and A-D both have assigned weights of 0.2). The likelihood that the fault extends in both directions is equal to the products of the probabilities that it extents in either direction (0.04). M_{MAX} depends on the total fault length. For all four options, we assumed that the rupture length is equal to the total fault length. The resulting values (using Wells and Coppersmith's 1994 relation for all fault types) were taken as the preferred values for M_{max} and the associated uncertainty is estimated to be plus or minus about 3 of a magnitude unit (Table DFS-1).

Based on 155 cm vertical displacement observed in a trench across a trace of the Ash Meadows fault and an inferred age of about 40 ka, the slip rate is 0.04 mm per year (data from D.E. Donovan, University of Nevada, Reno, written communication, 1991, as cited in Piety, 1995, p. 87). Assuming that the displaced late Pleistocene deposits could be as young as about 20 ka or as old as about 89 ka suggests that the actual slip rate is probably within the range of 0.02 to 0.08 mm per year. Based on surfaces that are displaced as much as 3.4 m and an inferred minimum age of 40 ka, Anderson *et al.*. (1995a, p. 32) estimate that the slip